IMPROVEMENTS IN MAGNETIC RESONANCE IMAGING USING INFORMATION REDUNDANCY

A Dissertation

Presented to the Faculty of the Graduate School

of Cornell University

in Partial Fulfillment of the Requirements for the Degree of

Doctor of Philosophy

by

Ashish Raj

May 2005

IMPROVEMENTS IN MAGNETIC RESONANCE IMAGING USING INFORMATION REDUNDANCY

Ashish Raj, Ph.D.

Cornell University 2005

This thesis describes a number of algorithms related to the acquisition, reconstruction and post-processing of Magnetic Resonance data. The basic theme underlying each of these algorithms is the use of a unified systems approach to exploit information redundancy available in MR imaging. There are three basic contributions.

The first concerns the development of a new motion correction algorithm for Time-Resolved MR Angiography. Motion artifacts in angiography data are very difficult to remove without affecting vascular evolution. Our algorithm uses successive POCS iterations to remove unwanted artifacts without degrading quality. Double-blind testing has indicated significant improvement over angiograms created manually by experienced radiologist. In summary, our method seeks to exploit temporal redundancy to remove motion artifacts.

The second contribution is our recent work on Parallel MR imaging in presence of sensitivity errors using a Maximum Likelihood technique. It can be shown that standard phased array reconstruction using popular parallel imaging methods is inappropriate in presence of errors in measuring sensitivity maps of coils. Since these errors are actually quite common and unavoidable, current reconstruction methods can produce excessively noisy images. We describe a new algorithm that uses a Maximum Likelihood formulation that is tolerant to such errors. Our results

indicate almost 20 dB improvement in SNR for noisy cases compared to standard SENSE. In summary, this method effectively exploits receiver redundancy for resolution and scan time improvements.

The third major contribution involves exploiting prior information during the reconstruction of parallel data in MR. We develop a Markovian field model for the MR image prior and use it to perform Bayesian reconstruction of parallel data. This involves solving a complicated energy function with extremely challenging numerical properties. To make the approach practical, we have developed a fast graph cut based energy minimization algorithm. It turns out that the same algorithm is effective for all multi-dimensional problems involving linear systems with non-negative elements. We thus generalize our method to cover a larger set of target problems, including image deconvolution, motion deblurring, etc. Our results on reconstructed MR Angiography data suggests significant improvement in SNR compared to standard SENSE reconstruction. Results for image deconvolution are also very promising, and preliminary testing on several images has reported small but significant gains in peak SNR. In summary, the graph cut approach is a natural and powerful way to exploit spatial redundancy present in MR data.

Taken together, these contributions may have the potential to significantly alter the current state of the art in MR imaging, especially MR angiography.

BIOGRAPHICAL SKETCH

Ashish Raj was born in Godda, India, in 1976. He received the B.E. degree in Electrical and Electronic Engineering from the University of Auckland in 1998. He joined the graduate program in Electrical Engineering at Cornell in the Fall of 1998, and received the M.S. degree in Electrical Engineering in 2001, specialising in signal and image processing. Since then he has worked on medical imaging problems, particularly MRI.

ACKNOWLEDGEMENTS

First of all I would like to thank my advisor and mentor Professor Ramin Zabih for his constant guidance and encouragement. He has helped me learn how to conduct independent research, while at the same time making judicious interventions whenever I seemed to lose focus. His expertise and "feel" for the issues involved have greatly impacted my work and perhaps made up for some of my own shortcomings and lack of breadth. He has also done a marvelous job navigating several bodies of terrifying bureaucracy on my behalf. I thank him for these and many other ways he has guided me.

I would like to thank my parents for instilling in me an ethos and a culture of academic pursuit. Without their guidance and encouragement this thesis could not be written. I would like to thank Professors Thomas Parks, Dan Huttenlocher, Yi Wang and Martin Prince for forming a very effective and constructive committee. In particular Professors Wang and Prince deserve my unending gratitude for first introducing me to this amazing field, and then extending every possible guidance to help me understand the issues involved. I would like to acknowledge my collegues and fellow students Amy Gale, Junhwan Kim, Vladimir Kolmogorov, Pascal Spincemaille, Bryan Kressler, Ryan Brown, Zhenghui Zhang and Darian Muresan for many illuminating discussions. I thank Professor Charles Van Loan for his suggestions on Total Least Squares techniques. Finally, thanks are due to ECE administrative assistants Jamie Dal Cero and Cynthia Robinson who helped out with countless little chores.

TABLE OF CONTENTS

LIST OF TABLES

LIST OF FIGURES

Chapter 1

Introduction

1.1 Synopsis

Contemporary medical imaging has evolved to the point where it is now possible to image the interior of the human body in detail and speed that was considered, even a few years ago, to be improbable if not impossible. In turn, some major advances are currently on way that promise to further revolutionize the field. It is safe to surmise that in the next few years we will be able to perform imaging tasks now considered quite impossible. Most of these advances have come, and will continue to come, not from the basic hardware of imaging systems - which have remained largely unaltered over the years - but from new developments in acquisition, reconstruction and post processing methods (these will be defined and explained in a later section). In other words, advances in algorithms and software are currently the most compelling driver of improvements in imaging technologies, and this is likely to remain the case for the foreseeable future.

A very large number of problems that naturally occur in medical imaging - spanning acquisition, reconstruction and post-processing algorithms - in fact have surprisingly close counterparts in various fields of engineering and computer science. For example, the problem of reconstructing images from data acquired from MRI scanners is basically a problem of linear estimation. Consequently, the field could benefit from insights from the large body of work done in estimation theory,

ranging from array processing to communication systems. For example, a large body of work exists in these fields that handle information redundancy to improve performance. We show in this thesis that these methods can be modified to achieve similar improvements in medical imaging. Some imaging modalities make available a set of time-resolved images which provide temporal redundancy. Several new techniques acquire data from multiple receiver, resulting in receiver redundancy. Finally, individual medical images themselves contain considerable spatial redundancy which can be exploited.

Unfortunately, until very recently there have been few and sporadic attempts at exploiting and adapting existing methods from engineering and computer science to the problems that arise in medical imaging. In this thesis we will attempt to fill this gap by using various ideas from estimation and detection theory, graph theory and multi-variate optimization. The common theme underlying the various pieces of this work is the problem of exploiting information redundancy for improved imaging. Our work has largely concentrated on various MR imaging modalities, for reasons that we describe below. We present new algorithms for some challenging data acquisition, reconstruction and post-processing tasks in MRI which have the potential to result in disruptive innovations in the field.

In particular we describe in this thesis our work on the general problem of estimating the structural or functional image representing the region of interest, from a sequence of MR projection data. This data is obtained from measurement of echoes produced by molecules of various tissues in the region of interest, and is typically acquired in a Fourier-encoded space. We will describe several recent methods that exploit information redundancy and result in considerable improvements in acquisition speed and resolution, but in turn make the reconstruction problem

quite challenging. Another problem, common to all medical imaging modalities, is the retrospective removal of imaging artifacts. Again, using the redundancy present in the data, we are able to remove some of these artifacts. In particular, we will describe our work on removing motion artifacts, some of the most debilitating artifacts in MR. We argue that the issue of removing artifacts and the issue of improving resolution or speed are not separate, but complementary. Thus each method described in this thesis is in a rather fundamental way addressing the same problem. We explain this point in detail in §1.3. While there are existing methods to solve many of these problems, they are *ad hoc* and arguably sub-optimal, as we describe later. Our contribution consists of applying theoretical and computational approaches developed in electrical and computer engineering to all these problem areas keeping optimality and efficiency in mind. The result of this effort has been a set of methods based on well-known principles, but involving some non-trivial innovation in their use for MRI. Our results suggest considerable improvement in performance over existing methods, in each problem area we have addressed.

1.2 Why MRI?

This thesis is mainly concerned with techniques involving MR imaging. This is not merely a matter of choice. In recent years no other medical imaging technology has seen as much technical and clinical advancement as MRI, and no other technology has attracted as much attention. Technologies like x-ray, Computed Tomography (CT), Positron Emission Tomography (PET), etc that have played very important roles in medical imaging in the past are now slowly being complemented, sometimes displaced, by MRI. In a recent monograph, McRobbie *et al.*state that "MR imaging has evolved from unpromising beginnings in the 1970s to become nowadays the

imaging method of choice for a large proportion of radiological examinations and the 'jewel in the crown' of medical technology." [DEMM03], page 1.

One of the main reasons for the popularity of MR is that unlike other imaging technologies, it does not produce ionizing radiation, and is therefore safe even under prolonged imaging durations. MRI has displaced certain previous methods, for instance x-ray fluoroscopy for obtaining angiograms (images of blood vessels). X-ray fluoroscopy was earlier used only in very serious cases due to its high mortality rate and serious side effects. The advent of MR - based angiography suffers from none of these problems, and has consequently become a routine but life-saving procedure. There are numerous other examples of imaging applications which used to be rare due to radiation side effects, but are now routinely performed using MRI.

Perhaps even more compelling, from a radiological point of view, is the fact that MRI can image a large spectrum of tissue properties, unlike other imaging methods which basically measure x-ray or positron absorption by tissues in the ray path. Since the other technologies measure only a single property of tissues, they are very limited in the kinds of features, anatomical or functional, that they can measure. However, MR methods have been developed to image a large number of tissue properties. Depending on the parameters used during the scanning process, it is now possible to obtain good tissue contrast for numerous target areas. Furthermore, it is now possible to perform *functional* imaging, where one is not interested in the structure of the tissue, but its dynamic behaviour over time signifying some functional properties. For instance, MR-based functional brain imaging or functional MRI (fMRI), has revolutionized the fields of psychology and neuroscience. This capability is possible only using MR technology.

A related point is that MR imaging is much more flexible that other technologies. By simply adjusting the scan parameters on basically the same hardware, it is possible to perform vastly different imaging applications. For example, one can use a standard protocol to obtain a structural image of the brain. Then, by changing the scan parameters with the same physical setup, one can perform spectroscopic imaging, which measures the concentration of certain chemicals in brain tissue, for example Choline. This level of flexibility is entirely absent in most other imaging technologies. For all these reasons we have concentrated mainly on MRI techniques and modalities.

There are, to be sure, some disadvantages to MRI compared to other methods in specific imaging situations. For example, MRI is in general much slower than other methods. This is a serious disadvantage for several reasons. First, long scan times translate into expensive imaging - far fewer patients can be scanned per hour than would be possible in other methods. Second, few patients are very comfortable inside an MR scanner, and scans taking several minutes, by no means rare, can take a heavy toll on patients' stress and discomfort levels. But most importantly, long scan times increase the possibility of patient motion, which can cause severe artifacts. In fact it is very difficult to ensure an entirely motion-free scan, especially in applications like cardiac imaging where the motion may be physiological (e.g. induced by breathing) rather than external. Due to the nature of data acquisition in MR, motion within the field of view (FOV) is handled extremely poorly, and can cause severe degradation in image quality. The slowness of MRI must therefore be seen not merely as a factor in making the procedure costly, but as a fundamental factor limiting the quality of MR images and the number of applications to which MR methods can be put. MRI also suffers from some other sources of artifacts, like

non-uniform magnetic fields and off-resonance effects in certain MR modalities.

However, there are strong indications that the speed problem of MR may finally be on its way out. In fact a great deal of the "buzz" generated in the MR community in recent years has revolved around some new developments in acquisition and reconstruction techniques which promise to provide speed-up by several factors. The potential of such high speed-ups has re-energized the development of new clinical applications of MR which were previously considered impractical or impossible. This thesis will describe these new developments in some detail, and propose some original algorithms to further improve them.

1.3 A unified view of the algorithmic problem in MR imaging

Magnetic Resonance Imaging involves a fundamental trade-off between image quality and scan time [WBP04]. The data is acquired in k-space via a number of trajectories of certain kinds, for example Cartesian, spiral or radial. Each trajectory takes a certain amount of time to be acquired, and this acquisition time limits the overall scan speed. For a given sampling scheme one needs to acquire a sufficiently large number of k-space points in order to densely sample the space, i.e. satisfy the Nyquist sampling criterion. Therefore any reduction in scan time must come from either subsampling the trajectories, or by reducing the extent of k-space to be sampled. The former case will lead to aliasing artifacts since the Nyquist criterion will in general be violated, and must be redressed by multiple-coil-based parallel imaging techniques described earlier. It is well known that even if aliasing is completely removed by SENSE or other reconstruction methods, there is still a

net loss of SNR compared to the fully-sampled acquisitions. The latter case does not produce aliasing, but results in loss of resolution, since the radius of k-space traversed is directly related to the fine-ness of resolvable image space details. In either case, it can be argued, the result is loss of quality. Therefore decreasing the scan time results in loss of quality, either in terms of SNR, aliasing artifacts, or poor resolution. At this point one may raise the question of what happens if one is only interested in the overall quality of the image, regardless of the time taken to obtain it. Theoretically, if sufficient scan time is expended, it is possible to obtain images of arbitrarily high quality in terms of resolution. But as we have described earlier, this comes at the expense of higher risk of motion corruption. In some dynamic applications like angiography, fMRI, cardiac imaging, etc, high scan times can make the scan completely useless. Therefore, one always hits upon a ceiling of MR image quality, regardless of how much or how little time was spent during data acquisition, and regardless of which reconstruction method was used to remove aliasing. In this thesis we argue that all algorithmic advances that have occurred in the field, or are likely to occur in the immediate future, essentially involve shifting this trade-off point between scan time and image quality in a favourable direction. This point is pictorially represented by figure 1.1.

The images shown in the figure are of the vasculature of the trifurcation region. As indicated, short scan times cause aliasing artifacts, whereas long scan times cause motion artifacts. The figure also suggests two possible approaches for removing these problems: one can either de-aliase the images (parallel imaging), or remove artifacts caused by long scans (motion correction). The former approach is useful at the acquisition and reconstruction stages, while the latter is basically a retrospective post-processing approach. Either approach achieves a favourable

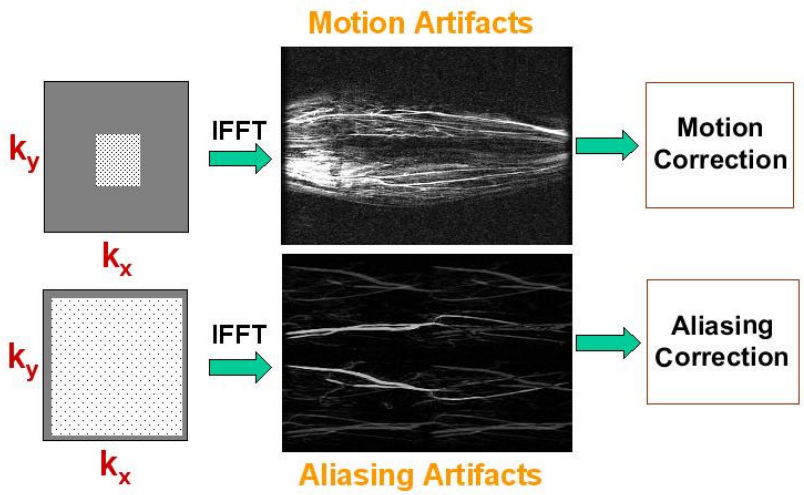

Figure 1.1: Various sources of artifacts in MR imaging, and ways to remove them.

shift in the tradeoff point, albeit in completely different but complementary ways.

In the following chapters we will present three different algorithmic approaches to improve MR acquisition, reconstruction and post-processing. These approaches seem, at first sight, to be rather disparate, intended for different applications. However, each approach essentially exploits information redundancy to obtain better image quality for a given scan time, or reduces scan time for constant quality. The first technique is on correction of motion artifacts in MR Angiography data. The second technique provides a new reconstruction algorithm for parallel imaging under a more realistic noise model than what is assumed in conventional methods like SENSE. The third technique performs fast, stable reconstruction of parallel data using an edge-preserving Markov Random Field (MRF) - based Bayesian estimation algorithm. Each of these methods is a "standalone" application, meaning they can be used independently or in combination with each other. But as we have emphasized above, they must be viewed as attempting to solve the same fundamental problem: how to use information redundancy to get better quality images for a certain scan time, and vice versa. We now present a unified description which connects all these approaches through a linear systems viewpoint.

1.3.1 A linear systems approach to MR imaging

Problems in MR imaging, whether for multiple coils or single coil, can in general be viewed as the following linear system

$$\mathrm{y} = E\mathrm{x} + \mathrm{n}, \tag{1.1}$$

where x is the desired image to be estimated, y represents observed data, n is additive instrumentation noise and E is the system matrix. The quantities concerned

are defined either in k-space or image space. We will describe in chapter 2 the detailed derivation of this model for single and multiple receiver coils. When using a single coil no speed-up is possible, and the data needs to be acquired densely in k-space. As we have pointed out, this lengthens the scan time, which can limit image quality due to motion artifacts. So the first and most obvious algorithmic challenge is to perform some kind of retrospective motion correction on the fully sampled Fourier-space data. A new algorithm performing this task, based on convex projections and called POCS motion correction, is described in chapter 3.

Since the motion problem can be quite difficult to remove in general, it is usually desirable to reduce its likelihood by accelerating the acquisition process via parallel imaging using multiple coils. The standard parallel reconstruction method, called SENSE, is basically a least squares estimate of x, which amounts to the maximum likelihood estimate under the jointly Gaussian i.i.d. assumption for n, the noise vector.

$$\hat{\mathrm{x}}_{SENSE} = \arg\min_{\mathrm{x}} ||\mathrm{y} - E\mathrm{x}||^2, \tag{1.2}$$

which has a closed form solution given by the pseudoinverse

$$\hat{\mathrm{x}}_{SENSE} = (E^H E)^{-1} E^H \mathrm{y}.$$

This method, while sufficient for many purposes, can be further improved in two roughly orthogonal directions, following the evolution of linear estimation theory used in other areas of electrical engineering. To begin with, a more general and realistic noise model must assume that the system E is itself corrupted by noise, since it involves sensitivity maps obtained by a measurement process. We show in chapter 4 that using the additive noise model in equation (1.1) instead of a realistic error-in-variable model can cause serious errors in reconstruction by current

methods. Methods such as SENSE assume that the coil outputs contain noise, but that the sensitivity maps are noiseless. In practice, however sensitivity maps are subject to a wide variety of errors, and we must consider a new generalized noise model

$$\mathrm{y} = (E + \triangle E)\mathrm{x} + \mathrm{n}, \tag{1.3}$$

where we have now introduced an error term in the system matrix E, caused by sensitivity measurement errors. The exact form of $\triangle E$ and the ways to solve systems of the above kind constitute major sections of chapter 4, but a brief outline is given here. At first glance, sensitivity noise appears to result in an errors-in-variables problem of the kind in equation (1.3) that is typically solved using Total Least Squares (TLS) [GL96]. However, existing TLS algorithms are inappropriate for the specific type of block structure that arises in parallel imaging. We have taken a maximum likelihood approach to the problem of parallel imaging in the presence of independent Gaussian sensitivity noise. This results in a non-quadratic multivariate optimization problem in chapter 4, which also describes a fast and efficient algorithm for implementing it.

Another way to extend the standard SENSE reconstruction is to exploit prior information about the desired image. Indeed, for any given noise model, a Bayesian estimate is likely to provide significant improvement over SENSE, which is essentially a maximum likelihood method. Most imaging situations allow the estimation of some useful *a priori* information about the image to be obtained. One of the most widely used methods is the Wiener estimate, which is a linear estimator satisfying the *maximum a posteriori* (MAP) criterion:

$$\hat{\mathrm{x}}_{MAP} = \arg\max_{\mathrm{x}} \Pr(\mathrm{y}|\mathrm{x}) \cdot \Pr(\mathrm{x}) \tag{1.4}$$

It is well-known [Kay93] (chapter 12) that if the additive noise vector n is

Gaussian distributed with covariance matrix R_n, and the desired signal x is also Gaussian distributed with covariance R_x, then the Wiener estimate

$$\hat{\mathrm{x}}_{wiener} = \arg\min_{\mathrm{x}} (\mathrm{y} - E\mathrm{x})^H R_n (\mathrm{y} - E\mathrm{x}) + \mathrm{x}^H R_x \mathrm{x}, \tag{1.5}$$

is the optimal estimator, and has a closed form shown below:

$$\hat{\mathrm{x}}_{wiener} = R_x E^H (E R_x E^H + R_n)^{-1} \mathrm{y}. \tag{1.6}$$

The Wiener estimate for parallel MR reconstruction of MR angiography data looks very promising compared to standard SENSE. However, the prior parameters, namely R_n and R_x must be deduced from incompletely sampled data, and therefore this method is appropriate for dynamic sequences like MRA, where a large number of frames are available.

For single-frame acquisitions, the Wiener method may not work very well. Furthermore, the Gaussian assumption about MR data is frequently inappropriate in real imaging situations. This brings us to general Bayesian estimation techniques. The use of a priori information in a Bayesian context has led to substantial performance gains in many areas of engineering, like signal/image denoising and restoration, image deblurring, radar processing, multiuser detection in cellular systems, etc. We posit that a Bayesian approach can similarly impact the quality of MR image reconstruction. In particular, Bayesian methods relying upon Markov Random Fields (MRFs) have become very popular in recent work in multi-dimensional inverse problems, for many reasons. Many multi-dimensional signals displaying local (e.g. spatial) correlation seem to be most naturally expressed in terms of MRFs. Many forms of distribution functions over MRFs, like Gaussian or Gibbsian, have been proposed to model real life images, videos and medical data. One of the major properties of non-Gaussian distributions like Gibbsian is that they are more

robust to outliers, and result in less smearing of important image features like edges. A large number of papers have proposed these general signal models for images, both consumer as well as medical [Li95]. For a general linear system as in equation (1.1), the MRF-based Bayesian methods seek an estimate of

$$\hat{\mathrm{x}}_{MRF} = \arg\min_{\mathrm{x}} ||\mathrm{y} - E\mathrm{x}||^2 + G_{MRF}(x), \tag{1.7}$$

where $G_{MRF}(x)$ is the *a priori* term. We use the class of discontinuity-preserving Gibbsian distribution given by

$$G_{MRF}(x) = \sum_{(p,q)\in\mathcal{N}} V(x_p, x_q). \tag{1.8}$$

The neighborhood system $\mathcal{N}$ consists of pairs of adjacent pixels, usually the 4-connected neighbors. The smoothness cost $V(l, l')$ gives the cost to assign l and l' to neighboring pixels. Typically the smoothness cost has a discontinuity-preserving form such as $V(l, l') = \min(|l - l'|, K)$ for some metric $|\cdot|$ and constant K. Such a smoothness term incorporates discontinuity-preserving priors, which can be justified in terms of Markov Random Fields [Li95].

Unfortunately, while such models are relatively easy to formulate and understand, the optimization problem associated with them is extremely challenging from a computational point of view. This is because the associated energy function is highly non-convex, and can be expected to contain numerous local minima. Traditional multivariate continuous optimization methods fare rather poorly in this environment, displaying slow convergence and getting trapped in poor local minima.

We propose a graph cut-based method to perform fast Bayesian estimation of x under a Gaussian or Gibbsian distribution defined on a Markov Random Field. Graph cuts have been used in recent year with spectacular effect on the

problem of stereo vision, which is a non-linear inverse problem where the underlying image is assumed to have a Gibbs distribution over an MRF. Unfortunately this body of work cannot be easily extended to the case of general linear inversion. In chapter 5 we develop a new graph cut algorithm which works on general linear inverse problems, provided the system matrix has non-negative entries. The MR reconstruction problem with Cartesian sampling falls under this category, as does general image restoration and deblurring. We provide results of our method on each of these applications.

1.3.2 A summary of contributions

We provide here a brief overview of each technique developed and described in this thesis.

1. *Correction of motion artifacts in MRA:* Chapter 3 presents an automatic method to remove motion artifacts via a novel application of convex projections. High-pass phase filtering is combined with convex projections in Fourier-space and image-space successively to remove motion artifacts. The method effectively removes motion artifacts without degrading vascular information. In effect, the method seeks to exploit temporal redundancy to remove motion artifacts.

2. *A Maximum likelihood approach to parallel imaging with sensitivity noise:* This work, presented in Chapter 4, develops a maximum likelihood approach to solving MR reconstruction problems of the kind shown in equation (1.3), by allowing for errors in sensitivity maps. This looks at first glance to be a classic error-in-variables problem usually solved by total least squares (TLS)

methods. However, we show that TLS algorithms are inappropriate for the specific type of block structure that arises in parallel imaging. We start from first principles and derive a simple energy cost minimization, and show that this results in a quasi-quadratic objective function. We discuss efficient algorithms for energy minimization under Cartesian sampling schemes. This method effectively exploits receiver redundancy for resolution and scan time improvements.

3. *Bayesian MR reconstruction from multiple coil data:* In Chapter 5 we present a general and powerful approach of using graph cuts to solve Bayesian reconstruction problems under MRF-based priors. MRF based approaches are popular due to locally adaptive reconstruction and their edge-preserving nature. We show however that the resulting reconstruction problem is computationally prohibitive, and suggest a new graph cut energy minimization approach. However, existing graph cut methods cannot be used for this problem, and we develop a modified algorithm. Our technique is a natural and powerful way to exploit spatial redundancy present in MR data.

4. *Using Graph Cut Techniques for Other Linear Inversion Problems:* We show further that apart from MR reconstruction, many pixel labeling problems in early vision, such as image restoration, motion deblurring, etc can benefit from the graph cut approach. In fact most linear multi-dimensional systems involving non-negative matrix elements can be solved within a Bayesian MRF framework using small modifications of our algorithm. We present results on image deblurring and motion deblurring.

We point out that the first technique is geared specifically towards MR angiography, while the other techniques are more generally applicable. It is noteworthy however, that the techniques contained in this thesis are especially suited for MRA, an important and life-saving procedure. Taken together, these techniques hold the promise of significantly improving the state of the art in MRA. This is owing to the fact that MRA suffers more than most other modalities from time, artifact, noise and resolution constraints. A combination of motion correction, realistic noise models, and MRF-based Bayesian reconstruction can be easily developed for MRA, and holds great potential in this area.

Chapter 2

Introduction to MR Imaging

This chapter provides a short description of MR imaging principles and techniques. The chapter is divided into two parts. The first part, §2.1, contains a brief overview of the fundamentals of MR imaging, including the underlying physics. The second part, §2.2, describes the imaging process in MR, both for single as well as multiple receivers. The second case in particular is a relatively new development in MR, and is popularly referred to as Parallel Imaging. We discuss this case in some detail, since it forms the basis of our work in accelerated acquisition techniques, described in chapters 4 and 5.

2.1 A brief introduction to MR imaging

Differing contrast response of different tissues in the body is the basis for MR imaging. In contrast to other technologies like CT, the contrast behaviour of these tissue regions can be altered drastically by using different acquisition techniques (called pulse sequences). This is one of the main reasons for the power and popularity of MRI. The MR image is produced by mapping the magnetization properties of protons within tissues. The mechanics of MRI are very complex, and we will provide a very brief overview of the same. For a simple, readable and non-mathematical introduction to MR physics and engineering, we refer the reader to the excellent monograph by McRobbie *et al.*[DEMM03]. A more comprehensive and technical treatment, from a signal processing point of view, may be found in [LL99].

During scanning, the MR scanner creates a magnetic field B_0 along which the

spinning protons align themselves, a process called magnetization. The proton spins in turn precess about th external field at the frequency, called Larmor frequency, which is proportional to the external field:

$$\nu = \gamma B_0.$$

The strength of this magnetization is proportional to the density of proton dipoles within tissue regions, referred to as *proton density* or PD. To acquire data, an additional radio-frequency (RF) pulse in the transverse direction is applied, which tips the spinning dipoles into the transverse plane. During the period these dipoles re-align themselves back to B_0, they emit RF signals which are picked up by receiver coils placed around the tissue. By a carefully orchestrated sequence of field gradients and other hardware, the resulting signal is frequency encoded, i.e. the frequency of the RF signal emitted by tissue protons varies according to their spatial position. It turns out that this frequency encoding is exactly identical to the well-known Fourier Transform. Hence the data points acquired by the receiver coils map directly onto the space of Fourier coefficients of image dimensions. For a three-dimensional image, the raw data get mapped to the (k_x, k_y, k_z)-space, usually referred to within the MR community as *k-space*.

To demonstrate frequency encoding, let us consider an experiment, where we are interested in imaging a one-dimensional image, along the x-direction. Suppose the external B_0 field is varied linearly along x, as per $B = B_0 + xG_x$. Then the frequency of the signal generated by the magnetization at x will be given by

$$\nu(x) = \gamma(B_0 + xG_x) = \nu_0 + \gamma G_x x.$$

In other words, the frequency content of the received signal is a direct mapping of the one-dimensional image! The overall received signal due to the spin density

$I(x)$ (corresponding to the tissue under investigation) for any given gradient value G_x is given by

$$y(t) = constant \cdot \int I(x) \exp(-i\gamma G_x x t) dx.$$

Now G_x is time-dependent in general, and we introduce $k_x = \int_0^t \gamma G_x(\tau)\tau d\tau$, and obtain

$$y(k_x) = constant \cdot \int I(x) \exp(-ik_x x) dx,$$

which is nothing but the Fourier transform of $I(x)$! Therefore, we can recover the "image" $I(x)$ by simply performing the inverse Fourier transform of $y(k_x)$. The process of acquiring data by stepping through various k_x values is called *frequency encoding*, for the obvious reasons. If the desired image is 2- or 3-dimensional, the situation is similar, except that one needs to introduce additional phase terms during each frequency encoding step. Conceptually, this is equivalent to selecting different rows of k-space, each row being acquired during a single frequency encoding step. The process of acquiring different k-space rows is therefore called *phase encoding*, since each of these steps differs from the other by a simple phase term. In this way the entire k-space, in one-, two- or three-dimensions can be sequentially acquired. This is pictorially depicted in figure 2.1.

The contrast produced by different tissue regions in the final MR image depends on three main properties of the tissue. Proton density, already mentioned above, is one of them, and determines the overall strength of the signal from various areas. The other two properties relate to how fast the transverse magnetization relapses to its original alignment with the B_0 field. There are basically two mechanisms by which this occurs: spin-lattice relaxation, and spin-spin relaxation. Without going into the detailed physics behind these properties, it suffices to know that these two mechanism give rise to two distinct relaxation times, called T_1 and T_2 times, which

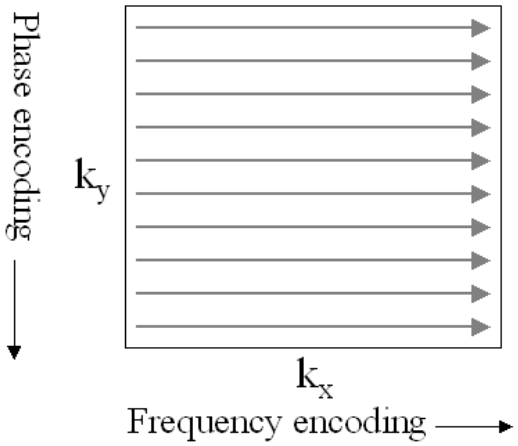

Figure 2.1: Schematic description of frequency- and phase-encoding steps used to acquire k-space data.

are intrinsic to the tissue in question. By carefully choosing the acquisition pulse sequence, the MR technologist can obtain images which are weighted according to any one of these three tissue properties. The resulting images are then said to be either T_1-weighted, T_2-weighted, or PD-weighted. Since different tissues in the body have different values of these parameters, a radiologist is usually able to exert great control over the contrast properties of the region being imaged.

2.1.1 Sampling k-space along trajectories

As described above, MR data is acquired in the Fourier- or k-space via a number of phase-encoding and frequency-encoding steps. We indicated that these steps are equivalent to acquiring single rows in k-space at a time. But in practice the data acquired can fall along not just rows, but more general trajectories, although the pulse sequences for these other trajectory types becomes considerably more

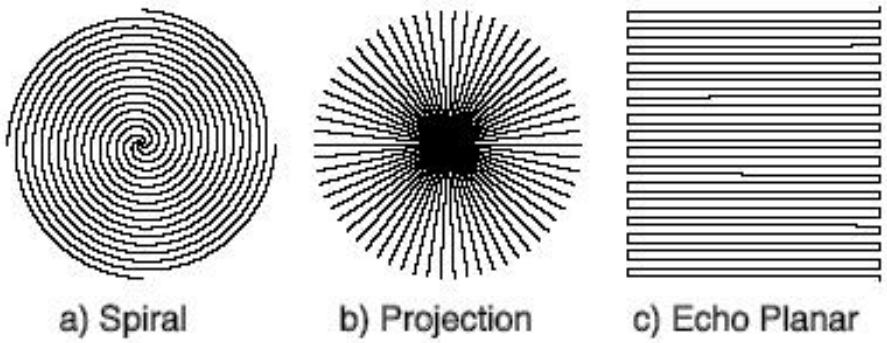

Figure 2.2: Popular k-space trajectories.

complex. Some of the most popular trajectory types are listed below, in the approximate order of popularity. Examples of these different trajectories are shown in figure 2.2.

1. *Cartesian*: Linear trajectories with regularly spaced sample points - the standard row-by-row order mentioned above. Figure 2.1 shows the standard Cartesian technique. Another Cartesian sampling method called EPI is shown in figure 2.2.

2. *Spiral*: Spiral trajectories with several spiral "leaves" oriented regularly around the circle.

3. *Radial*: Radial trajectories with regularly spaced sample points along each radial "spoke".

Due to the mechanics of the gradient switching and RF pulse sequences used, it turns out that densely-spaced samples along these trajectories can be acquired relatively fast. However, the process of going from one trajectory to the next in k-space requires some time-delay which is dependent on tissue properties like T_1,

T_2 and PD, as well as the particular pulse sequence being used. This time delay is usually of a magnitude which makes the overall acquisition time of the entire image quite large, of the order of several seconds for a single 2D image. Thus MRI suffers from a much slower scanning process than other technologies like CT or PET. Since the number of trajectories in any given k-space data set must be large enough for dense sample packing, there is usually a lower limit for any particular situation below which the scan time cannot be reduced without causing aliasing artifacts (described in the next section). Some exciting new methods have recently been discovered that promise to speed up the scanning process, and will be described in detail in §2.2 below. We note that speedup obtained by these methods is *not* due to a basic improvement in MR hardware or pulse sequence design, but rather in the process of reconstruction.

2.2 Accelerated scanning using parallel imaging

As mentioned in the previous chapter, one of the major disadvantages of using MRI is its slow scan time. More specifically, there is more or less a linear dependence of imaging resolution with scan time. For certain clinical applications like cardiac imaging, this problem has limited the use of MR methods. This is because we need to scan this region quickly to avoid motion artifacts that may result from the breathing process. However, a high-resolution scan of the cardiac region is not possible within such a small duration using current techniques. The development of new accelerated scanning techniques has therefore resulted in bringing several new MR application areas within feasibility, that were earlier considered impractical. In the last few years, several techniques have been developed that use multiple coils to substantially reduce scan time (and thus motion artifacts) without signif-

icant loss of image quality. The best-known such technique is SENSE [PWSB01], although there are also other methods such as SMASH [MOY+01] and GRAPPA [WND+03]. The basic idea of each of these methods is to speed up the acquisition by subsampling data in Fourier space, thereby causing aliasing or folding in image space. The aliasing is removed, and the full-resolution unaliased image recovered, by the use of multiple receiver coils, in contrast to traditional scanning where a single receiver coil is used. Although the techniques mentioned above have some differences in terms of certain specifics, they are all essentially identical from a high-level viewpoint as described above. These methods have had a significant impact in the medical imaging community; for example, a recent paper [vdBWK+03] states that "SENSE has opened new horizons in both routine and advanced MR imaging". In this thesis we will mainly use the SENSE algorithm when we talk about parallel imaging, since SENSE is widely recognized as the most general as well as powerful implementation of parallel imaging concepts [vdBWK+03]. Let us now describe the method in detail.

SENSE, like other parallel imaging schemes, uses multiple coils to subsample in k-space. Each coil also has a sensitivity map, which encodes the different responses of each coil over the imaging volume. These sensitivity maps are typically obtained by scanning with a phantom. The outputs of each coil can be combined with the sensitivity maps to reconstruct a full, unaliased image. The MR parallel imaging process is most naturally expressed in k-space as a linear system of the form

$$\bar{\mathrm{y}} = \bar{E}\bar{\mathrm{x}} + \bar{\mathrm{n}}, \tag{2.1}$$

where $\bar{\mathrm{y}}$ contains the (k-space) outputs of the receiver coils, $\bar{E}$ contains the (k-space) sensitivity maps, and $\bar{\mathrm{x}}$ is the (k-space) image.[1] The reconstruction al-

[1]See [GBD04] for a study of noise in medical imaging.

gorithm used by SENSE assumes that the output of the receiver coils has been corrupted by noise, represented by the vector $\bar{\mathrm{n}}$[2]. A more detailed formalization of the imaging process will be presented in section 4.1.2. Along with the k-space input-output model (2.1), we will also use the image-space input-output model:

$$\mathrm{y} = E\mathrm{x} + \mathrm{n}, \tag{2.2}$$

where x, n and y are in the spatial domain. As we will see in section 4.1.2, both E and $\bar{E}$ have specific block structures as a result of the imaging process. K-space noise $\bar{\mathrm{n}}$ is assumed to be Gaussian, independent and identically distributed (i.i.d.). Then due to the property of the Fourier transform, the image-space noise n is also i.i.d. Gaussian. The SENSE method takes a least squares approach, which is natural under these assumptions. Note that the least squares solution is well-known to be the maximum likelihood estimate [PTVF92, Ch. 15], again assuming this noise model.

2.2.1 System model

The system matrices E and $\bar{E}$ represent a concatenation over all coils of the discretized encoding operator which acts on the input image vector x and k-space vector $\bar{\mathrm{x}}$, respectively. The vector x is a discrete representation of the desired MR image $X(\mathrm{r}_\rho)$, where $\mathrm{r}_\rho \in \Omega$ is the 2-D spatial vector distributed over the support Ω of the image, and indexed by ρ, the spatial index. The parallel imaging process for each coil l can be summarized by figure 2.3, where S_l is the sensitivity map of the l-th coil, sampled on the same grid as X.

[2]We will use the notation that $\bar{x}$ represents a k-space object, while x is an image-space object; we will also denote 1D objects in lower case, and 2D objects in upper case.

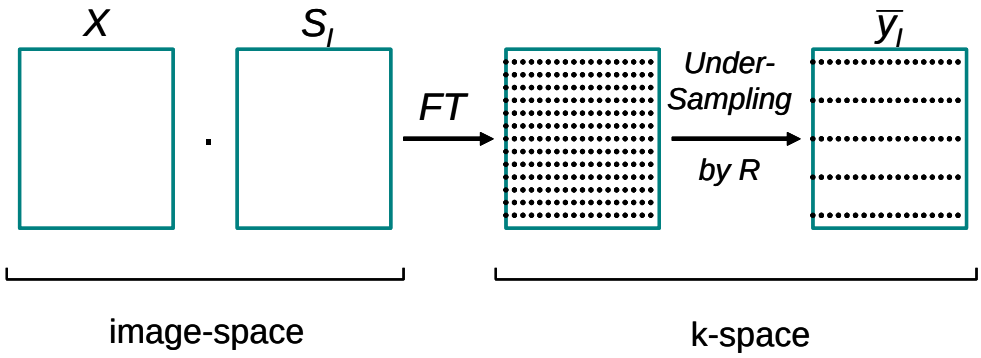

Figure 2.3: Schematic description of the parallel imaging process for the lth coil. Note that the multiplication of X and S_l takes place pixel by pixel.

Let the 2-D vectors k_κ and r_ρ be points in k-space and image-space respectively, and $\mathcal{F}$ be the 2-D Fourier transform operator. Following [PWBB01] the imaging process in figure 2.3 can be expressed as the integral of a set of weighted Dirac distributions in the spatial domain, which may further be written as the 2-D Fourier Transform of the distribution set, sampled at k_κ:

$$(\mathcal{F}E\mathrm{x})_{(l,\kappa)} = \mathcal{F}\left[\sum_\rho S_l(\mathrm{r}_\rho)X(\mathrm{r}_\rho)\delta(\mathrm{r}-\mathrm{r}_\rho)\right](\mathrm{k}_\kappa). \tag{2.3}$$

This can be further discretized by imposing a regularly sampled rectangular grid on the spatial variable r_ρ, and a similar grid on the k-space variable k_κ. Let vectors x and s_l be the lexicographically stacked versions of the 2-D MR image X and sensitivity responses S_l respectively, sampled on the regular grid of size $N \times M$. Let Y_l be the aliased (folded) image seen by the l-th coil, and y_l its vector representation, defined similarly. The Fourier Transform now becomes the 2-D DFT and the resampling over k_κ may be accomplished by using a general downsampling operator in k-space.

The output of the l-th coil can then be expressed as a matrix-vector product

$$\mathrm{y}_l = E_l\mathrm{x} = \; D^H_{N\times M} \downarrow_R D_{N\times M} S_l \cdot X = \; D^H_{N\times M} \downarrow_R D_{N\times M} diag(\mathrm{s}_l)\mathrm{x}. \tag{2.4}$$

The multiplication '$\cdot$' between the image and the sensitivity map takes place pixel by pixel, and the k-space downsampling operator $\downarrow_R$ resamples k-space according to the specific k-space trajectory used during the scan. As used in equation (2.4), $\downarrow_R$ is basically an indicator function from $\mathcal{C}^{N\times N}$ to $\mathcal{C}^{N\times N}$, with zeros for every k-space point not sampled by the trajectory. The subscript R denotes the data reduction factor, and superscript H denotes the Hermitian operator. The operator $D_{N\times M}$ is the 2-D DFT over the grid $(N \times M)$. The specific form of $\downarrow_R$ will depend on the reduction factor and the sampling method used, but we note that it need not be explicitly computed.[3]

Finally, the entire multi-coil output can be written in terms of equation (2.2), with

$$\begin{aligned} \mathrm{y} &= [\mathrm{y}_1^T, \ldots, \mathrm{y}_L^T]^T, \\ E &= [E_1^T, \ldots, E_L^T]^T \end{aligned}$$

Similarly, the k-space version can be written as

$$\begin{aligned} \bar{\mathrm{y}} &= [\bar{\mathrm{y}}_1^T, \ldots, \bar{\mathrm{y}}_L^T]^T, \\ \bar{E} &= [\bar{E}_1^T, \ldots, \bar{E}_L^T]^T \end{aligned}$$

This brings our discussion of multiple-receiver MR imaging to a conclusion. It is important to note that the entire development presented in this section finally comes down to a set of linear equations. Thus, the problem of MR reconstruction,

[3]We have skirted around the gridding issue involved with resampling general scanning trajectories to keep the discussion simple; however, the gridding step must always be understood to be implicit in the downsampling operator.

with either single or multiple coils, is basically one of linear inversion. In the next three chapters we will describe some new methods of performing this inversion, as well as some techniques to remove artifacts from already inverted data.

Chapter 3

Motion Correction in Time-Resolved MR Angiography Using Convex Projections

Time-resolved 2D Magnetic Resonance Angiography (MRA) is a promising clinical tool that suffers significantly from motion artifacts. In this chapter we present an automatic method to remove motion artifacts via a novel application of convex projections. The method works by exploiting temporal redundancy available in time-resolved MRA data to remove motion artifacts. We identify a large class of non-rigid in-plane motions where our method should be effective. High-pass phase filtering is combined with convex projections in Fourier-space and image-space successively to remove motion artifacts. The projections are designed to avoid degrading vasculature information during this process. The algorithm is stable, and converges quickly, usually within five iterations. Results on a large set of clinical MRA cases indicate significant improvement in the visual quality of angiograms. A double-blind evaluation shows that the algorithm produces significantly better scores ($p = 0.016$) when compared to angiograms produced manually by experienced radiologists.

3.1 Introduction

Time-resolved 2D Magnetic Resonance Angiography (2D MRA) is a promising clinical tool for non-invasive diagnosis of vascular diseases [MTJ98]. In 2D MRA a sequence of 2D MRI images is obtained while a contrast agent is injected. Typically each image takes approximately 2 seconds to acquire, and the entire sequence lasts about a minute. Subtraction of pre-contrast images (often called mask images) from post-contrast (arterial phase) images is then performed to obtain an image of the vasculature, that is, an angiogram. MRA provides both temporal information about blood flow as well as anatomic information about the vascular conduit. It eliminates the risks of iodinated contrast, X-ray radiation and arterial puncture used with conventional angiography. Instead it utilizes an intravenous injection of Gadolinium contrast which has an extraordinary safety profile, especially when compared to iodinated contrast. The MR data can be acquired in just a few minutes and does not require any of the post-procedural care needed with the arterial punctures used with conventional angiography. The subtraction of mask from arterial phase makes the technique very sensitive to Gadolinium so that tiny doses (e.g. $\sim$6 ml) can be used.

Patient motion is always a major challenge in MR, but 2D MRA is particularly susceptible to motion. The action of the contrast agent leads to small changes changes in intensity, while motion often leads to large intensity changes. Motion not only reduces the overall image quality, but can also obscure important temporal events like the arrival of contrast agent and the temporal evolution of the angiogram. As a result, important dynamic data relating to vascular evolution runs the risk of being completely swamped by even small amounts of patient motion. Motion of elongated structures (e.g. bones) can create a subtraction artifacts re-

sembling arteries. In many cases, the radiologist is forced to discard several frames with excessive motion artifacts, which can lead to potentially serious gaps in the temporal MRA record, and may even cause a misdiagnosis.

There has, of course, been a great deal of work on motion correction in MR (we provide a brief survey in §3.2.2). However, previous work has focused on rigid, global motion in single-frame MR images. In 2D MRA, however, it is necessary to handle a much larger variety of motion. Motion in the middle of the acquisition of a 2D image is particularly challenging, since that is when the low-frequency components of the image are acquired.

While handling motion in MRA is generally difficult, in 2D MRA the task is simplified by the availability of a sequence of images. Although patient motion is difficult to model, it is typically of fairly limited duration, and can potentially be overcome by exploiting the wealth of temporal data that 2D MRA provides. To this end, we present an iterative algorithm based on the widely used method called Projections Onto Convex Sets, or POCS (§3.2 contains a brief review of previous applications of POCS). By applying POCS in a novel manner, our algorithm corrects for motion without degrading radiologically important temporal events.

Our POCS-based method iteratively applies successive constraints to the corrupted frame, making it more similar to an artifact-free reference frame that is computed from other input frames. The constraints applied consist of four projections, two defined in image space, and two in Fourier space (usually called k-space in MR). These projections, described in §3.3, were designed specifically to prevent obliteration of vascular features, and to ensure stability and convergence of the POCS algorithm. We have identified a large class of non-rigid in-plane motions (defined formally in §3.4) where our method should be effective. Articulated limb

motion (bending, shifting) falls under this category. The results of our algorithm have been evaluated on a large set of clinical MRA cases collected over several months. Significant improvement in visual quality was reported in several cases exhibiting motion. A double-blind evaluation on 47 cases returned a p-value of 0.0162 on a two-tailed t-test, clearly indicating significant overall improvement over manually obtained angiograms.

The rest of this chapter is organized as follows. Section 3.2 presents an overview of MRA motion correction and related work, as well as a highlighting some assumptions made in our approach. Section 3.3 describes the POCS motion correction algorithm in detail, with sub-sections (A) to (D) devoted to each of its four convex projections. Of particular note is a new high-pass phase filtering operation to suppress non-global translational motion, described in §3.3.2. While the other three projections are easy to understand, our high-pass phase filter requires additional analysis, which is provided in §3.4. We give a detailed spectral analysis which suggests that a broad class of in-plane motions will result in low-frequency (band-limited) phase artifacts; such artifacts can be reduced by our high-pass phase filter. In §3.5 experimental results are presented for simulations as well as real clinical cases. The data reported by a double-blind evaluation of our technique is also included, and helps validate the new technique.

3.2 Overview of Proposed Method

Our automatic technique begins by identifying mask and arterial phase MRA frame using the algorithm described in [KZ03]. Motion-corrupted frames are corrected using the POCS algorithm, as shown in Figure 3.1. The process repeats for each corrupted frame in the sequence. The POCS algorithm assumes that an uncor-

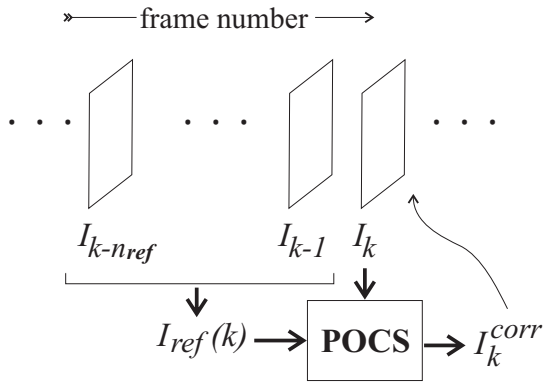

Figure 3.1: Overview of Motion Correction on MRA: the kth frame has motion artifacts, which are removed by the POCS algorithm by using the reference frame

rupted reference image can be obtained from the *reference set*, the set of n_{ref} frames preceding the corrupted frame, as indicated in the figure. A median or mean operation on the reference set is usually sufficient. The median is preferred as a more robust average, since it can remove the effect of outliers caused by motion in the reference set. We note that the implied "direction" in the sequence (left to right) is entirely arbitrary — the sequence could be processed from right to left, or different parts of the sequence could be processed in different orders.

The choice of n_{ref} is dependent on the levels of motion; it should be the smallest number sufficient to effectively mitigate motion noise in the reference set. We also experimented with more elaborate reference sets, for example sets striding either side of the frame in question, but the improvement was insignificant. Other enhancements like iterating the process over the entire sequence several times was found to yield little additional performance, on the other hand suffering from greater risk of obliterating important radiological features.

3.2.1 Assumptions

The most important assumption in our method is that it is possible to obtain a good reference image. Note that, as described above, the reference image is not a single image in the input, but rather is computed from n_{ref} input images. While our assumption fails if there is excessive motion in all or a majority of frames, such situations appear to be infrequent. Isolated instances of motion in the reference set will be ignored by the median operation. In cases with pervasive motion, taking the median over the reference set should produce a reference image with low levels of motion noise.

We also make a few assumptions in our individual projections. The first two projections, which take place in k-space, assume that the changes in k-space due to the contrast agent can be distinguished from the changes due to motion. The first projection (P_1 in §3.3) assumes that the vasculature is concentrated in image space, and hence distributed in k-space. The second projection (P_2) can soundly distinguish the action of the contrast agent, provided the motion arises a large class of in-plane motions. The image space projections (described under P_3 and P_4 in §3.3) estimate the portions of the image that are parenchyma or background (air). The estimate is designed to be conservative, and assumes that the image does not have a large amount of overall motion.

3.2.2 Related Work

Several motion correction techniques have been proposed earlier [ea96], [EK02] to correct for limited rigid, global motion in single-frame MR images, typically using subspace analysis. Navigator-based correction of rigid translation motion artifacts has also been proposed, with some success in removing non-rigid motion [MP03].

Some correction techniques have also been proposed to correct for global, rigid in-plane translation in MR temporal sequences [Hog03]. However, this method only works for rigid, global translation, and assumes that the motion is basically a step function in time, and occurs *between* frame acquisitions rather than *during* a frame acquisition. These methods are perhaps best suited for brain imaging since the motion in that case is expected to be rigid. However, none of these techniques are suitable for 2D MRA, because arbitrary amounts of non-rigid motion, containing rotations as well as translations, can easily occur in the middle of a frame acquisition. Furthermore, the motion may be non-global in the sense that certain portions of the field of view of the region imaged may move, while certain other portions may not. This is particularly relevant for peripheral 2D MRA, since limbs may move in rather complex ways. Our technique on the other hand is geared specifically towards motion correction for 2D MRA.

Another technique for mitigating motion was suggested for PET images [PT97] using motion information from video cameras. This method may be applied to MRA, but obviously requires additional sophisticated machinery, and tends to be sensitive to the motion tracking algorithm used. Cardiac gating using EEG has also been used extensively for peripheral MRA [GWB86], but apart from requiring additional hardware, its utility in removing patient limb movement is questionable. A comprehensive survey of correction methods for peripheral DSA is contained in [MNV99]. While most of these methods are specific to DSA and not readily applicable to MRA, retrospective methods proposed by the authors are of interest here. These methods rely on the template matching of moving regions in the image by using similarity measures bases on cross-correlation and robust measures of difference. While such techniques are possible for MRA, their utility is much

reduced due to the fact that MR images are acquired in k-space. Indeed, the phase artifacts caused by motion occurring in the middle of k-space acquisition cannot be removed by purely image-domain methods like template matching. Our POCS method on the other hand does not suffer from these problems.

POCS methods have been widely used in signal and image processing to perform band-limited interpolation and extrapolation [Fer94], image restoration [RA98], and in optics for non-coherent phase correction, where it is called the Gerchberg-Papoulis algorithm. These methods have recently been employed with some success in Partial Fourier MR techniques [OFS88], [XH01]. The success of POCS in so many different applications stems from the fact that it is a conceptually simple but powerful way to exploit a-priori constraints and properties that one believes the solution to possess. A common theme to all these algorithms is that they try to retrieve missing data from incompletely known data. In particular, Partial Fourier techniques use POCS to fill-in values for the entire k-space given partial k-space data covering the central k-space region. The POCS method proposed in the current work is different from the above POCS applications in the sense that we do not attempt to retrieve missing data, but to correct corrupted data.

An earlier automatic technique to create angiograms from MRA sequences was developed by Kim *et al.* [KPZ$^+$02]. The authors obtain the best angiogram by evaluating a quality metric, first separating pre- and post-contrast frames. Their method also identifies motion corrupted frames. Individual frames are not corrected, but if they contain sufficient motion they are not used for subtraction. As a result, in image sequences with a lot of motion their method can miss important events. This algorithm, however, performs a number of useful tasks (such as detecting contrast agent arrival), and as a result is used as part of the current

work.

3.3 POCS Based Motion Correction

POCS motion suppression relies upon projections defined on convex constraint sets. A set C is said to be convex if and only if for any two members $a, b \in C$ a binary mixture $c = \alpha a + (1 - \alpha)b, 0 \leq \alpha \leq 1$ also belongs to C. Common examples of convex sets include the set of numbers bounded from above and/or below, and the set of vectors with magnitudes bounded from above. Each projection is basically a way to move an arbitrary point in the solution space to a member of the constraint set that is "nearest" to it. The constraint sets must be convex in order to guarantee convergence [GPR67, Opi67].

We have used four projections P_1 to P_4 defined on convex sets, and described in sections (A) to (D). Starting from the corrupted image, the projections iteratively reduce motion artifacts by successively making it more similar to the reference image. The projections have been carefully designed to suppress arbitrary non-rigid motion artifacts in a variety of ways without degrading vascular enhancement. In (A)-(D) below and §3.4.1 we present an analysis to ensure that our projections satisfy this requirement.

Figure 3.2 summarizes our POCS algorithm, with the projections represented by labeled boxes.

The output of each projection is given by

$$I_k = (1 - \lambda_k)I_{k-1} + (\lambda_k)P_k(I_{k-1}), k = 1 \ldots, 4, \tag{3.1}$$

where $0 < \lambda_k < 1$ are the relaxation factors used to weight the projections, and P_k are the projections as shown in figure 3.2. The power of the POCS method

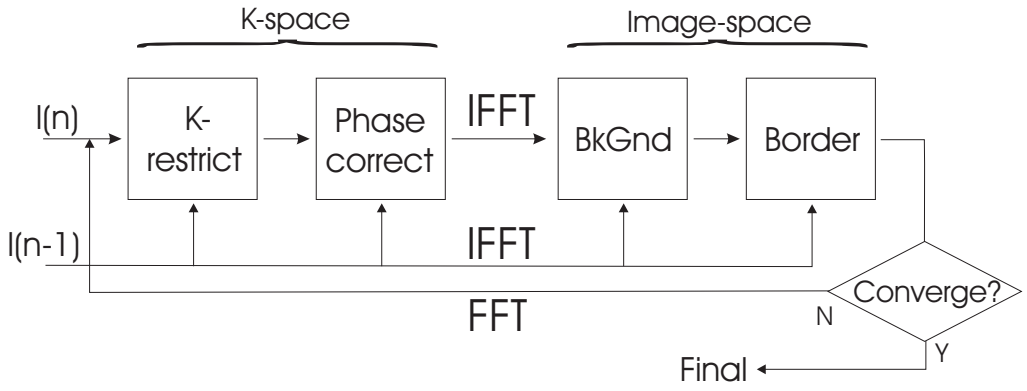

Figure 3.2: The POCS Motion Correction Algorithm: each box represents a convex projection.

derives from these highly independent constraint sets defined by projections P_1 to P_4, applied alternately in two orthogonal spaces (k-space and image space). We now define the projections.

3.3.1 P_1 : K-space Box Constraint Step

Complex and arbitrary patient motion can cause points in k-space of the corrupted frame to differ significantly from corresponding points in the reference frame. The mitigation of these undesirable changes is performed by the projection **k-restrict**, which restricts corrupted k-values to lie within a small range of the reference k-values. This amounts to what is usually called a *box constraint* applied to k-space values, since it defines a convex polyhedral or spherical "box" around a reference point within which any solution must reside. Our constraint can be expressed as the projection

$$P_1(I) = \begin{cases} I, & |I - I_{ref}| \leq \epsilon |I_{ref}|; \\ I_{ref} + (I - I_{ref})(\frac{\epsilon}{|I - I_{ref}|}), & |I - I_{ref}| > \epsilon |I_{ref}|. \end{cases} \tag{3.2}$$

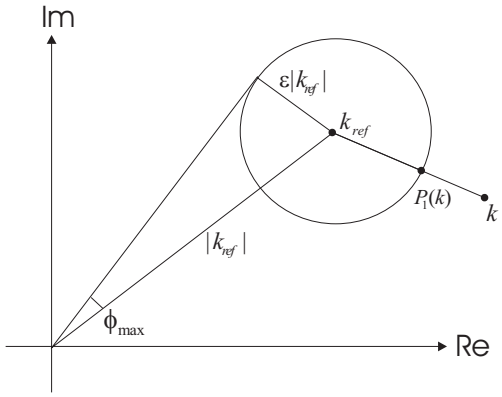

Figure 3.3: The k-space box constraint imposed by P_1

It is well-known that box constraints of this kind, illustrated in figure 3.3, define projections onto convex sets [XH01]. The circle around the complex value k_{ref} is of radius $\epsilon|k_{ref}|$, and the projection moves an arbitrary point k to the nearest point on the circle, denoted by $P_1(k)$.

Since P_1 keeps large temporal changes from occurring, its application in general will lead to loss of temporal information and obliteration of actual radiological temporal events along with motion artifacts. However, this not the case for 2D MRA, because the vasculature is sparse and localized in image space. Consequently the contribution of the vasculature to each k-space data point is likely to be very small and well-distributed. Hence a box constraint of the kind above will not adversely affect temporal evolution of the vasculature provided the box radius ϵ is comfortably larger than the mean energy per data point of the vasculature.

To validate this observation, we present in figure 3.4 a typical peripheral 2D MRA study of the trifurcation. Figure 3.4(a) shows the actual image obtained by 2-D Fourier transform of the k-space data. The angiogram obtained from this sequence is shown in (b). This image is NOT to the same intensity scale as (a) which has much larger intensities. The angiogram produces a relatively noise- and

background-free rendering of the vasculature. We plot the k-space magnitude of figure (c) as a function of distance to the center of k-space, in (c). This particular plot was obtained by averaging the magnitudes of four radial k-space lines — two vertical and two horizontal. The solid curve is obtained from (b), and the dotted curve from (c). We note that apart from one or two central pixels containing the lowest frequencies, the curve of the vasculature maintains almost constant (low) energy as a function of distance to center. In contrast, the reference data follows a more pronounced decline in magnitude. To demonstrate that a good choice of ϵ will not affect the vasculature data, we plot in (d) the ratio of vasculature magnitude in k-space to the overall magnitude. Since the ratio is susceptible to small changes in magnitudes, several radial lines in k-space of several angiograms had to be averaged to produce the plot. Notice that the highest point of the curve is lower than 0.25; hence $\epsilon > 0.25$ will ensure against vascular degradation.

3.3.2 P_2 : Phase Correction Step

The second projection, denoted by the box **phase-correct**, is an interesting phase filter for correcting translational motion artifacts. It relies on the claim that phase artifacts due to translation vary smoothly in k-space, whereas the phase information due to contrast arrival and vascular evolution is predominantly fast-varying and erratic. We give experimental evidence for this claim in figure 3.5. While we cannot prove this claim analytically, we give a theoretical and empirical argument in favor of it in §3.4, as well as a proof of convexity.

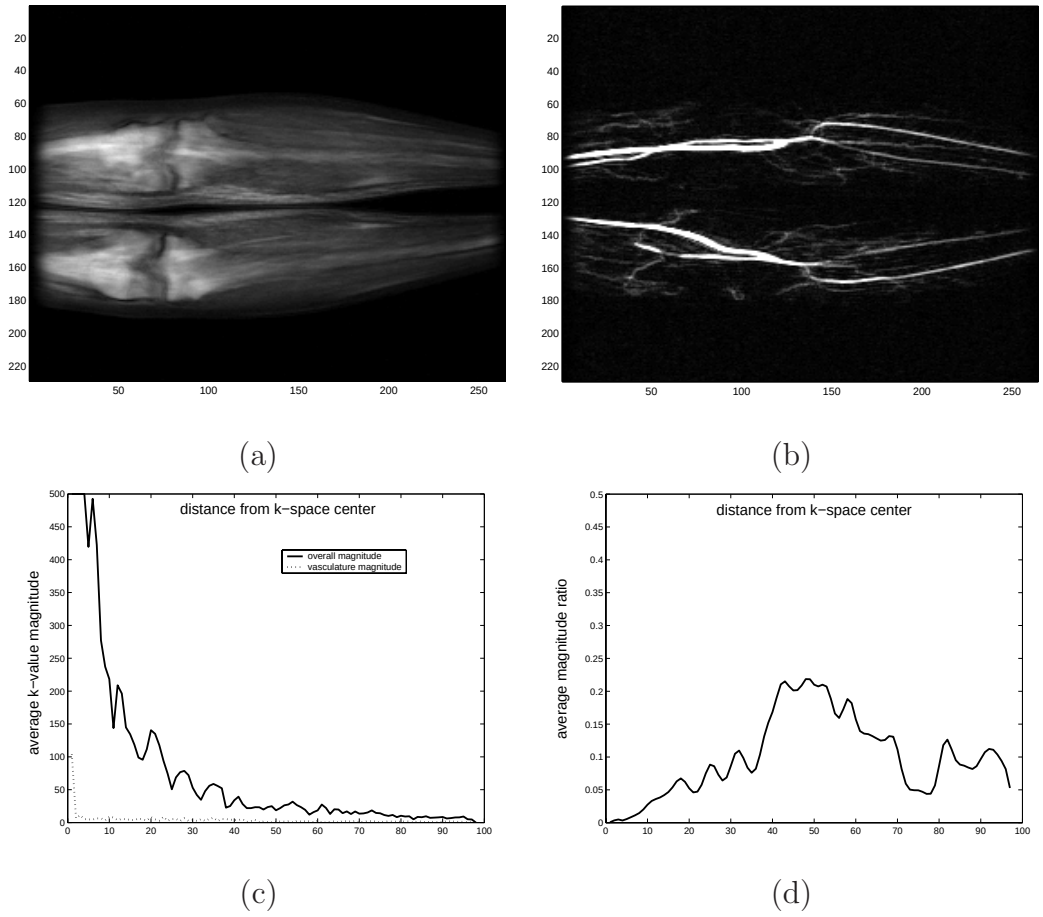

Figure 3.4: A typical peripheral 2D MRA case (a) Original frame, image space, (b) Difference image (c) Plot of k-space magnitudes vs. distance to center, and (d) ratio of vasculature magnitude to overall magnitude.

3.3.3 P_3 : Parenchyma Correction Step

Projection P_3, **parenchyma-correct**, imposes additional intensity constraints in image space. It forces the regions of the image reasonably deduced to be parenchyma (flesh) to be "close" to the corresponding regions of the reference image via a similar box constraint as in (3.2). Let $\mathcal{P}$ be the set of all pixels belonging to regions deduced to be parenchyma. Then for every pixel p in the corrupted image and the corresponding pixel p_{ref} in the reference image

$$P_3(p) = \begin{cases} I(p), & p \notin \mathcal{P}; \\ I(p), & p \in \mathcal{P}, \quad |I(p) - I(p_{ref})| \leq \eta |I(p_{ref})|; \\ I(p_{ref}) + \eta \frac{I(p) - I(p_{ref})}{|I(p) - I(p_{ref})|}, & p \in \mathcal{P} \quad |I(p) - I(p_{ref})| > \eta |I(p_{ref})|. \end{cases} \tag{3.3}$$

Again, this is well known to be a projection onto a convex set. Unlike ϵ, the box radius η need not be conservative, since we do not expect any useful temporal information to exist within the parenchyma region. The contrast agent courses only through the vasculature, and any big or small intensity differences within parenchyma are likely to be artifacts. The question of deducing the parenchyma regions from noisy and motion corrupted sequences is quite important. For sequences without an enormous amount of motion (§3.2.1) it is possible to obtain an initial subtracted image of the angiogram from which a reasonable estimate of the parenchyma regions can be obtained. Fortunately the projection P_3 does not require high accuracy in deducing the parenchyma regions, allowing us to use a very conservative estimate in order not to introduce subsequent errors.

3.3.4 P_4 : Background Forcing Step

The background of an MRA image is the region with no signal, and should ideally be zero. However, due to instrument noise as well as spurious motion artifacts,

this is usually not the case. We therefore impose our final projection P_4, **BkGnd** in figure 3.2, by deducing the background from the reference image and forcing it to be zero in the corrupted image. This is clearly a projection onto a convex set, since any linear combination of two images of zero background produces an image of zero background. As before, we have used a conservative estimate of background regions in order not to introduce further errors.

3.4 A High-Pass Phase Filter for Suppression of Translation Artifacts

In this section we show that phase artifacts caused by general non-global translation are band-limited to low frequencies through spectral analysis of the phase under a multi-piece translation model. In figure 3.5 a typical example is shown: (a) shows a typical spectrum of phase caused by non-global translation (§3.4.4 describes how we obtained this plot), and (b) shows a typical spectrum of the phase caused by the vasculature. This plot was obtained with Burg's average periodogram [SM97] from several rows of vasculature phase in k-space. The figure clearly shows that a modest high-pass phase filter effectively suppresses translation artifacts. Our filter has an impulse response $h = [-0.2, -0.6, 1, -0.6, -0.2]$, and the frequency response shown in figure 3.6.

The filter is one-dimensional because we chose to filter only in the Frequency Encode (FE) direction [MTJ98]. In MRI, it is usually assumed that a single scan line in the FE direction is sufficiently quick to not suffer from phase distortions like (3.5) due to patient motion [EK02]. Thus all motion effects may be assumed to occur *between* FE lines, not *within* them. Filtering only in the FE direction there-

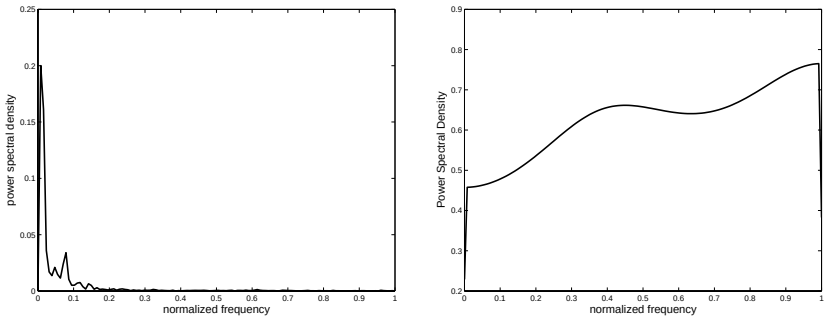

(a) (b)

Figure 3.5: Typical power spectra of phase signals in k-space, obtained from the phase difference between consecutive frames: (a) Non-global translation; (b) phase due to vasculature, obtained from an artifact-free sequence.

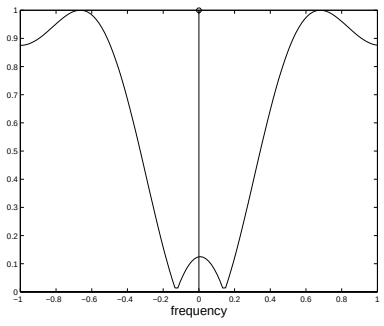

Figure 3.6: Frequency response of the high-pass phase filter.

fore prevents phase distortion in corrupted FE lines from influencing the phase of adjacent non-corrupted FE lines. In §3.4.1 we prove the convexity of the projection defined by the phase filter. The remaining sections discuss the spectral properties of translation phase.

3.4.1 Proof of Convexity of P_2

Proving the convexity of P_2 is rather complicated since it acts only on the phase, and is therefore not guaranteed to define a complex projection in $\mathcal{C}^{MN}$, the space of $M \times N$ complex images. Theorem 1 proves that this operation does in fact approximate, to arbitrary accuracy, a convex projection by virtue of the construction of our algorithm.

Theorem 3.1 *Let $H(\phi(k_x, k_y))$ represent the high pass filtering operation on the phase image $\phi(k_x, k_y)$ performed by the phase correct step. Let L be the complementary low-pass filter constructed such that $LH = 0$. Let C be the set of $M \times N$ complex k-space frames of identical magnitude $M(k_x, k_y), k_x = 1 \ldots M, k_y = 1 \ldots N$ such that $C = \{M(k_x, k_y)e^{i(\phi_0(k_x,k_y)+\phi(k_x,k_y))} \mid L(\phi(k_x, k_y)) = 0\}$. We will drop the indices (k_x, k_y) henceforth for convenience. Then*

1. *The phase correction step defines a projection onto C.*

2. *Set C approximates a convex set over a region of interest $R \subset C$ containing members with phase bounded by ϕ_{max}: $-\phi_{max} \leq \phi \leq \phi_{max}$. The error of approximation is proportional to ϕ^2_{max}.*

3. *The k-space box projection P_1 with box radius ϵ imposes a bound ϕ^2_{max} on the phase of the intermediate POCS solution at every iteration, with $\phi_{max} = \epsilon$.*

PROOF:

1. For any $A = Me^{i(\phi_0+\phi)}$, $A' = Me^{i(\phi_0+H(\phi))} \in C$, since $L(H(\phi)) = 0$. Hence **phase-correct** step with phase filter H defines a projection onto C.

2. Let $A_1 = Me^{i(\phi_0+\phi_1)}, A_2 = M\ e^{i(\phi_0+\phi_2)}$ be two members of C. We need to show that $\bar{A} = \alpha A_1 + (1-\alpha)A_2$ also belongs to C. We have

$$\bar{A} = Me^{i\phi_0}[\alpha e^{i(\phi_1)} + (1-\alpha)e^{i(\phi_2)}].$$

Linearizing the expression within square brackets by the Taylor Series we obtain

$$(\alpha + 1 - \alpha) + (\alpha\phi_1 + (1-\alpha)\phi_2) - \frac{i}{2}(\alpha\phi_1^2 + (1-\alpha)\phi_2^2) + \text{higher order terms.}$$

The higher order terms can be omitted since they are likely to be extremely small for small ϕ_1 and ϕ_2. Expanding this in a Taylor Series in $(\alpha\phi_1 + (1-\alpha)\phi_2)$ by completing the square for the second order terms and omitting higher terms, we get

$$\bar{A_1} = Me^{i\phi_0}\{e^{i((\alpha\phi_1+(1-\alpha)\phi_2))} + E\},$$

where the error term E is the residue from completing the square. Now it is clear that $\bar{A_1}$ belongs to C up to the error term E, since $L(\alpha\phi_1+(1-\alpha)\phi_2) = 0$.

Furthermore, it is straightforward to show that $E = \frac{\alpha(1-\alpha)}{2}(\phi_1 - \phi_2)^2$. Given that $-\phi_{max} \leq \phi_1, \phi_2 \leq \phi_{max}$, clearly the maximum error occurs for $\alpha = 1/2$, $\phi_1 = -\phi_2 = \phi_{max}$, and the maximum error is given by $E_{max} = \phi_{max}^2/2$.

3. From figure 3.3, every k-space data point k of every intermediate solution must reside within the circle of radius $\epsilon|k_{ref}|$ in the complex plane, where k_{ref}

is the corresponding reference point. Then the maximum phase difference between any two points in that circle is ϕ_{max} as shown in the figure. Since a tangent subtends a right angle at the center, we have $\sin(\phi_{max}) = \epsilon$. Result follows from small angle approximation of sines.

3.4.2 Phase Artifacts For a Piece-wise Motion Model

A global translation of $(\triangle_x, \triangle_y)$ in the complex image $I(x, y)$, with $K(k_x, k_y) = \mathcal{F}(I(x, y))$ being the k-space image, leads to a linear phase term in k-space given by $K'(k_x, k_y) = K(k_x, k_y) \exp(ic(\triangle_x k_x + \triangle_y k_y))$, for some constant c. The Fourier transform of this phase is obviously band-limited to low frequencies. We provide evidence in this section that this continues to be the case even for non-global, non-rigid translations, provided they can be approximated by the multi-piece motion model

$$K'(k_x, k_y) = \sum_{i=1}^{N} K_i(k_x, k_y) \exp(ic(\triangle_{xi} k_x + \triangle_{yi} k_y)), \tag{3.4}$$

where N is the number of image pieces, and each K_i is the transform of an image piece undergoing translation by $(\triangle_{xi}, \triangle_{yi})$. Equation (3.4) is reasonable for arbitrary non-rigid translation for sufficiently large N.

To begin with, we need a formal definition for band-limited images:

> *Definition*: Let $\Omega(W)$ be defined as the set of two-dimensional smoothly-varying functions $\phi(k_x, k_y) \in \mathcal{R}^2$ whose Fourier Transforms $\mathcal{F}(\phi)$ are band-limited to the low-frequency band $[-W, W] \times [-W, W]$, with W being the angular frequency cutoff.

Using expressions for phase spectra we will argue that the following holds:

Proposition 1: The phase difference between the corrupted and reference frame, $\triangle\phi(K', K) = \phi(K') - \phi(K)$ belongs to $\Omega(W)$, i.e., is band-limited. Consequently, the power spectral density of $\triangle\phi(K', K)$ is concentrated in the low frequency region $[-W, W] \times [-W, W]$.

To keep the analysis uncluttered, we only consider the two-piece model

$$\begin{aligned} K'(k_x, k_y) &= K_1(k_x, k_y) \exp(i\phi_1(k_x, k_y)) \\ &+ K_2(k_x, k_y) \exp(i\phi_2(k_x, k_y)) \cdot \exp(ic(\triangle_x k_x + \triangle_y k_y)), \end{aligned} \tag{3.5}$$

where $\phi(\cdot)$ denotes the phase of a complex quantity, K_1 is the stationary component, and K_2 undergoes translation. However, this does not cause loss of generality due to the following theorem.

Theorem 3.2 *If Proposition 1 holds for the two-piece model (3.5), then it also holds for the multi-piece model (3.4). That is, the phase difference $\triangle\phi(K', K)$ is band-limited for (3.4) as well: $\triangle\phi(K', K) \in \Omega(W)$.*

PROOF: Let

$$\Gamma_m^n = \sum_{i=m}^{n} K_i(k_x, k_y) \exp(ic(\triangle_{xi} k_x + \triangle_{yi} k_y))$$

$$\gamma_m^n = \sum_{i=m}^{n} K_i(k_x, k_y)$$

$$\triangle\phi^{(n)} = \phi(\Gamma_1^n + \Gamma_{n+1}^N) - \phi(\Gamma_1^{n-1} + \Gamma_n^N).$$

From Proposition 1, $\triangle\phi^{(n)} \in \Omega(W) \quad \forall n \in [1, N]$ since the phase difference is between two signals differing by only a single component K_n which undergoes translation. By the definition of $\triangle\phi^{(n)}$, it is easy to show that

$$\sum_{i=1}^{N} \triangle\phi^{(n)} = \phi(\Gamma_1^N) - \phi(\gamma_1^N) = \triangle\phi(K', K).$$

Now the set $\Omega(W)$ is obviously closed under addition, i.e. a sum of signals belonging to $\Omega(W)$ also belongs to $\Omega(W)$. Therefore $\triangle\phi(K', K) \in \Omega(W)$.

A general expression of the phase shift is derived (equation (3.6)), but explicit spectral analysis of this expression is difficult. We instead focus on three separate cases, whereby the moving piece is considered small, large, and equal, respectively, compared to the non-moving piece. In each case, a spectrum of $\triangle\phi(K', K)$ is explicitly derived, and found to be band-limited. We also present computed spectra of intermediate cases to verify that band-limitedness continues to be true across all scenarios.

3.4.3 Expression For Phase Difference

We wish to obtain expressions for the phase difference $\triangle\phi = \phi' - \phi$ caused by the two-piece translation model (3.5). We assume that the phase $\phi(k_x, k_y)$ is a random process uniformly distributed in $[-\pi, \pi]$ with a power spectral density exhibiting 3 dB cutoff at angular frequency W_0. This is reasonable given that phase is frequently modeled as uniform noise, and that it is quite correlated, if we neglect instrumentation noise. Let $\delta(k_x, k_y) = c(\triangle_x k_x + \triangle_y k_y)$ be the phase term due to translation. Let $\phi(k_x, k_y)$ be the original phase before motion, and $\phi'(k_x, k_y)$ be the phase after motion. Figure 3.7 depicts the situation for a single k-space point. Position A is the original k-value, and position B is the k-value after translation of K_2 by $(\triangle_x, \triangle_y)$, causing a phase shift δ. The indices (k_x, k_y) have been dropped for simplicity. Theorem 3 summarizes and proves our main result.

Theorem 3.3 *Let δ, ϕ, ϕ' and $\triangle\phi$ be defined as above, and let the phases of components K_1 and K_2 prior to translation be ϕ_1 and ϕ_2 respectively. Let $\alpha =$*

$|K_2|/|K|$ *be the ratio of the moving signal strength to the overall signal strength. Then*

$$\triangle\phi = \arcsin\left(\frac{\alpha(\sin(\phi-\phi_2)+\sin(\phi_2-\phi+\delta))}{\sqrt{1+4\alpha^2\sin^2(\delta/2)+4\alpha\sin(\phi-\phi_2-\delta/2)\sin(\delta/2)}}\right), \tag{3.6}$$

PROOF: In figure 3.7 angle $\angle AOX$ is the original phase ϕ and $\angle ACB = \delta$. We wish to find $\angle AOB = \triangle\phi$, the phase difference. The displacement caused by motion is given by

$$\overline{AB} = 2K_2\sin(\delta/2), \tag{3.7}$$

where $\overline{AB}$ denotes the distance between A and B. Now $\angle AOC = q = \phi_2 - \phi$ and $\angle BAC = \pi/2 - \delta/2$. Therefore $\angle BAO = \pi/2 - \delta/2 - q$. Using the Law of Sines on triangle $\triangle OBA$, we get

$$\sin(\triangle\phi) = \frac{\overline{AB}}{|K'|}\sin(\angle BAO). \tag{3.8}$$

Using the Law of Cosines on $\triangle OBA$, we obtain

$$|K'| = \sqrt{|K|^2 + \overline{AB}^2 - 2K\overline{AB}\cos(\angle BAO)}. \tag{3.9}$$

Finally, combining (3.7), (3.8) and (3.9) we get after simplification,

$$\sin(\triangle\phi) = \frac{2K_2\sin(\delta/2)\cos(p+\delta/2)}{\sqrt{K^2+4K_2^2\sin^2(\delta/2)-4KK_2\sin(\delta/2)\sin(p+\delta/2)}}. \tag{3.10}$$

Using $\alpha = |K_2|/|K|$ in above, we obtain (3.6). Although $\triangle\phi$ was derived only for the first quadrant of the complex plane, and for increasing δ, the same result obtains in all cases.

The general spectral analysis of (3.6) is difficult. Instead we present results on important special cases corresponding to $|K_1| >> |K_2|$, $|K_1| = |K_2|$ and $|K_1| << |K_2|$, covering all scenarios. As in figure 3.7, let $p = \phi - \phi_1$and $q = \phi_2 - \phi$. From the Law of Sines, we get: $\sin(p)/|K_2| = \sin(q)/|K_1|$. Hence for small K_1, q is small;

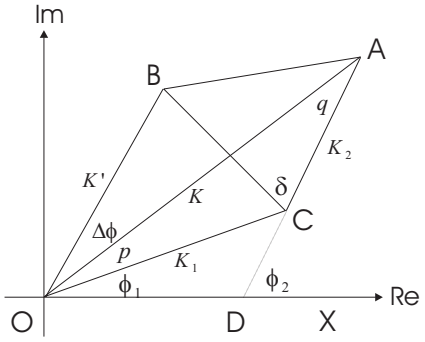

Figure 3.7: Relationship between phase difference $\triangle\phi$ and translation phase shift δ

conversely, for small K_2, p is small. We will model p and q as random uniformly distributed processes with 3 dB bandwidth of W_0, like the overall phase.

3.4.4 Special Case 1: K_2 is small

We have $\alpha \ll 1$, $|p| \ll 1$, which gives, from equation (3.6), $\triangle\phi \approx \alpha(-\sin(q) + \sin(q+\delta))$ using $sin(x) \approx x, |x| \ll 1$. From Law of Sines and $|p| \ll 1$, it can be shown that

$$\triangle\phi \approx \alpha\{\sin(\delta) + (p/\alpha)(\cos(\delta) - 1) - \frac{1}{2}(p/\alpha)^2 \sin(\delta)\}. \tag{3.11}$$

It is easy to verify that p/α is approximately uniformly distributed in $[-\pi, \pi]$. $\triangle\phi$ consists of a sinusoid in k-plane, and random phase signals modulated by the sinusoid. The sinusoid is at the angular frequency of $(c\triangle_x, c\triangle_y)$ in (x, y)-plane, and the PSD (power spectral density) of $\triangle\phi$ is predominantly clustered around this frequency. In fact it is easy to show that the residual power of the phase signal outside the (two-dimensional) frequency band $[-(W_0 + c\triangle_x), W_0 + c\triangle_x] \times [-(W_0 + c\triangle_y), W_0 + c\triangle_y]$ is $\mathcal{O}(\alpha^2)$, and may be neglected for small α. To corroborate our conclusion, we present in figure (3.8)(a) a typical power spectrum corresponding to

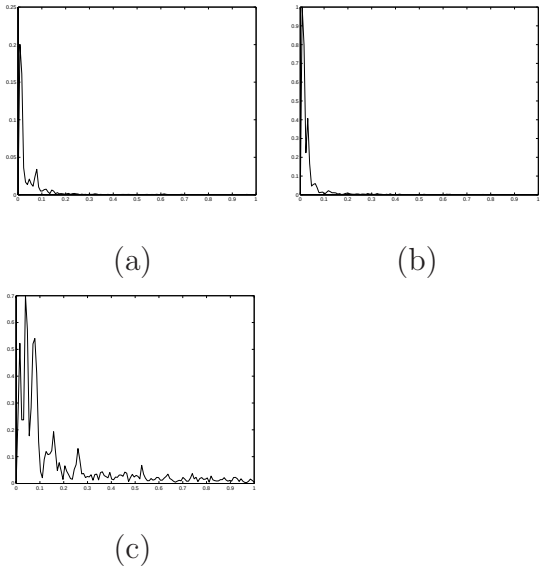

(a) (b)

(c)

Figure 3.8: Averaged power spectra of phase signals: (a) Case A, $\alpha = |K_2|/|K| = 0.2$; (b) Case B, $\alpha = 0.9$; (c) General intermediate case, $\alpha = 0.7$.

this case. The power spectrum was arrived at for $\alpha = 0.2$, as follows. Traversing a typical k-space frame in the frequency-encode direction, we acquired several one dimensional phase signals. These phase signals were used to model the stochastic signal p in (3.11). Then we used (3.11) to produce corresponding phase difference signals. Power spectra of each of these signals was obtained using Welch's averaged periodogram method [Wel67]. Figure (3.8)(a) was obtained after averaging these power spectra to produce a relatively noise-free representative power spectrum. The frequencies are normalized to fall between 0 and 1, with the latter corresponding to the Nyquist rate. The signal has predominantly low frequencies, along with a modulation portion centered at the frequency of the phase sinusoid, at normalized frequency of 0.08, corresponding to 8 percent translation in the field of view (FOV).

3.4.5 Special Case 2: K_1 is small

We have $\alpha \approx 1$, $|q| \ll 1$. Let $\beta = |K_1|/|K| \ll 1$. Equation (3.6) reduces to

$$\triangle\phi \approx \arcsin\left(\sin(\delta) + \beta(q/\beta)\cos(\delta)(\cos(\delta) - 1)\right), \tag{3.12}$$

after expanding the denominator of (3.6) as a binomial series and neglecting higher order terms. As before, q/β is a random process uniformly distributed in $[-\pi, \pi]$. Since the second term is quite small, we can expand the above in a Taylor series for $\arcsin(\cdot)$ about the point $\sin(\delta)$. We then have, after neglecting higher order terms,

$$\triangle\phi \approx \delta + \beta(q/\beta)(\cos(\delta) - 1). \tag{3.13}$$

Therefore, the phase difference in this case is basically a linear ramp function, with a small amount of a modulated random signal of bandwidth W_0. The residual power outside frequency band $[-(W_0+c\triangle_x), W_0+c\triangle_x]\times[-(W_0+c\triangle_y), W_0+c\triangle_y]$ is $\mathcal{O}(\beta^4)$, and can be safely neglected. Figure (3.8)(b) presents corroborating evidence for our conclusion. It was obtained in the same way as described in Case 1, with $\alpha = 0.9$, and 8 percent translation.

3.4.6 Special Case 3: K_1 and K_2 are equal

From figure 3.7 it is easy to show, using basic circle geometry, that

$$\triangle\phi = \delta/2. \tag{3.14}$$

This is an interesting result, since it indicates that the phase difference is independent of the phase, and is constant! In any case, this is a linear ramp in k-space, and therefore also lies in the low-frequency region.

We have shown that if K_2 is much larger, smaller or equal to K_1, then the phase difference in each case is predominantly low-frequency. It is therefore reasonable to expect that this will continue to be the case for intermediate cases as well. This is experimentally corroborated by figure (3.8)(c), which shows a typical PSD corresponding to $|K_2|/|K| = 0.7$.

3.5 Results

3.5.1 Materials and methods

The following data were obtained at 1.5 Tesla with a head coil for signal transmission and reception (LX Horizon, General Electric Medical Systems). Patients were placed feet-first into the magnet with the legs positioned within the head coil to image from above the patella down to mid-calf. A sagittal gradient echo scout sequence was used to position the coronal 2D projection MRA slab so that it encompassed the entire calf. The 2D projection MRA was performed as a coronal spoiled gradient echo sequence using the following parameters: TR/TE/ip angle = 10/2/60 degrees, slab thickness = 7-10 cm, field-of-view = 30cm, matrix = 256x192, bandwidth = 16 kHz. The imaging time was 1.95 seconds per acquisition, repeated 35 times for a total of 67 seconds. Gadolinium contrast (5-7 ml at 0.5mol/L) (Magnevist, Berlex Laboratories, Wayne, NJ; Omniscan, Nycomed Amersham, Princeton, NJ) was injected and flushed with 20 ml saline. The injection rate was 2.5ml/sec by hand with a SmartSet (TopSpins, Ann Arbor, MI) or using an automatic injector (Spectris MR Injector, MedRad, Pittsburg, PA). The injection was initiated simultaneously with image acquisition.

3.5.2 In-plane motion in a single frame: Simulation Results

Several experiments were conducted to test the operation of the POCS algorithm on removing motion artifacts from a single frame within the sequence. For the purpose of comparison, various kinds of motion were simulated and applied on an otherwise well-registered and motion-free MRA sequence. The first example demonstrates POCS results on step-like translational motion as a function of the PE index, shown in figure 3.9. The translation was non-global - only a part of the image was caused to move 2 pixels in both the PE and FE directions. In this example, half of the image undergoes translation after almost half the (Cartesian) k-space lines have been acquired. This case is exceedingly difficult to correct for by most current algorithms, since the motion is non-global and has occurred in the middle of the k-space scan. The results are shown in figure 3.9. The uncorrupted frame (a) is just prior to the corrupted frame (b) in the MRA sequence. The effect of the translation is too small to be easily discerned from the actual scans as shown here, but the resulting *difference* image, i.e. the angiogram shown in (d) clearly has significant artifacts when compared to the uncorrupted angiogram shown in (c). These artifacts make the angiogram quite useless diagnostically. This is a good example of the extreme sensitivity of 2D MRA to even small amounts of motion. Part (e) shows the result of the POCS motion correction algorithm applied on the motion corrupted MRA sequence. Clearly the algorithm has been able to recover almost all features present in the original uncorrupted angiogram while removing motion artifacts. The result was obtained after three iterations with relaxation factor of $\lambda = 0.8$.

Figure 3.10 shows another non-global translation example. The amount of translation was chosen to be large — around a quarter of FOV in the PE direction.

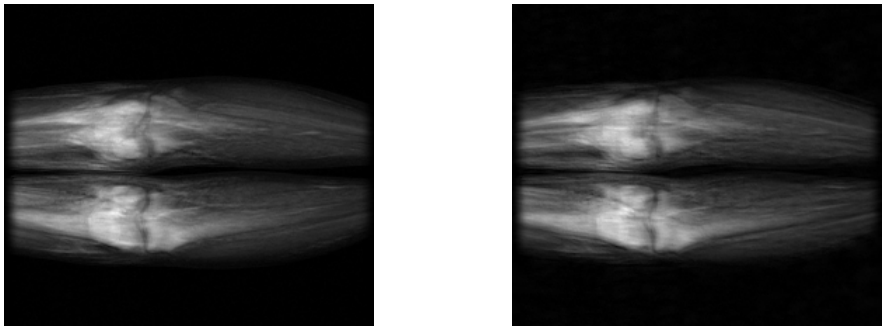

(a)

(b)

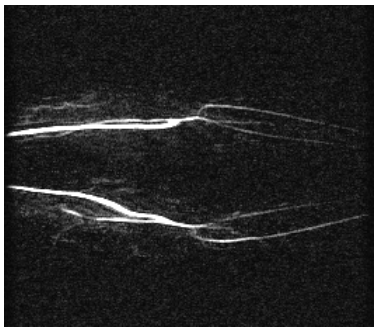

(c)

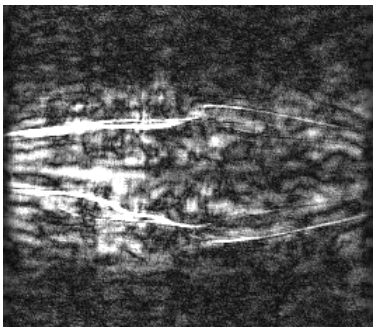

(d)

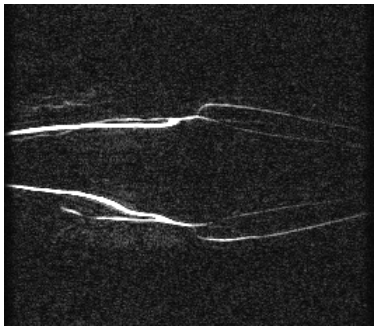

(e)

Figure 3.9: Example of non-global step translation occurring in middle of k-space acquisition: (a) Uncorrupted frame, (b) Corrupted frame, (c) Original angiogram, (d) Motion-corrupted angiogram, and (e) Corrected using POCS, with $\lambda = 0.8$

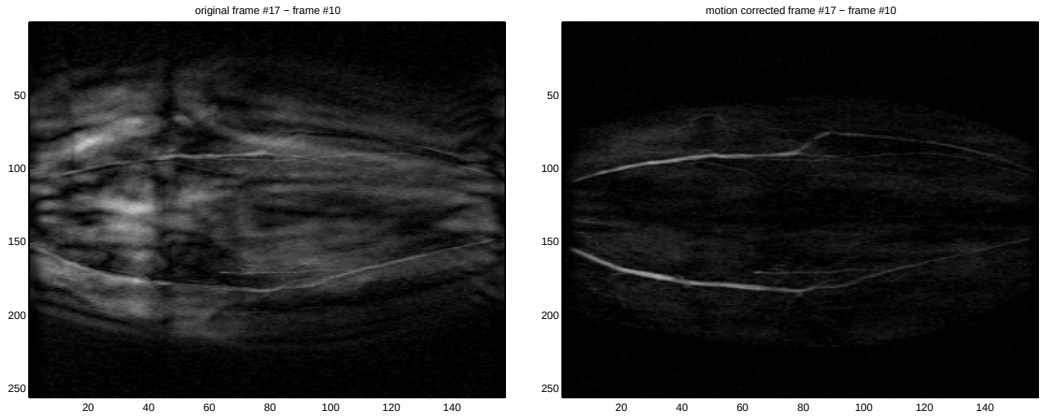

(a) (b)

Figure 3.10: Motion Correction (a) Motion Corrupted Difference Image, and (b) Corrected using POCS Algorithm, with $\lambda = 0.8$

The result was obtained after three iterations with relaxation factor of $\lambda = 0.8$.

The next example introduces a random walk type non-global translation. The amount of translation, in pixels, is plotted with respect to the PE index in figure 3.11, which shows both the translation in the PE and FE directions. The step size at each point was sampled from a zero mean Gaussian to model erratic or involuntary motion. Only a small part of k-space (PE lines) are affected by this motion. Again the translation was non-global - only a part of the image was allowed to move. This example is more difficult than the step motion in earlier examples since the amount of translation varies rather erratically from one PE line to the next. However, the POCS algorithm is designed to compare phase artifacts in k-space on a line-to-line basis, thus is equally successful at removing this artifact as the earlier examples, as demonstrated in figure 3.12.

The final single-frame motion example, shown in figure 3.14, introduces an additional non-global rotation on top of the translation artifacts in figure 3.9. We

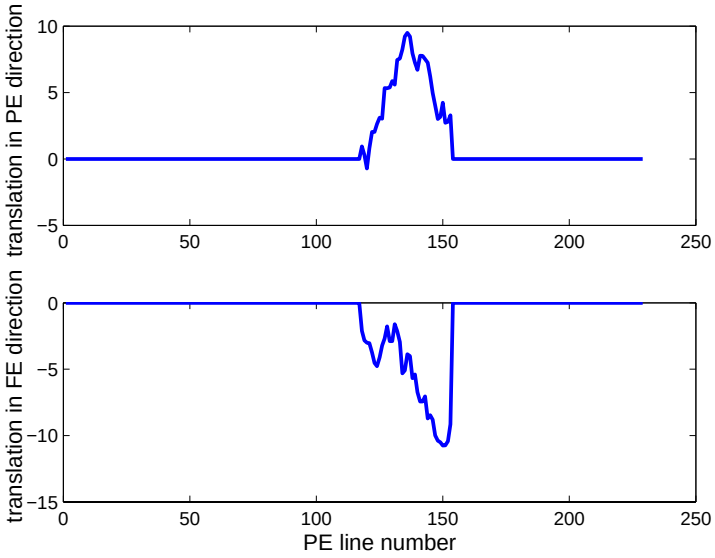

Figure 3.11: Non-global random-walk translation, plotted as a function of the phase encode index. The top curve shows translation in the PE direction, while the bottom curve shows translation in FE direction.

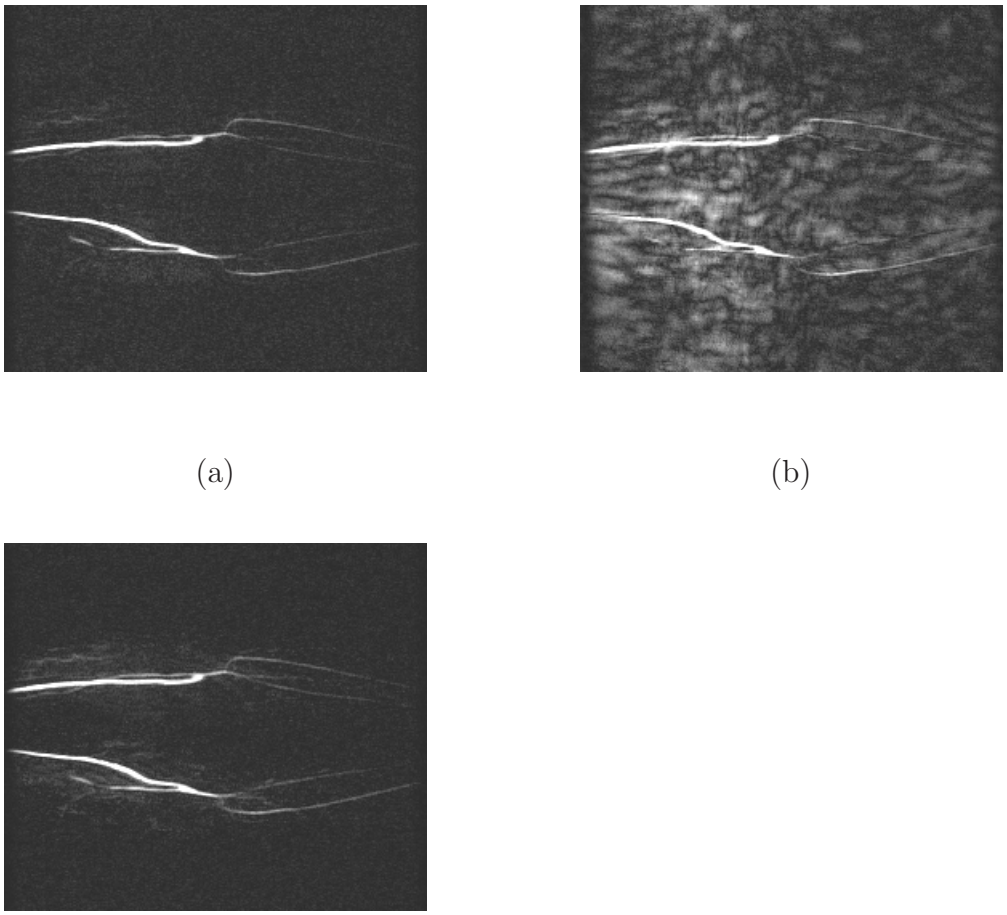

(a) (b)

(c)

Figure 3.12: Example of non-global random-walk translation occurring in middle of k-space acquisition: (a) Original angiogram, (b) Motion-corrupted angiogram, and (c) Corrected using POCS Algorithm, with $\lambda = 0.8$

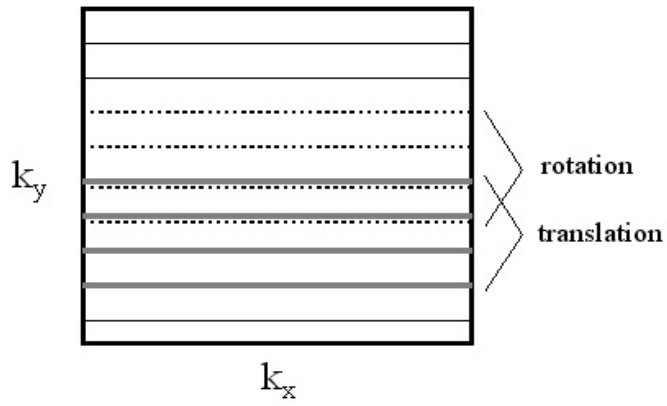

Figure 3.13: Combined non-global rotation and translation mapped in k-space

allowed the left leg only to rotate by a small amount, roughly 15 degrees counter-clockwise. This was simulated to occur while the middle portion of k-space was being acquired. In terms of PE lines covered, the rotation duration overlapped with the translation duration, but did not coincide with the latter. This is shown in figure 3.13. The effect of rotation of the left leg is visible in the top half of the angiogram, which shows mis-registration errors roughly aligned 15 degrees from the axis. But this is not simply a matter of mis-alignment - since the rotation is not global and only occurs in a portion of k-space, it produces artifacts much more disturbing and challenging than a simple rotational mis-alignment would produce. As a result, conventional image-based motion compensation schemes are not likely to succeed. The POCS method is able to remove most of these artifacts, after only 4 iterations.

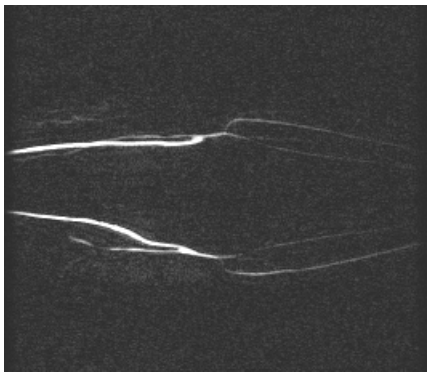

(a)

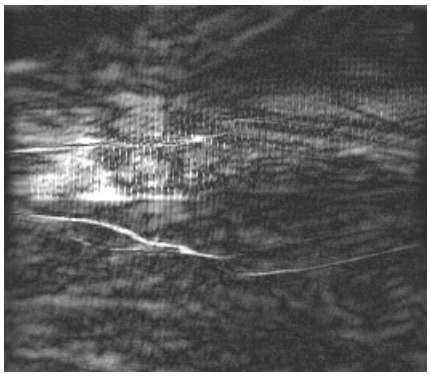

(b)

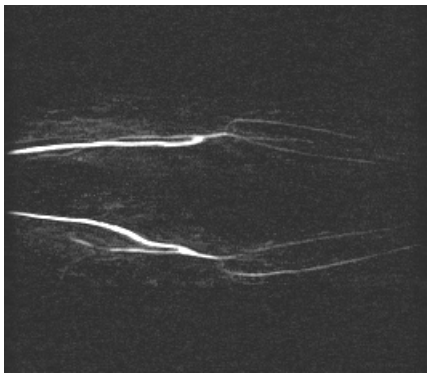

(c)

Figure 3.14: Non-global rotation as well as translation, both occurring in middle of k-space acquisition: (a) Original angiogram, (b) Motion-corrupted angiogram, and (c) Corrected using POCS Algorithm, with $\lambda = 0.8$

3.5.3 Completely un-supervised clinical MR-DSA: a joint classification and motion correction algorithm

In clinical practice, after acquisition the MRA sequence is analysed laboriously by radiologists. Each frame is viewed, and estimates of contrast arrival, arterial phase (post-contrast), mask phase (pre-contrast) and venous phase are empirically obtained. Then frames are evaluated according to their quality, and any motion-corrupted frames are rejected, more or less by trial and error. Then the final angiogram is obtained by subtracting the set of "good" mask frames from "good" arterial phase frames. A new, automatic MR-DSA algorithm was recently proposed by Kim *et al.*[KPZ+02] to automate this time-consuming procedure. In this section we investigate an extension of this method by incorporating the POCS-based motion correction algorithm within the automated MR-DSA classification algorithm. This attempts to remove a major source of error in the work in [KPZ+02], which was extremely sensitive to motion artifacts. Our unsupervised method performs motion correction on all frames of all cases. This is obviously both unnecessary as well as potentially harmful for cases and frames that do not suffer from noise. However, this approach was necessitated by the fact that the MR-DSA algorithm did not provide adequate indication of motion corruption. We also wish to demonstrate that our method is designed to retain radiologically important information. Clearly, if angiogram quality is degraded if the POCS method is applied on non-corrupted cases, then that would be a useful piece of information which would help decide in which situations the method should be applied.

Real clinical cases were obtained from data collected in a recent comparative study [KPZ+02]. The authors have investigated many peripheral MRA clinical cases and used a panel of radiologists to identify cases and frames which have mo-

tion. They have produced a database containing the best angiograms produced by expert radiologists for each case. The images of 47 consecutive patients who underwent peripheral MRA including 2D projection MRA of the trifurcation from September 11, 2000 to November 25, 2000 were obtained using both manual image selection and the automatic MR-DSA algorithm. These patients included 26 males aged 24 - 87 (mean 70) years and 19 females aged 33 - 85 (mean 68) years. The primary indications for peripheral MRA in these patients included claudication (n=23), limb threatening ischemia (n=11), aneurysm (n=7), post-bypass graft (n=3), and dissection (n=1). This study was approved by Weill-Cornell's Institutional Review Board.

In this section we will compare these images with our automatically motion corrected angiograms obtained from the same data sets. Figure 3.15(a) shows the difference image obtained manually by an expert radiologist, and (b) shows the corresponding image produced after removal of motion artifacts using the POCS algorithm. We have implemented an automatic algorithm that uses software developed earlier by Kim (see [Kim03], Ch. 2 for details) which classifies post-contrast and pre-contrast frames, and also identifies frames corrupted by motion using a simple motion metric. Our automatic technique then recomputes the best angiogram after including all the frames, even those that would previously have been discarded due to motion. Significant improvement in visual quality as well as SNR of the images was observed in most cases exhibiting motion artifacts. Figure 3.15(b) was obtained after three iterations with relaxation factor of $\lambda = 0.8$.

Our next example, shown in figure 3.16, illustrates the suppression of background clutter caused by motion. The corrected angiogram has much improved contrast and definition.

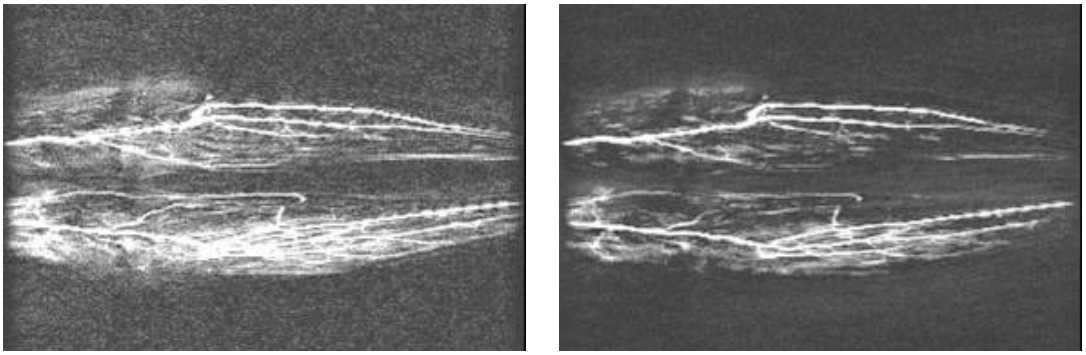

(a) (b)

Figure 3.15: Motion Correction of clinical peripheral MRA case (a) Motion Corrupted Difference Image, and (b) Corrected using POCS Algorithm, with $\lambda = 0.8$

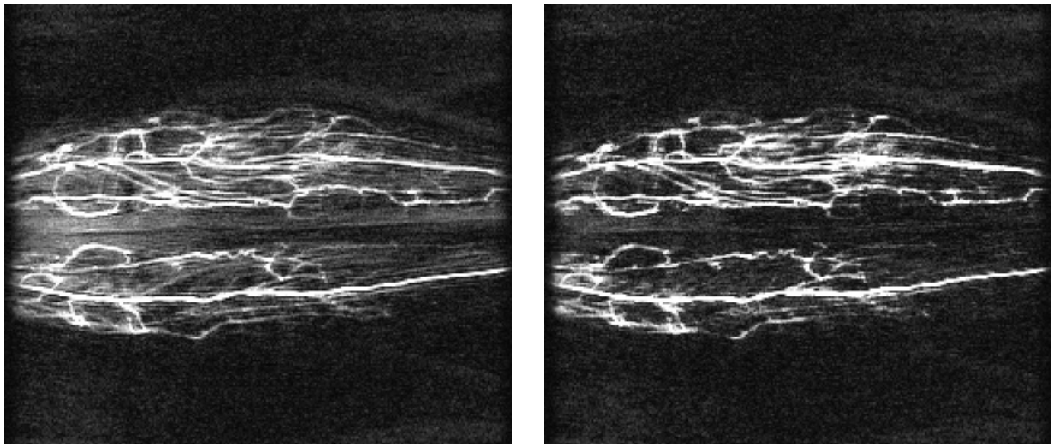

(a) (b)

Figure 3.16: Clinical peripheral MRA example (a) Best manual angiogram, and (b) Output of automatic POCS algorithm

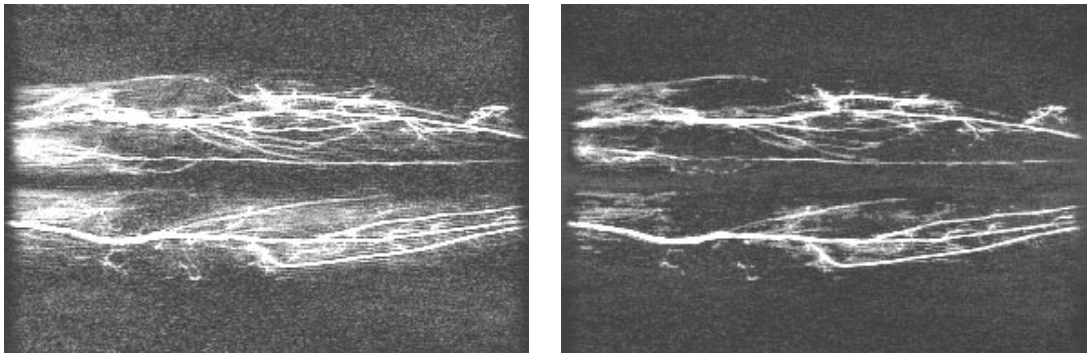

(a) (b)

Figure 3.17: Another example: (a) Best manual angiogram, and (b) Output of automatic POCS algorithm

The example in figure 3.17, shown at a different contrast and saturation level, shows up some limitations of the POCS algorithm. While there is significant clutter reduction, there seems to be some loss of extremely fine or faint arterial features. This example illustrates the need to strike a good balance between motion suppression and loss of some fine features. On the other hand, the definition and contrast of major arteries is enhanced by our method.

These examples suggest that motion correction inevitably involves some loss of fine details despite careful design of the algorithm to prevent it. As such, the method should only be used in cases where significant motion has occurred. Also, since the best angiogram is obtained by averaging operations on the data set, the removal of artifacts from individual frames may not necessarily lead to commensurate improvement in the final angiogram.

In addition to visual evidence, an extensive double-blind comparative study was conducted to validate the technique. A set of randomized image pairs was presented to an experienced radiologist, one obtained manually by a specialist, and

the other obtained automatically by our technique as described above. A total of 47 cases were studied. The results are shown in Table 3.1. The mean score was 2.74, on a scale from 1 to 5, with 1 denoting cases where the automatic POCS algorithm performs much better than manual, and 5 denoting manual performing much better than POCS. It is noteworthy that the number of cases where our result was deemed better than the manually obtained result (25) exceeds the number of cases where manual result outperformed our result (16). The last number mainly corresponds to those cases which did not have motion artifacts to begin with, and whose fine features got slightly degraded by the POCS algorithm which was attempting to remove motion that was not there. Yet overall, the automatic method still does significantly better than manual method. A two-tailed two-sample (paired) t-test was conducted on the scores in the table. At 5% level of significance, the quality score of POCS-corrected angiograms was found to be significantly better than manually obtained angiograms ($t(92) = -2.45, \quad p = 0.0162$). Clearly, such a small p-value indicates significant improvement for real clinical cases. This presents a strong justification for using the un-supervised method presented here in clinical MRA exams, perhaps with some operator intervention to identify corrupted cases. While our results do not indicate improvement over manual methods in all cases, it may be pointed out that instances in the literature of completely automatic algorithms even partially outperforming data obtained by an experienced medical practitioner are relatively rare.

3.5.4 Limitations and further improvements

While there is strong visual and statistical evidence of the success of our method, we also encountered several problems during the experimental evaluation. The

Table 3.1: Results of a Double Blind Comparison of Manual versus Automatic POCS Angiograms

$POCS >> man$	$POCS > man$	$same$	$POCS < man$	$POCS << man$
3	22	6	16	0

main problem with the POCS algorithm remains the fact that in order to remove artifacts resulting from motion, especially arbitrary 3D motion, it is frequently necessary to constrain the time evolution of certain features in the complex frames. We have provided theoretical and empirical evidence that the POCS algorithm usually leads to only small amounts of degradation of vascular enhancement. However, the fact remains that the two goals of preserving useful data and removing artifacts are in a way mutually contradictory — there is always some, albeit small, loss of vascular definition during the process. This problem manifests itself most often when excessive amounts of artifacts bury small, fine vascular features. In such cases one may have to settle at a conservative correction if one is interested in these fine features. In other words, one must decide on the trade-off between background motion clutter and resolution of fine features on a case-by-case basis. This suggests the need for some operator involvement in selecting this trade-off point. The automatic technique presented here relies on the accuracy of the mask and arterial phase selection algorithm, called MR-DSA [KPZ$^+$02]. Work currently underway by several workers in this and other labs will likely result in dramatic improvement in the MR-DSA classification algorithm, which will produce a corresponding improvement in the performance of the proposed automatic motion correction method. In the meantime, our correction method can be applied in the non-automatic mode, where an operator selects arterial and mask phases and iden-

tifies frames corrupted by motion. Further improvements may result from a hybrid of the proposed method with other motion correction schemes like navigators or parameter tracking methods. Work is continuing in this direction.

3.6 Conclusion

We have described a convex projection-based algorithm that corrects a motion corrupted frame by iteratively making it more similar to a non-corrupted one. The algorithm is able to identify and partially correct corrupted features of k-space and thereby remove artifacts due to complex non-global or non-rigid motion. Radiologically important temporal events are not degraded by the successive projections. The technique has the potential to retrieve corrupted angiography data that would otherwise be unusable due to motion artifacts. Simulated and clinical examples present visual evidence of the efficacy of our method. The POCS algorithm, after being incorporated into a completely automatic program, was found to yield automatic angiogram results that were judged to show significant improvement over manually obtained angiogram during a double-blind comparative study. The method can be extended to 3D data, and is able to incorporate additional motion correction innovations within the general POCS framework.

Chapter 4

Total Least Sense: A Maximum - Likelihood Approach to Parallel MR Imaging with Sensitivity Noise

Parallel imaging is a powerful technique to speed up Magnetic Resonance (MR) image acquisition via multiple coils. Each coil subsamples in k-space at the cost of introducing aliasing. The output of the coils, plus the sensitivity maps that describe the different responses of each coil, can then be combined to produce a non-aliased image. Widely used parallel imaging methods such as SENSE and its variants assume that the coil outputs contain noise, but that the sensitivity maps are noiseless. In practice, however sensitivity maps are subject to a wide variety of errors. At first glance, sensitivity noise appears to result in an errors-in-variables problem of the kind that is typically solved using Total Least Squares (TLS). However, existing TLS algorithms are inappropriate for the specific type of block structure that arises in parallel imaging. Here we take a maximum likelihood approach to the problem of parallel imaging in the presence of independent Gaussian sensitivity noise. This results in a quasi-quadratic objective function, which can be efficiently minimized. Experiments demonstrate that our method produces substantial SNR gains over current methods.

4.1 Parallel Imaging and Sensitivity Noise

Magnetic resonance imaging involves a fundamental trade-off between image quality and scan time [WBP04]. As described in chapter 2, parallel imaging techniques like SENSE [PWSB01], SMASH [MOY+01] and GRAPPA [WND+03] use multiple coils to reduce scan time. Our work concentrates on the SENSE technique since it is widely recognized as the most general and powerful one. The sensitivity maps of receiver coils are used to encode the imaging volume. These sensitivity maps are typically obtained by scanning with a phantom. The outputs of each coil can be combined with the sensitivity maps to reconstruct a full, unaliased image. Recall that the reconstruction algorithm used by SENSE assumes that the output of the receiver coils has been corrupted by noise, and can be modeled as

$$\mathrm{y} = E\mathrm{x} + \mathrm{n}, \tag{4.1}$$

where n is Gaussian noise, assumed to be independent and identically distributed (i.i.d.). This noise may arise, for example, from instrumentation error. The SENSE method takes a least squares approach, which is natural under these assumptions. Note that the least squares solution is well-known to be the maximum likelihood estimate [PTVF92, Ch. 15], again assuming this noise model.

In this chapter we address a major shortcoming with SENSE, which is the assumption that the sensitivity maps are noiseless. The sensitivity maps, however, are computed from an MR scan, typically of a phantom. As a result, they are subject to almost the same noise processes that affect the coil outputs during the scans of the patients. This is not just a theoretical argument; we will demonstrate in section 4.4 that our reconstruction method, which handles sensitivity noise, gives significantly better experimental results.

As mentioned in chapter 1, we model the imaging process as

$$\mathrm{y} = (E + \Delta E)\mathrm{x} + \mathrm{n}, \tag{4.2}$$

where ΔE is the noise in the system matrix that results from errors in the sensitivity maps (i.e., sensitivity noise). At first glance, this appears to be an errors-in-variables problem of the kind commonly addressed with Total Least Squares (TLS) [HL02]. Indeed, several authors, such as [LBJ+02], have suggested taking a TLS approach to sensitivity error. However, TLS algorithms assume that ΔE consists of independent elements. The discussion of noise model in section 2.2 demonstrates that this assumption is invalid, due to the block structure of the system matrix E in parallel imaging.

We propose a maximum likelihood approach to solving equation (4.2). Maximum likelihood can be viewed as a generalization of both least squares [PTVF92] and total least squares [HL02]. We use the natural model for sensitivity errors, where each pixel in the sensitivity map is corrupted by i.i.d. noise. The resulting algorithm, which we call TL-SENSE, gives strong results, even in cases where our assumed noise model is incorrect. We show a couple of examples later where the sensitivity errors do not follow the assumed model, but are still mitigated by our method. A reasonable explanation for this phenomenon is that while out i.i.d. noise assumption may be inaccurate for these cases, it is still much better than the conventional assumption of *zero* sensitivity errors. This is by no means a novel observation - for many years workers in signal processing, radar systems and mobile communications, to give a few examples, have used i.i.d. Gaussian models to great effect, even in cases where they are demonstrably inaccurate.

The rest of this chapter is organized as follows. We present our system model (from §2.2) and our model for sensitivity noise. In §4.2 we discuss related work, and

show that sensitivity noise cannot be handled by standard methods such as TLS or its variants. Section 4.3 derives our new TL-SENSE algorithm from a maximum likelihood formulation. We also demonstrate that with Cartesian sampling the general solution can be considerably simplified, and results in a quasi-quadratic minimization problem directly in image space. We give experimental results on both simulated and clinical data in section 4.4.

Recall from §2.2 that he output of the l-th coil is

$$\mathrm{y}_l = E_l \mathrm{x} = \; D^H_{N\times M} \downarrow_R D_{N\times M} S_l \cdot X = \; D^H_{N\times M} \downarrow_R D_{N\times M} diag(\mathrm{s}_l)\mathrm{x}. \tag{4.3}$$

Also recall that the entire multi-coil output can be written as

$$\begin{aligned} \mathrm{y} &= [\mathrm{y}_1^T, \ldots, \mathrm{y}_L^T]^T, \\ E &= [E_1^T, \ldots, E_L^T]^T \end{aligned}$$

Similarly, the k-space version becomes

$$\begin{aligned} \bar{\mathrm{y}} &= [\bar{\mathrm{y}}_1^T, \ldots, \bar{\mathrm{y}}_L^T]^T, \\ \bar{E} &= [\bar{E}_1^T, \ldots, \bar{E}_L^T]^T \end{aligned}$$

4.1.1 System matrix structure under Cartesian sampling

The vast majority of MR scans are done with regular Cartesian sampling in k-space, which considerably simplifies the problem and produces a specific matrix structure. The 2-D DFT operator then reduces to two 1-D DFT's acting separately on rows and columns. The general-purpose k-space sampling operator $\downarrow_R$ in equation (4.3) is now redefined as a *sub-sampling* operator, equivalent to removing rows of k-space.

Writing $D_{N\times M} = D^{row}_M D^{col}_N$ as the explicit row and column 1-D DFT operations, since $\downarrow_R$ only acts on columns, we have $\downarrow_R D_{N\times M} = D^{row}_M \downarrow_R D^{col}_N$. The output

image is now $\frac{N}{R} \times N$, and equation (4.3) can be rewritten as

$$\mathrm{y}_l = \ (D^{col}_{N/R})^H \downarrow_R D^{col}_N diag(\mathrm{s}_l)\mathrm{x}, \tag{4.4}$$

This equation can be solved separately for each column.

Since the downsampling is regular, it is easy to show that

$$\downarrow_R D^{col}_N = D^{col}_{N/R}[I_{N/R} \cdots I_{N/R}], \tag{4.5}$$

which is the concatenation of R identity matrices of size $\frac{N}{R}$.

Equation (4.5) leads immediately to the partitioning of E_l, the system matrix corresponding to the lth coil:

$$E_l = [E^1_l, \ldots, E^R_l] \tag{4.6}$$

Therefore the full system matrix E has a diagonal-block structure containing $L \times R$ diagonal blocks:

$$E = \{E^r_l\} \quad \begin{matrix} r=1\ldots R \\ l=1\ldots L \end{matrix} \tag{4.7}$$

where each sub-block E^r_l is diagonal from (4.4). This is shown in figure 4.1. Vectors $\mathrm{y}^{(i)}_l$, $\mathrm{s}^{(i)}_l$ and $\mathrm{x}^{(i)}$ are the i-th column of Y_l, S_l and X, all in spatial domain.

As shown in the figure, the system matrix E is partitioned, which leads to a natural partitioning of $\mathrm{x}^{(i)}$ into R aliasing components:

$$\begin{aligned} \mathrm{x}^{(i)} &= [\mathrm{x}^{(i)^T}_1 \cdots \mathrm{x}^{(i)^T}_R]^T \\ \mathrm{s}^{(i)}_l &= [\mathrm{s}^{(i)^T}_{l\ 1} \cdots \mathrm{s}^{(i)^T}_{l\ R}]^T. \end{aligned}$$

Then from (4.4) and (4.5) we have, for each column i,

$$\mathrm{y}^{(i)}_l = \sum_{r=1}^{R} \mathrm{s}^{(i)}_{l\ r} \cdot \mathrm{x}^{(i)}{}_r. \tag{4.8}$$

Figure 4.2 shows the structure of $\bar{E}$, the Fourier dual of E.

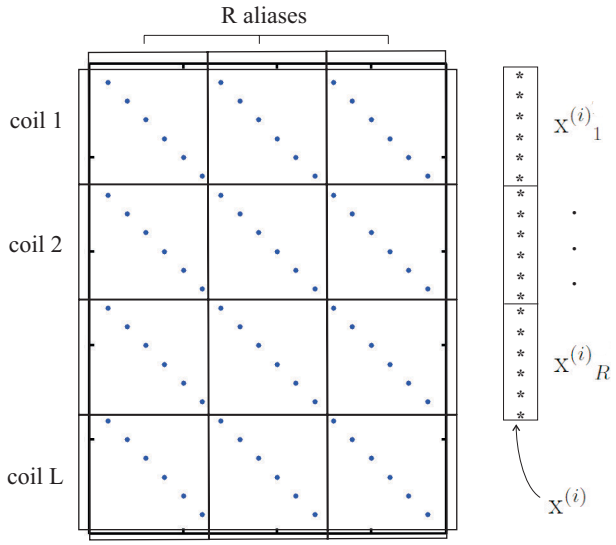

Figure 4.1: Structure of matrix E under regular Cartesian sampling. Non-zero elements are indicated with an asterix. As a consequence of the partitioning, image column $x^{(i)}$ separates into R aliasing components

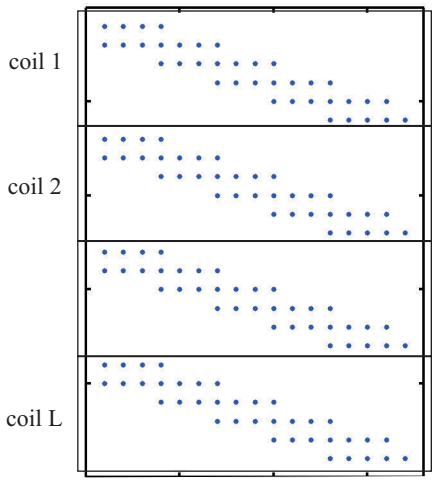

Figure 4.2: Structure of matrix $\bar{E}$ under regular Cartesian sampling

To maintain readability, we will henceforth drop the superscript (i) denoting the ith column. We will use the same symbols E, x and y etc. both for arbitrary and Cartesian sampling, with their meaning being indicated from the context.

4.1.2 System matrix structure under arbitrary sampling

The system matrices E, $\bar{E}$ have important special forms. The individual blocks $\bar{E}_1, \ldots, \bar{E}_L$ have a Toeplitz structure as shown in figure 4.2, but they have been decimated by the sampling. (Recall that a Toeplitz matrix is a matrix $T = T_{ij}$ such that $T_{ij} = \mathrm{t}_{j-i}$ for a given row vector t.) If the sampling were not present, the matrix $\bar{E}$ would have Toeplitz block structure.

The Toeplitz-type structure of each block results from the convolution operation in k-space. The decimation of rows results from the subsampling of data points in k-space. The structure of the corresponding image-space matrix E can be determined from (4.3) for arbitrary k-space sampling. Unlike the simple closed-form diagonal-block structure that arises in Cartesian sampling, this structure can be quite complicated as it depends on the sampling trajectories used.

4.1.3 Our noise model

We use the obvious noise model of i.i.d. Gaussian noise both for sensitivity and instrumentation noise. We note that the Gaussian assumption is only valid for complex data; once an actual image is obtained by discarding phase information, the noise process accociated with such images is well-known to be Rician rather than Gaussian [GBD04]. Here the quentities involved are complex, hence the Gaussian assumption is valid. For $l \in \{1, \ldots, L\}$, the noise model for the lth coil

sensitivity and output, respectively, is given by

$$S_l^{noisy} = S_l + N_l^s \tag{4.9}$$

$$Y_l^{noisy} = Y_l + N_l \tag{4.10}$$

where the output noise terms N_l are i.i.d. Gaussian with standard deviation σ_n, and sensitivity noise terms N_l^s are i.i.d. Gaussian with standard deviation σ_{n^s}. Let n_l and n_l^s be their vectorized representations.

Clearly, the structure of $\triangle E$ must mimic that of E shown in figure 4.1:

$$\triangle E = \{\triangle E_l^r\} \quad \begin{matrix} r=1\ldots R \\ l=1\ldots L \end{matrix}, \tag{4.11}$$

and the same holds for the k-space versions $\triangle \bar{E}$ and $\bar{E}$. Again, each sub-block $\triangle E_l^r$ is diagonal, with entries given by the sensitivity map noise terms N_l^s. Similarly, in k-space the error matrix $\triangle \bar{E}$ mimics the structure of $\bar{E}$ as shown in figure 4.2.

The assumption of Gaussian noise in spatial sensitivity measurement is actually quite a natural one, since sensitivity maps are usually obtained through an initial scan with a uniform phantom. As a result, the effects of measurement noise clearly carry over into sensitivity maps. The effect of this noise can frequently be exacerbated by further processing, like the common practice of dividing by the body coil output, or the sum-of-squares from all coils [PWBB01]. In addition, by using two separate scans for sensitivity and data, certain other small errors or discrepancies can creep in the actual sensitivity map as compared to the measured sensitivity maps.[1] In practical experiments involving phased array coils such discrepancies result from small changes in orientation and positioning of coils, coil loading effects, non-systematic coil and instrumentation errors, as well as a host

[1]This is why we explicitly allow for the noise variance of coil output and coil sensitivity to be different.

of other errors resulting from random noise. In the absence of a detailed and exhaustive error model for parallel imaging, the noise resulting from all these effects may reasonably be assumed to be i.i.d. Gaussian.

If the noise cannot be modelled accurately as i.i.d. white noise, or if the noise variance of the coils are different, it is easy to incorporate a more general non-identically distributed non-white noise model, by pre-multiplying E with a "whitening" matrix, as described above for coil output data. All correlation between different coils and sensitivity noise from the same coil can thus be removed, and we may continue using the i.i.d. Gaussian model.

4.2 Related Work

Equation (4.2) appears to be an errors-in-variables problem of the kind traditionally solved with TLS. Such methods appear not to have been applied to parallel imaging. This may result from the fact that TLS makes extremely unrealistic assumptions about the structure of the sensitivity noise. There are variants of TLS, such as Constrained Total Least Squares, that can handle a broad class of matrix structure, including the structures that arise in parallel imaging. However, these approaches require the use of very general minimization techniques, which are very inefficient.

4.2.1 Total Least Squares

The classical TLS theory [GL96] applied on (4.2) attempts to find a solution that minimizes both the additive noise n as well as the error-in-variables $\triangle E$, as follows:

$$\hat{x}_{TLS} = \arg\min_{x} || \ [\triangle E \mid \mathrm{n}] \ ||_F, \quad \text{subject to} \quad \mathrm{n} + \triangle E x = y - Ex \tag{4.12}$$

where the indicated norm is the Frobenius norm over a matrix obtained by concatenating $\triangle E$ and n. Note that this problem formulation assumes that the elements of $\triangle E$ are independent (i.e., that $\triangle E$ has no structure).

Unfortunately, TLS is ill-equipped to handle the specific system model described in §4.1.3. This is because E has a diagonal block structure as shown in figure 4.1, with off-diagonal elements in the constituent blocks being zero. The corresponding elements of $\triangle E$ will therefore also be zero. As a consequence, the independence assumption of TLS is always violated, even when the underlying sensitivity noise process is independent.

A similar situation results if one tries to perform classical TLS on the k-space imaging model (2.1). The system matrix $\bar{E}$ derives from the convolution operator, leading to a Toeplitz-type structure as shown in figure 4.2. This results in the elements of $\bar{E}$, and consequently the elements of $\triangle\bar{E}$, being algebraically related to each other, rather than being independent variables.

4.2.2 Constrained Total Least Squares

Several generalizations of TLS have been proposed which handle matrix structure. The best-known such technique is called *Constrained* TLS.[2] The Constrained TLS approach was proposed by [AMH91], whose work handles *linearly structured* matrices — those matrices that can be obtained from a linear combinations of a smaller perturbation vector.

For a linearly structured matrix E, the CTLS approach works as follows. Let $C = [E|y]$, and define a perturbation in C as $\triangle C = [\triangle E|n]$. CTLS consists of

[2] An earlier approach, called *Structured* TLS [MGK95], was shown to be equivalent to Constrained TLS in [LdMH96].

solving

$$\min_{v,x} ||v||, \tag{4.13}$$

subject to

$$(C + \triangle C) \begin{bmatrix} x \\ -1 \end{bmatrix} = 0$$

and

$$\triangle C = [F_1 v | F_2 v | \cdots | F_{N+1} v],$$

where the F_i's generate the elements of the linearly structured matrix ΔC. Note that this problem is difficult to solve for an arbitrary linearly structured matrix E, requiring the use of a general-purpose constrained minimization algorithm.

The system matrix that results from parallel MR (described in §2.2) turns out to be linearly structured. However, by taking advantage of the particular structure of the system matrix, we can use much more efficient special-purpose unconstrained minimization methods.

4.3 The TL-SENSE Algorithm

We will derive a formula for $\ell(\mathrm{x})$, the likelihood of an image x, using the system model and noise model of section 4.1.3. The TL-SENSE algorithm maximizes $\ell(\mathrm{x})$, which involves minimizing a quasi-quadratic objective function. Under Cartesian k-space sampling this objective function can be efficiently minimized using non-linear least squares.

4.3.1 Deriving the likelihood function $\ell(\mathrm{x})$

We now derive a formula for the likelihood $\ell(\mathrm{x})$ given the observed data y, which is by definition $Pr(\mathrm{y}|\mathrm{x})$. Define the total noise by $\mathrm{g(x)} = \mathrm{y} - E\mathrm{x}$. Under the noise

model described in section 4.1.3, this is jointly Gaussian with zero mean. As a result, and we can express the likelihood as

$$\ell(\mathrm{x}) \propto \exp(-\frac{1}{2}\{(\mathrm{y} - E\mathrm{x})^H R_{\mathrm{g|x}}^{-1}(\mathrm{y} - E\mathrm{x})\}) \tag{4.14}$$

where $R_{\mathrm{g|x}} = \mathcal{E}((\mathrm{g}(\mathrm{x}))(\mathrm{g}(\mathrm{x}))^H)$ is the covariance matrix of the conditional noise $\mathrm{g}(\mathrm{x})|\mathrm{x}$.

The maximum likelihood estimate, which we will denote $\hat{\mathrm{x}}$, minimizes $-\log \ell(\mathrm{x})$, and is given by

$$\hat{\mathrm{x}} = \arg\min_{\mathrm{x}} (\mathrm{y} - E\mathrm{x})^H R_{\mathrm{g|x}}^{-1}(\mathrm{y} - E\mathrm{x}). \tag{4.15}$$

Under our noise model, $R_{\mathrm{g|x}} = \mathcal{E}(\mathrm{nn}^H + (\triangle E\mathrm{x})(\triangle E\mathrm{x})^H)$, and $\mathcal{E}(\mathrm{nn}^H) = \sigma_n^2 I$. Note that we have omitted the $det(R_{\mathrm{g|x}}^{-1})$ term, for several reasons. This term results in an additional log term, making the overall cost function very expensive to compute and analyse. However, the incremental benefit of including this term is quite small since a log function does not increase as fast as the the rest of the cost function, and can be safely neglected, especially when the initial "guess" of $\hat{\mathrm{x}}$ is sufficiently close to the correct estimate. Therefore equation (4.14) entails, strictly speaking, an approximation of the Gaussian assumption. We point out that this is a standard omission in many inversion problems. For example, in some image restoration problems [MGK95], a careful experimentation with Toeplitz systems exhibited little or no improvement in performance after the log term was included, at substantial computational cost. Similar behaviour was observed during our experimentation. Consequently, we shall henceforth drop this term from discussion.

The data-dependent covariance $\mathcal{E}((\triangle E\mathrm{x})(\triangle E\mathrm{x})^H)$ is an $L \times L$ block matrix $\left[(\triangle E_l\mathrm{x})(\triangle E_{l'}\mathrm{x})^H\right]_{l,l' \in \{1,\ldots,L\}}$ with the (l,l')-th block $(\triangle E_l\mathrm{x})(\triangle E_{l'}\mathrm{x})^H$ is given by $D_{N/R\times M}^H \downarrow_R D_{N\times M} diag(\mathrm{x}) \mathcal{E}(\triangle \mathrm{s}_l \triangle \mathrm{s}_{l'}^H) diag(\mathrm{x}) D_{N\times M}^H \downarrow_R^H D_{N/R\times M}$. This follows from:

$$\begin{aligned} \triangle E_l \mathrm{x} &= D^H_{N/R\times M} \downarrow_R D_{N\times M} diag(\triangle \mathrm{s}_l)\mathrm{x} \\ &= D^H_{N/R\times M} \downarrow_R D_{N\times M} diag(\mathrm{x})\triangle \mathrm{s}_l. \end{aligned}$$

Due to our noise model, $\mathcal{E}(\triangle \mathrm{s}_l \triangle \mathrm{s}_{l'}^H) = \sigma_{n^s}^2 \delta_{l,l'} I$. It follows therefore that

$$R_{\mathrm{g|x}} = \sigma_n^2 \left(I + \beta^2 \begin{bmatrix} A(\mathrm{x}) & & \\ & \ddots & \\ & & A(\mathrm{x}) \end{bmatrix} \right), \tag{4.16}$$

where $A(\mathrm{x}) = D^H_{N/R\times M} \downarrow_R D_{N\times M} diag(|\mathrm{x}|^2) D^H_{N\times M} \downarrow^H_R D_{N/R\times M}$, and $\beta = \sigma_{n^s}/\sigma_n$.

Finally, we have

$$R^{-1}_{\mathrm{g|x}} = \frac{1}{\sigma_n^2} \begin{bmatrix} B(\mathrm{x})^{-1} & & \\ & \ddots & \\ & & B(\mathrm{x})^{-1} \end{bmatrix}, \tag{4.17}$$

where $B(\mathrm{x}) = I + \beta^2 D^H_{N/R\times M} \downarrow_R D_{N\times M} diag(|\mathrm{x}|^2) D^H_{N\times M} \downarrow^H_R D_{N/R\times M}$. Due to the block-diagonality, we can write the maximum likelihood estimate as

$$\hat{\mathrm{x}} = \arg\min_{\mathrm{x}} \sum_l (\mathrm{y}_l - E_l \mathrm{x})^H B(\mathrm{x})^{-1} (\mathrm{y}_l - E_l \mathrm{x}). \tag{4.18}$$

In summary, the TL-SENSE algorithm computes the maximum likelihood estimate given by equation (4.18). Minimizing this expression is numerically expensive in general. We discuss strategies for doing this in the next section, both for arbitrary sampling as well as Cartesian sampling.

4.3.2 Minimization Algorithms

Solving equation (4.18) requires solving a non-quadratic minimization problem. As a general rule, this would require a large number of cost function evaluations,

over a solution space of extremely large dimensionality. We now describe an efficient strategy for the arbitrary sampling case. We will also show that in the case of Cartesian sampled data, (4.18) can be reduced drastically in complexity, and propose an efficient algorithm.

Each function evaluation of (4.18) for general, arbitrarily sampled data involves the inversion of $NM \times NM$ matrices. Direct inversion is not a good option since these matrices are unlikely to be sparse for arbitrary sampling schemes. However, these inversions may be efficiently performed iteratively, since the products $B\mathrm{x}$ and $B^H\mathrm{x}$ can be computed at $\mathcal{O}(NM\log(N))$ cost due to the presence of the Fourier operator. Furthermore, B is obviously well-conditioned, which means that a fast iterative algorithm like Preconditioned CG [GL96] can perform this inversion in relatively few steps. Since the cost function may be expressed as a data-dependent weighted least squares problem, powerful non-linear least squares algorithms may be used to solve the problem efficiently (see [PTVF92, Ch. 10]). The TL-SENSE solution (4.18) not only reduces drastically in complexity, but is only moderately more expensive than the standard SENSE algorithm. We now turn to the special but important case of Cartesian sampling, and obtain an efficent algorithm.

In order to minimize equation (4.18) under Cartesian sampling, we can apply equation 4.8 with $B(\mathrm{x}^{(i)}) = diag(1+\beta^2\sum_{r=1}^{R}|\mathrm{x}_r^{(i)}|^2)$. This being diagonal, the ML problem reduces, like standard SENSE, to NM/R subproblems, each with only R variables. In this section, we describe our non-linear least squares (NLLS) method with Newton iterations.

From the above and the matrix structure of figure 4.1, the cost minimization can be performed independently over aliasing elements in image space. Figure 4.3 shows the algorithm to minimize (4.8), one column at a time.

- Y_l = coil output of lth coil, in spatial domain
- S_l = sensitivity map of lth coil
- X = desired MR image of size $(N \times M)$
- L = number of coils
- R = downsampling factor.
- $for\ i = 1 \ldots M$
  1. Define x,y_l,s_l as the ith column of X,Y_l,S_l, respectively.
  2. $for\ k = 1 \ldots N/R$
     (a) Define $\zeta = [\Psi_{l,r}],\ (l,r) \in [1,L] \times [1,R]$, with $\Psi_{l,r} = s_{l,(r-1)N/R+k}$.
     Let $\mu = [\mathrm{y}_{1,k}, \ldots \mathrm{y}_{L,k}]^T$.
     (b) Solve $\hat{\eta} = \arg\min_\eta (\frac{1}{1+\beta^2||\eta||^2})||\mu - \Psi\eta||^2$
     (c) $\hat{x}_{(r-1)N/R+k} = \eta_r$
  3. ith column of $X = \hat{x}$.

Figure 4.3: TL-SENSE algorithm for Cartesian sampling

The minimization in figure 4.3 is challenging due to the presence of the non-quadratic term. But the non-quadraticity enters the equation only via a well-behaved, smooth, slowly-varying function of the norm $||\eta||^2$. Consequently, we can perform the minimization using a non-linear least-squares method to solve

$$\hat{\eta} = \arg\min_{\eta} ||F(\eta)||^2, \;\; F(\eta) = q(\eta)(\mu - \Psi\eta), \;\; q(\eta) = 1/\sqrt{1 + \beta^2||\eta||^2}. \qquad (4.19)$$

This is similar to the standard least squares method for solving the pseudoinverse $\Psi^\dagger$. The only difference is that the Jacobian of F is not a constant matrix any more. Fortunately, the Jacobian in this case is readily available and easily computed. It is easily shown that

$$J(\eta) = \frac{\partial F(\eta)}{\partial \eta} = -q(\eta) \cdot (\Psi + \beta^2 q^2(\eta)(\mu - \Psi\eta)\eta^T). \qquad (4.20)$$

The additional cost of non-quadratic minimization is not significantly higher than the function evaluation used in standard pseudoinverse computed through conjugate gradients, due to the easy availability of the Jacobian and its cheap evaluation from (4.20). The algorithm in figure 4.3 was implemented in MATLAB version R13. Typical execution times for reconstructions of size 256 x 256 were between three to four times the execution time in Matlab of standard SENSE.

4.4 Results

4.4.1 Simulation results

Cartesian TL-SENSE results were obtained from the following simulation: Sensitivity maps of circular coils positioned uniformly around the FOV are computed from the Biot-Savart Law. Coil output from each coil is computed by encoding a Nyquist-sampled full MR image with the coil sensitivity map, followed by down

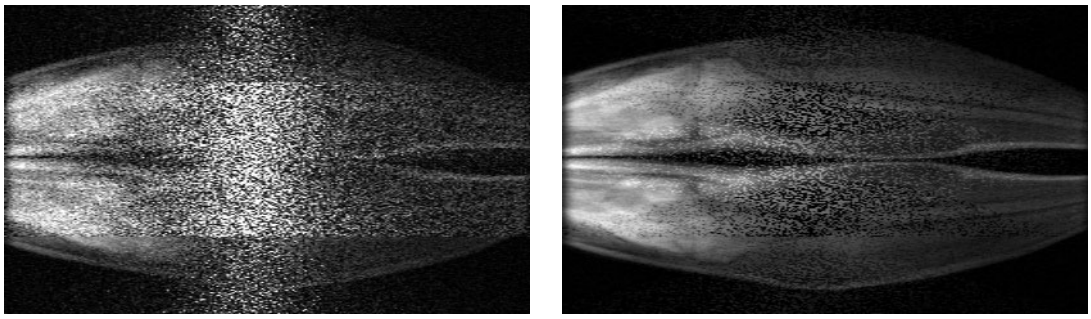

(a) (b)

Figure 4.4: (a) Standard SENSE, and (b) TL-SENSE, with $R = 4$, $L = 5$ and input SNR of 45 dB

sampling by the factor R in the phase encoding direction. Gaussian noise is added to the coil outputs as well as to the sensitivity maps, to simulate the effect of observation error and sensitivity error, respectively. MR data used in these experiments were taken from scans of patients' limbs. To keep our discussion of comparative performance uncluttered, we have introduced an equal amount of noise (in SNR terms) in both sensitivity as well as the coil outputs.

The performance of our TL-SENSE algorithm can be evaluated visually in figure 4.4. In the figure we show a noisy scenario, with SNR of 45 dB in both coil outputs and sensitivity maps, $R = 3$, and $L = 4$. The standard SENSE result can be seen to be almost useless in this case. The encoding matrix is marginally well-conditioned since only five coils were used to achieve four times acceleration. This makes the pseudoinverse quite susceptible to noise in the system, as is obvious from the SENSE result. In contrast our TL-SENSE algorithm is able to salvage considerably more useful data out of the same coil outputs, since it is much more robust to noise in the sensitivity maps.

For quantitative comparisons we have chosen the SNR metric to evaluate simu-

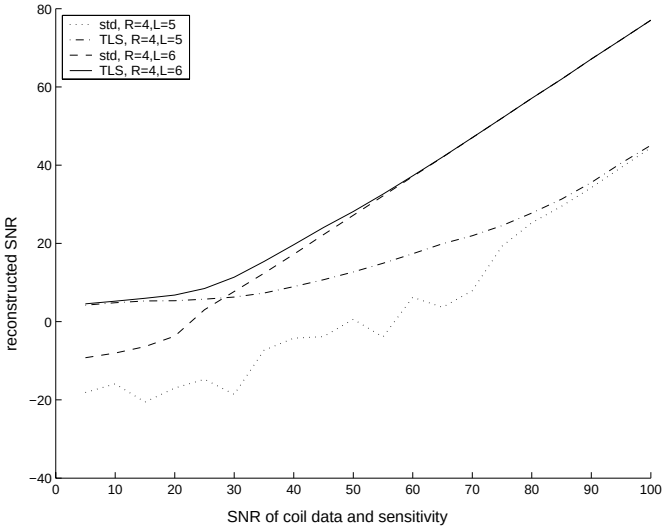

Figure 4.5: The SNR performance of standard and TL-SENSE

lation results. For a given SNR (named "input SNR") of coil outputs and sensitivity maps (assumed equal for current purposes), we determine the SNR of results obtained by both standard and TL-SENSE (named "reconstructed SNR"). The latter SNR was obtained from the difference between original full Nyquist-sampled MR image and results computed from the above mentioned simulation. Figure 4.5 shows a plot of our simulation results for the same image as above, with the k-space downsampling of $R = 4$. Two sets of plots are shown - one with $L = 5$, and the other with $L = 6$. In the former case there is more than 20 dB improvement in noise performance for high input noise. The latter case case provides an almost 14 dB improvement. The average SNR improvement over the entire range is also quite considerable, large initially, then going to zero for extremely low levels of input noise.

The SNR performance of the two algorithms converges for high input SNR case, as they should. We note that the reconstructed SNR is always lower than input SNR due to the effect of inadequate least squares averaging. Using far more

coils than strictly required for acceleration will lead to improved SNR performance overall. Already, going from $L = 5$ to $L = 6$ results in significant SNR gain. The figure also shown an interesting but expected trend - the SNR gain due to TL-SENSE becomes smaller for better conditioned, more over-determined systems. This is expected because a highly over-determined, well-conditioned system should be able to overcome the effect of noise in the system model more effectively than marginally conditioned ones. The SNR improvement shown in the figure for noisy cases is quite significant, amounting to almost a hundred times reduction of the noise energy! This improvement was achieved from the same data set and for modest additional computation time (of the order of a few minutes, in MATLAB R13) as compared to standard SENSE.

4.4.2 Experiments with Sensitivity mismatch on phantom data

Phased array experiments were performed with a high-resolution (HiRes) phantom as the target, and a uniform spherical phantom to generate sensitivity maps. These experiments were mainly performed to demonstrate the use of our technique even for cases where sensitivity noise is not dominated by i.i.d. Gaussian noise, but other sources of errors like sensitivity mismatch and insufficient FOV. The HiRes phantom was placed within a plastic tube filled with doped water, and torso coil pads were wrapped around the tube. In order to acheive sufficient resolution of the target, the FOV was chosen to be smaller than the diameter of the plastic tube. This results in controlled aliasing in the reconstructed coil data. Sensitivity maps were obtained under the same conditions with the uniform phantom, but now in addition to the uniform phantom signals, we also have contributions from

the tube, which also has a uniform response. Un-aliased data received by one coil within the 4-coil configuration is shown in figure 4.6. Notice that sensitivity response has some contributions from the tube, of unequal intensity to the uniform phantom inside it. This state of affairs is usually quite disastrous for conventional parallel imaging. In addition, a small mis-alignment of the image was also observed between the sensitivity data and the HiRes data. While this experiment does not follow the standard parallel imaging set up, it mimics in many ways the kinds of errors one can expect if sensitivity maps are mis-aligned, incorrect, or obtained by improper division with a body coil image. The purpose of the experiment was to determine the extent to which such a complicated data set can be reconstructed under gross inaccuracies in sensitivity data. These errors are quite unlike the noise model we assumed in this work, and we would like to see if the technique is still effective. The reconstruction results are shown in figure 4.7. In addition to standard SENSE, we also show for comparison a Tikhonov-regularized version of SENSE. This should address the question of whether these errors can be mitigated simply by regularizing the SENSE reconstruction. It is obvious that while the standard SENSE method results in considerable errors due to mismatch and aliasing in the original data, this error can not be easily removed even by regularizing. The noise levels go down with higher regularization factors, but at the cost of degraded unfolding performance. This is an expected result - in the limit when regularization parameter is very large, the matrix inverse corresponds to a copy of the observation, i.e. no unfolding. The TL-SENSE result on the other hand is quite a lot more effective at both noise reduction as well as image unfolding. The effect of sensitivity mismatch and aliasing problems is visible, but considerably muted compared to SENSE results. The result seems to suggest that

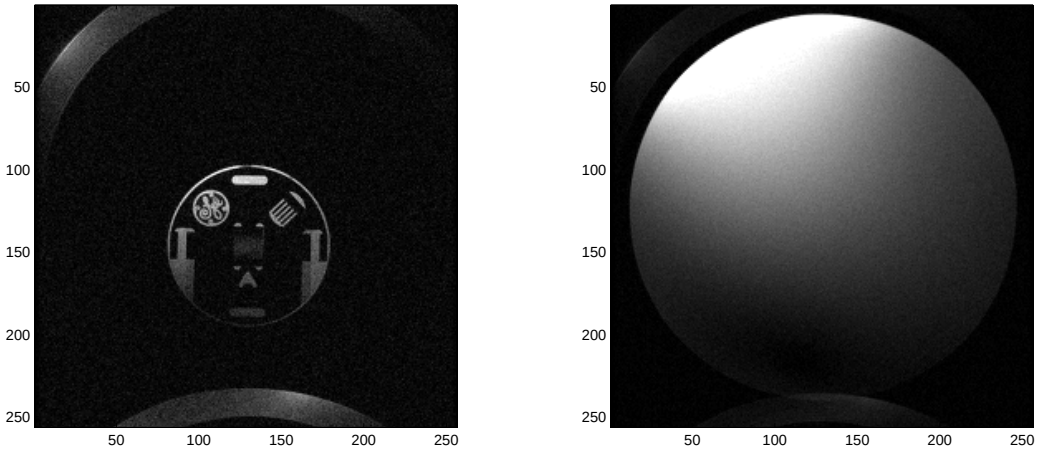

(a) (b)

Figure 4.6: Data received by a coil within a 4-coil arrangement. (a) shows the (unaliased) output of the HiRes pahntom within a PVC tube, and (b) shows sensitivity map obtained from a uniform phantom.

the TL-SENSE algorithm is effective even in cases where the assumed sensitivity noise model is inapplicable.

4.4.3 In vivo imaging with a 4-element torso coil array

Several experiments using phased array coils were performed on human subjects. Two torso coil pads, each with two coils, were used, one placed above and one below the torso. Data from each coil was independently stored using all four channels available on the MR scanner. The Total Least Sense algorithm was applied to the entire data set, using the sensitivity maps obtained during a pre-scan with a uniform ball phantom. The experiments were set up so that the phantom covered the entire extent of the torso region imaged in the subsequent scan. In cases where the phantom fell slightly short of the torso in extent, we extrapolated sensitivity

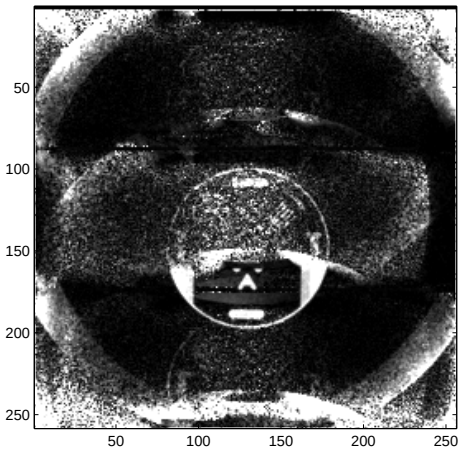

(a)

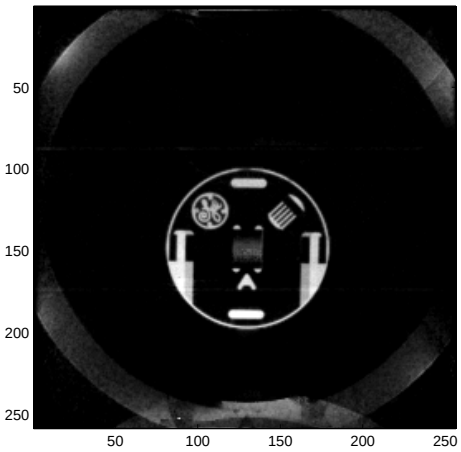

(b)

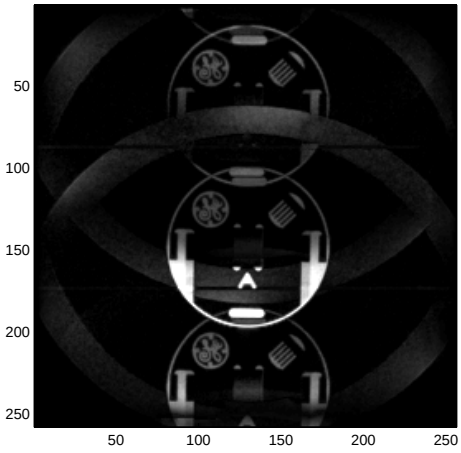

(c)

Figure 4.7: Reconstruction results of HiRes data in figure 4.6, with $R = 3$, $L = 4$: (a) Standard SENSE, (b) TL-SENSE, and (c) Standard SENSE with regularization

data as required. The following method was employed to extrapolate sensitivity data. First we obtain a binary image (silhouette) of the phantom from a sum-of-squares combined image from all four coils. The binary image was obtained by intensity thresholding, followed by some morphological processing to clean up the binary image. Using the data contained within the silhouette, we fit a two-dimensional low-order polynomial so that the square error within the silhouette is minimized. We note that this procedure is unreliable for large extrapolation factors, and was used only sparingly and only for small amounts of mismatch.

Torso images were obtained with the following MR parameters. A Fast Gradient Echo Sequence with a flip angle of 60 degrees and TE/TR of 3.3/7.5 was used. Cardiac gating breath hold techniques was used for scans involving the heart region, with 8 views acquired per heartbeat. The bandwidth was 31.2 kHz, and the axial slice thickness was 5 mm. Pre-scans with phantom were acquired similarly, but with TE/TR 3.3/15, and flip angle of 30 degrees. Phantom scans were performed with full Nyquist k-space resolution of 256 x 256 data points. Torso scans were acquired with varying number of views, depending on the under-sampling ratio, each view with 256 data points. Rows (views) in k-space were sub-sampled by two and three by skipping, respectively, one and two rows for each sampled row. This yielded acceleration factors of two and three, respectively. Acceleration by four is theoretically possible with four coils, but the resulting least squares problem becomes so ill-posed as to be virtually unusable.

Figure (4.9) depicts a reconstruction of the torso showing details of the stomach region. The k-space was sub-sampled by three, and four phased array coils as described above were used in the reconstruction. Standard SENSE reconstruction is shown in (a), and our TL-SENSE reconstruction in (b). This particular case

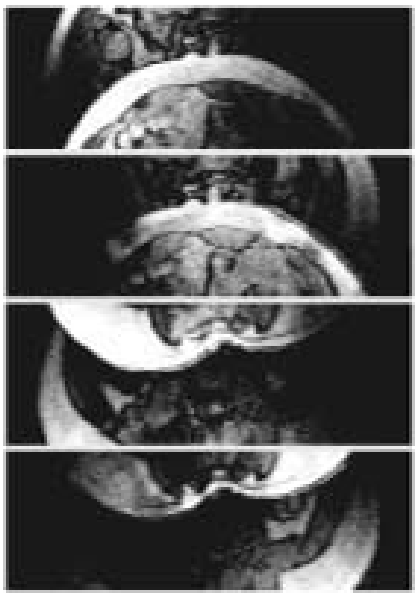

Figure 4.8: Aliased coil data from a torso scan with $R = 3$, $L = 4$

possessed reasonably good conditioning properties, and the reconstruction was well-posed for both standard and TL-SENSE solutions. The data suffered from random instrumentation noise as well as some amounts of i.i.d. sensitivity noise, resulting in unwanted noise amplification during standard reconstruction. The TL-SENSE reconstruction in contrast does not exhibit this noise amplification to any significant extent.

Figure (4.10) depicts the same torso slice as above, but this time with some mismatch in measured and actual sensitivity maps. The mismatch was a result of using flexible torso pads without rigid fastenings - a common issue with torso coils. The k-space was sub-sampled by three, and four phased-array coils as described above were used in the reconstruction. Conditioning of the encoding matrix was again reasonably good, and the reconstruction was well-posed. However, the data suffered from some instrumentation noise apart from sensitivity mismatch, resulting in unwanted noise amplification artifacts during standard reconstruction.

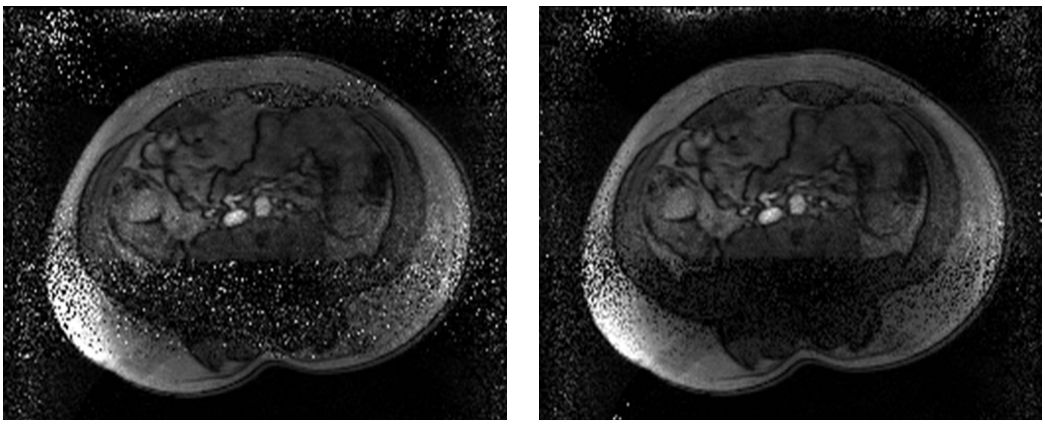

(a) (b)

Figure 4.9: Reconstruction results of torso data from figure 4.8: (a) Standard SENSE, and (b) TL-SENSE, with $R = 3$, $L = 4$

The TL-SENSE reconstruction however does not suffer from these reconstruction artifacts.

4.4.4 Parallel Brain Imaging With An 8-Element Head Coil

For our next experiment, we scanned some brain data using an eight-element head coil, one channel per element. The acceleration factor was $R = 4$. Figure 4.12 shows the results. The standard SENSE reconstruction, shown in (a), leads to too much noise amplification. In order to demonstrate that this problem cannot really be addressed by simply performing regularization on the SENSE method, we show in (b) the output of a Tikhonov-regularized SENSE algorithm, with the regularization factor set at 0.1, chosen after several trials with other values. While this procedure is considerably less noise-prone, it has in fact failed to resolve the aliasing components properly. A smaller value of regularization, say 0.05, would

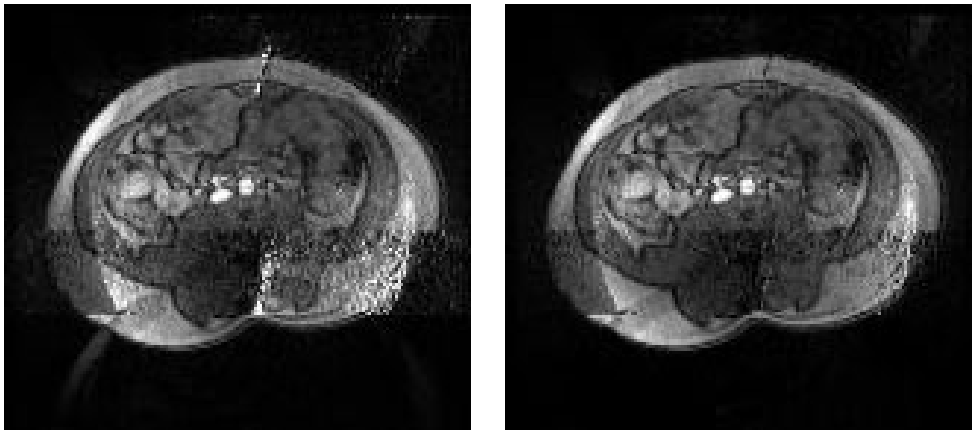

(a) (b)

Figure 4.10: Reconstruction results of torso scan : (a) Standard SENSE, and (b) TL-SENSE, with $R = 3$, $L = 4$

have resolved the ghosting problem better, but would have caused more noise amplification. In either scenario, the result is mostly unusable. Figure 4.12(c) shows the TL-SENSE reconstruction, which seems to suffer neither from excessive noise amplification, nor from ghosting. This example illustrates the efficacy of our total least squares approach, compared to a regularized least squares approach previously suggested by several authors [LBJ+02].

4.5 Conclusions

A natural extension to our work would be to handle non-Cartesian sampling schemes. The basic solution for the maximum likelihood estimate (4.18) remains the same, but non-Cartesian sampling methods do not lend themselves to such drastic reduction in problem size. The minimization must now be performed over the full image space without the benefit of diagonalization that was exploited for Cartesian sampling. We note that, again, the non-quadratic term $B(\mathrm{x})$ in

Figure 4.11: Aliased coil data from a head scan with $R = 4$, $L = 8$

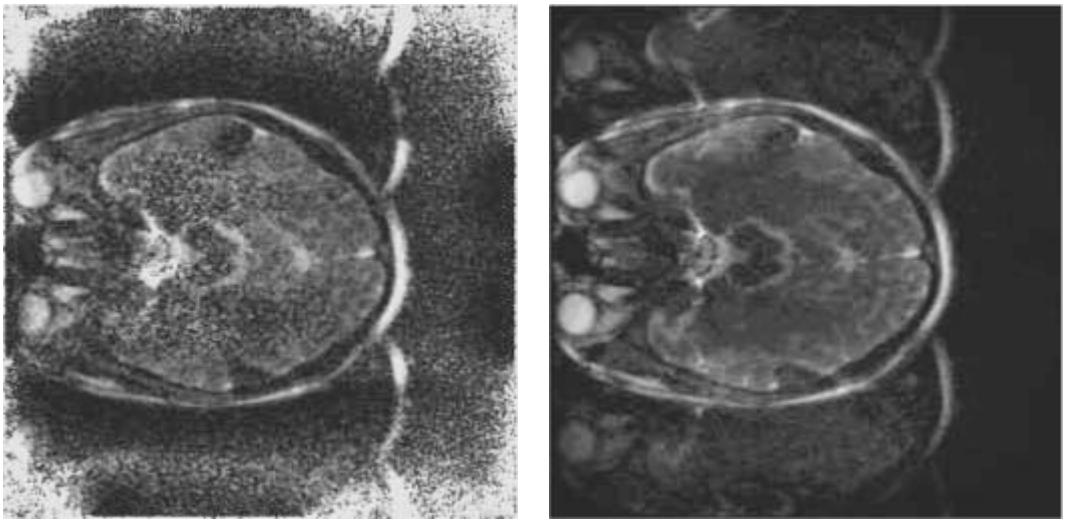

(a)

(b)

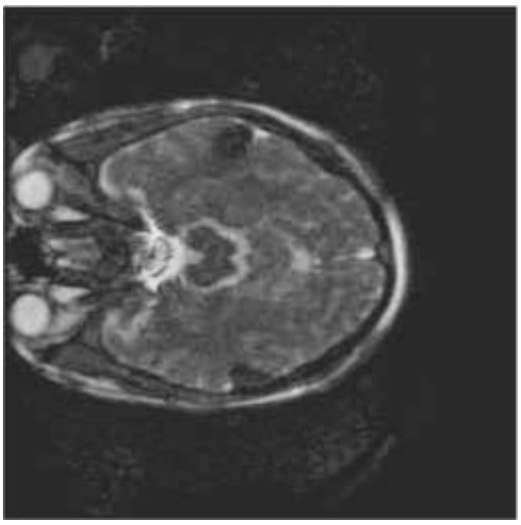

(c)

Figure 4.12: Reconstruction results of head scan data in figure 4.11: (a) Standard SENSE, (b) Standard SENSE with regularization, and (c) TL-SENSE, with $R = 4$, $L = 8$

(4.18) is rather well-behaved compared to the quadratic cost term. Hence, we may again utilize non-linear least squares techniques using Newton-type direction search to compute the minimum. The evaluation of the Jacobian and Hessian is again expected to be cheap due to its block-diagonal nature. For arbitrary sampling schemes therefore we expect our algorithm to be of the same order of complexity as standard SENSE algorithms.

We have addressed the problem of obtaining an optimal solution to the parallel imaging reconstruction problem in the presence of both measurement and sensitivity noise. We have shown that for i.i.d. Gaussian noise the optimal solution is the minimizer of a weakly non-quadratic objective function which may be solved efficiently via a non-linear least squares iterative technique with modest additional complexity compared to standard SENSE algorithms. We have also derived simplified expressions for the cost function as well as the Jacobian of the associated least squares problem in the case of Cartesian k-space sampling. A fast Newton algorithm with explicit Jacobian information was developed to solve the problem. Results for Cartesian k-space sampling indicate impressive improvement in performance compared to standard SENSE, amounting to almost 20 dB SNR gain in several high-noise cases. The algorithm yields substantial improvement even in cases where the i.i.d. Gaussian sensitivity noise model implicit in the method is not accurate.

Chapter 5

A Graph Cut Energy Minimization Algorithm for a New Class of Pixel Labeling Problems

5.1 Introduction

A large number of Bayesian estimation problems that arise in medical imaging, signal and image processing and machine vision can benefit immensely from a Markov Random Field (MRF) based formulation of *a priori* information. It is well-known that the MRF approach is a powerful and natural way to exploit spatial redundancy present in multi-dimensional data. These problems typically require inverting a linear system. The MRF approach has found favour in some recent work in image restoration as well as vision problems like stereo. In this chapter we propose the use of this approach for enhanced MR reconstruction from parallel data - in other words exploit both receiver redundancy from multiple coils as well as spatial redundancy in the form of a spatial prior. It turns out that the same class of techniques can perform Bayesian estimation in a large number of linear systems, essentially any problem which involves the estimation of multi-dimensional spatially correlated signals. Hence we will formulate the problem in terms of general linear systems, develop our technique in general terms, and then

specialize to particular applications. The main restriction of our technique is that it works only on linear systems with non-negative matrix elements. We will show that Cartesian parallel MR reconstruction problems fall under this category, as do many other problems in vision and image processing. We will motivate our approach by discussing linear systems arising in Vision; then we will extend the discussion to MR reconstruction.

All these linear problems can be made well-posed by adding a regularization term; this term imposes spatial smoothness, and should preserve discontinuities. The resulting energy minimization problem is quite challenging, and good algorithms only exist for restricted cases. If the system matrix is diagonal, as occurs in image denoising, the energy function can be solved by techniques such as graph cuts. Such algorithms have proven to be very effective for pixel labeling problems; for example, the majority of the top-ranked stereo algorithms on the Middlebury benchmarks use graph cuts for energy minimization. This chapter shows how to use graph cuts to obtain a discontinuity-preserving solution when the system matrix is no longer diagonal, but instead is an arbitrary non-negative matrix. In such problems, the data cost for a pixel to have a label depends on the hypothesized labels of other nearby pixels, and so existing graph cut methods cannot be applied to minimize the energy. We use a dynamically chosen approximation to the energy which can be minimized by graph cuts, and show that minimizing this approximation also decreases the original energy. We demonstrate our method by applying it for image deconvolution and motion deblurring on real images, and achieve promising peak SNR. We also demonstrate our method on parallel MR reconstruction from raw Fourier data.

5.1.1 Chapter Overview

We begin with a discussion of general linear inversion problem arising in vision, in §5.2. The section also contains a formal description of the graph cut problem for linear systems. Section 5.3 contains a brief survey of related work in machine vision and image processing literature. In section 5.4 we give some technical details of graph cuts, and show that existing methods cannot minimize the energy function corresponding to MRF-based Bayesian estimation of arbitrary non-diagonal linear systems. In section 5.5 we show that a dynamically chosen approximation to the energy function can be minimized with graph cuts, and that minimizing the approximation also decreases the original energy. Section 5.6 demonstrates experimental results for deconvolution and motion deblurring, and shows that our methods increase peak SNR (PSNR). In section 5.7 we extend the graph cut method to MR reconstruction from parallel data. Preliminary results are contained in §5.8. In §5.9 we discuss some extensions of this work.

5.2 Linear Inverse Problems in Machine Vision

Many pixel labeling problems in computer vision can be viewed as inverse problems [BB98] where the observed data y is linearly related to the desired quantity x by

$$y = Hx + n. \tag{5.1}$$

Here, H is the system matrix and n is a noise vector. In image denoising, for example, y and x are intensities and H is the identity matrix. Inverse problems of this form are ill-posed, and are typically solved by minimizing a regularized energy function [PTK85]. The energy of a solution x is given by

$$||y - Hx||_2^2 + G(x), \tag{5.2}$$

which is the sum of a data term and a smoothness term. The data term forces x to be compatible with the observed data, and the smoothness term $G(x)$ penalizes solutions that lack smoothness. This approach can be justified on statistical grounds, since minimizing equation (5.2) is equivalent to maximum *a posteriori* estimation [PTK85] assuming Gaussian noise. The energy is proportional to the negative logarithm of the posterior: the data term comes from the likelihood, and the smoothness term comes from the prior.

A wide variety of algorithms have been developed to minimize equation (5.2) when G imposes global smoothness [PTVF92]. However, global smoothness is inappropriate for most vision problems, since most underlying quantities change slowly across most of the image, but have discontinuities at object boundaries. As a result, some form of discontinuity-preserving G is required, which makes the energy minimization problem much harder.

A natural class of discontinuity-preserving terms is

$$G_{MRF}(x) = \sum_{(p,q)\in\mathcal{N}} V(x_p, x_q). \tag{5.3}$$

The neighborhood system $\mathcal{N}$ consists of pairs of adjacent pixels, usually the 4-connected neighbors. The smoothness cost $V(l, l')$ gives the cost to assign l and l' to neighboring pixels. Typically the smoothness cost has a discontinuity-preserving form such as $V(l, l') = \min(|l - l'|, K)$ for some metric $|\cdot|$ and constant K. Such a smoothness term incorporates discontinuity-preserving priors, which can be justified in terms of Markov Random Fields [Li95].

5.2.1 Problem definition

The problem we address is to efficiently minimize

$$\mathcal{E}(x) = ||y - Hx||_2^2 + G_{MRF}(x). \tag{5.4}$$

When H is diagonal, as in image denoising, the data term has a restricted form that makes it computationally tractable to minimize $\mathcal{E}$. Specifically,

$$||y - Hx||_2^2 = \sum_p (y_p - H_{p,p}x_p)^2, \tag{5.5}$$

which means that the data cost for the pixel p to have the hypothesized label (i.e., intensity) x_p only depends on x_p and y_p. With such an H, the energy $\mathcal{E}$ can be efficiently minimized by graph cuts, which have proven to be very effective for pixel labeling problems such as stereo [SS02].

Graph cuts, however, can only be applied to certain energy functions [KZ04]. We will demonstrate in section 5.4 that existing graph cut energy minimization methods cannot be applied when H is non-diagonal. Intuitively, this is because the data cost for a pixel to have a label depends on the hypothesized labels of other nearby pixels. Many important problems involve a non-diagonal system matrix whose elements are zero or positive. Examples include deconvolution, motion deblurring and the reconstruction of MRI images from raw Fourier data.

5.3 Related Work

There are many optimization techniques to solve equation (5.2) when G imposes global smoothness; examples include Preconditioned Conjugate Gradient, Krylov-space methods, and Gauss-Siedel [GL96]. Unfortunately, these convex optimization methods cannot be applied when the smoothness term is of the discontinuity-preserving form given by G_{MRF}. This is not surprising, since the most of these

methods use some variant of local descent, while pixel labeling problems with discontinuity-preserving smoothness terms are NP-hard [BVZ01].

Convex optimization techniques can be generalized to handle certain MRF-based smoothness terms under restricted assumptions. [FL97] presents a compound Gaussian MRF model for image restoration. They introduce additional parameters describing edge discontinuities into the MRF prior model, but the underlying image is assumed to have a Gaussian distribution enabling the use of Tikhonov-regularized inversion. [BS93] considers generalized Gaussian MRF models, which handle the (highly restricted) class of non-convex priors which can be turned into Gaussian priors by a non-linear transformation of image intensities. These approaches, while interesting, cannot be generalized to discontinuity-preserving smoothness terms like G_{MRF}.

It is also possible that an energy function like ours could be minimized by a fast algorithm that is not based on graph cuts, such as loopy belief propagation (LBP) [Pea88]. LBP is a method for inference on graphical models, which has been reported to produce results that are comparable to graph cuts [TF03]. It is not clear whether or not LBP could be used for the energy function we examine, as it is in a different form than the ones where LBP has been applied (such as [TF03]). In addition, LBP is not guaranteed to converge on problems that arise in early vision, due to the highly loopy structure of the neighborhood system. In contrast, graph cut energy minimization algorithms have well-understood convergence properties, and (as we will demonstrate) can be modified to minimize our energy function.

A related problem is addressed in [TRF04] using LBP. They are concerned with reducing the number of potential labels that a pixel can have, in order to make graphical inference more efficient. While they do not minimize a new class of energy

functions, their technique can be used to perform deconvolution. Their method relies on learning, and uses LBP for inference, while we do not use learning and use graph cuts for energy minimization. While their use of learning is innovative, there is an advantage to our non-learning based approach, since for many applications it may be difficult to obtain a representative training set.

5.4 Graph Cuts for H

In the last few years, efficient energy minimization algorithms using graph cuts have been developed to solve pixel labeling problems [BVZ01]. These algorithms have proven to be very effective; for example, the majority of the top-ranked stereo algorithms on the Middlebury benchmarks use graph cuts for energy minimization [SS02]. The most powerful graph cut method is based upon expansion moves.[1] Given a labeling x and a label α, an α-expansion $\chi = \{ \chi_p \mid p \in \mathcal{P} \}$ is a new labeling where χ_p is either x_p or α. Intuitively, χ is constructed from x by giving some set of pixels the label α. The expansion move algorithm picks a label α, finds the lowest cost χ and moves there. The algorithm converges to a labeling where there is no α-expansion that reduces the energy for any α.

The key step in the expansion move algorithm is to compute the α-expansion χ that minimizes the energy $\mathcal{E}$. This can be viewed as a binary energy minimization problem, since during an α-expansion each pixel either keeps its old label or moves to the new label α. An α-expansion χ is equivalent to a binary labeling $b =$

[1] The other graph cut methods either have a running time that is quadratic in the number of intensities [BVZ01, Sec. 4] or are cannot handle discontinuity-preserving smoothness terms [Ish03].

$\{ b_p \mid p \in \mathcal{P} \}$ where

$$\chi_p = \begin{cases} x_p & \text{iff } b_p = 0, \\ \alpha & \text{iff } b_p = 1. \end{cases} \tag{5.6}$$

Just as for a labeling χ there is an energy $\mathcal{E}$, for a binary labeling b there is an energy B. More precisely, assuming χ is equivalent to b, we define B by

$$B(b) = \mathcal{E}(\chi).$$

We have dropped the arguments x, α for clarity, but obviously the equivalence between the α-expansion χ and the binary labeling b depends on the initial labeling x and on α. Since we will focus on problems like image restoration or denoising, we will assume labels are always intensities, and use the terms interchangeably.

In summary, the problem of computing the α-expansion that minimizes $\mathcal{E}$ is equivalent to finding the b that minimizes B. The exact form of B will depend on $\mathcal{E}$. Graph cuts can be used to find the global minimum of B, and hence the lowest cost α-expansion χ, as long as B is of the form

$$B(b) = \sum_p B_1(b_p) + \sum_{p,q} B_2(b_p, b_q). \tag{5.7}$$

Here, B_1 and B_2 are functions of binary variables; the difference is that B_1 depends on a single pixel, while B_2 depends on pairs of pixels. It is shown in [KZ04] that such a B can be minimized exactly by graph cuts as long as

$$B_2(0,0) + B_2(1,1) \leq B_2(1,0) + B_2(0,1). \tag{5.8}$$

If B_2 satisfies this condition, then B is called *regular* (there is no restriction on the form of B_1) [2].

[2] Terms *regular* and *regularity* as used in this chapter should not be confused with signal regularity in the Holder sense, nor with regularization of linear inverses

When H is diagonal the data term is given in (5.5), which only involves a single pixel at a time, while the smoothness term involves pairs of pixels. Hence B_1 comes from the data term, while B_2 comes from the smoothness term:

$$B_1(b_p) = \begin{cases} (y_p - H_{p,p}x_p)^2 & \text{if } b_p = 0, \\ (y_p - H_{p,p}\alpha)^2 & \text{if } b_p = 1, \end{cases} \tag{5.9}$$

while

$$B_2(b_p, b_q) = V(\chi_p, \chi_q). \tag{5.10}$$

(Recall that the equivalence between χ and b is given by equation (5.6)). It is shown in [KZ04] that if V is a metric B_2 satisfies equation (5.8). As a result B is regular, and so the expansion move algorithm can be applied. Fortunately, many discontinuity-preserving choices of V are metrics (see [BVZ01] for details).

However, the situation is very different when H is non-diagonal. Consider the correlation matrix of H defined by $R_H(p,q) = \sum_{r=1}^{N} H_{r,p}H_{r,q}$. We can then write

$$\begin{aligned} ||y - Hx||_2^2 = \sum_p y_p^2 - 2\sum_p (\sum_q y_q H_{q,p}) x_p + \\ \sum_p R_H^2(p,p)x_p^2 + \sum_{(p,q)} R_H(p,q)x_p x_q. \end{aligned} \tag{5.11}$$

The first three terms in (5.11) depend only on a single pixel while the last term depends on two pixels at once. As a result, when H is non-diagonal the second term in (5.7) is

$$\sum_{(p,q)} 2R_H(p,q)\chi_p\chi_q + \sum_{(p,q)\in\mathcal{N}} V(\chi_p, \chi_q). \tag{5.12}$$

Theorem 5.1 *When H is non-diagonal, the binary cost function $B(b)$ is not regular.*

PROOF: The regularity condition is that for any α and pixel pair (p,q)

$$R_H(p,q)(\alpha^2 + x_p x_q - \alpha x_p - \alpha x_q) \leq 0. \tag{5.13}$$

R_H is non-negative by construction, and the polynomial in α factors into $(\alpha - x_p)(\alpha - x_q)$. So equation (5.13) holds iff

$$x_p \leq \alpha \leq x_q. \tag{5.14}$$

This is clearly invalid for arbitrary x_p, x_q and α. Thus, the optimal α-expansion can only be computed on those pixels $\{\, p \mid \forall q \; x_p \leq \alpha \leq x_q \,\}$. This is a small subset of the image.

5.5 Approximating the Energy

We now demonstrate how to use the graph cuts to minimize our energy function for arbitrary non-negative H. Our approach is to minimize a carefully chosen approximation to the original energy $\mathcal{E}$. The approximation is chosen dynamically (i.e., it depends upon x and α), and the α-expansion that most decreases the approximation can be rapidly computed using graph cuts. While we cannot guarantee that we find the best α-expansion for the original energy function $\mathcal{E}$, we can show that decreasing our approximation also decreases $\mathcal{E}$.

As before, we will use the expansion move algorithm with a binary energy function B. We will assume that V is a discontinuity-preserving metric, which means that we can write $B(b) = B_{regular}(b) + B_{cross}(b)$, where

$$B_{cross}(b) = \sum_{(p,q)} 2R_H(p,q)\chi_p\chi_q \tag{5.15}$$

are the only terms that are not known to be regular. Graph cuts cannot be used because there will be pairs (p, q) that do not satisfy equation (5.14), and as a result B is not regular.

We will create a regular approximation B' and minimize it instead of B. The construction proceeds in two steps; first, we introduce an initial modification $\hat{B}$,

and then we use $\hat{B}$ to build B'. Let $\mathcal{R}$ denote the set of pairs (p, q) that obey equation (5.14) at the current labeling x, i.e.

$$\mathcal{R} = \{\, (p, q) \mid x_p \leq \alpha \leq x_q \,\}.$$

For convenience, we will also define $\bar{\mathcal{R}} = \mathcal{N} \setminus \mathcal{R}$, which is the intersection of $\mathcal{N}$ and the complement of $\mathcal{R}$. We can split the pairs of pixels (p, q) into those in $\mathcal{R}$ and those in $\bar{\mathcal{R}}$. We will use an approximation for those pixels in $\bar{\mathcal{R}}$.

We begin by approximating B_{cross} by

$$\begin{aligned} \hat{B}_{cross}(b) = & \sum_{(p,q) \in \mathcal{R}} 2R_H(p, q)\chi_p\chi_q \\ + & \sum_{(p,q) \in \bar{\mathcal{R}}} R_H(p, q)(x_p\chi_q + \chi_p x_q) \end{aligned} \tag{5.16}$$

Our initial approximation is $\hat{B}(b) = B_{regular}(b) + \hat{B}_{cross}(b)$. It is straightforward to show that we can use graph cuts with this approximation.

Theorem 5.2 *The energy function $\hat{B}(b)$ is regular.*

PROOF: Except for the last term in equation (5.16), all the terms in $\hat{B}(b)$ either involve a single pixel or are known to satisfy equation (5.8). Since $R_H(p, q)$ is non-negative, we can simply focus on $(x_p\chi_q + \chi_p x_q)$. As a result, $\hat{B}(b)$ is regular if

$$\begin{aligned} (x_p x_q + x_p x_q) + (x_p\alpha + \alpha x_q) \quad \leq \\ (x_p x_q + \alpha x_q) + (x_p\alpha + x_p x_q). \end{aligned}$$

The two sides above are equal.

The obvious question is whether decreasing our modified energy function $\hat{B}$ results in a decrease in the original energy function B. Consider an initial labeling

x and an α-expansion χ. Both χ and the input labeling x correspond to binary labelings; χ corresponds to b, and x corresponds to the zero vector, which we will write as $\mathbf{0}$. The change in energy when we move from x to χ under the two different energy functions can be written as

$$\Delta B = B(b) - B(\mathbf{0}), \qquad \Delta \hat{B} = \hat{B}(b) - \hat{B}(\mathbf{0}). \tag{5.17}$$

We can use graph cuts to find the b that minimizes $\hat{B}$, so $\Delta \hat{B} < 0$. We wish to show that this results in a decrease in the original energy function, i.e. $\Delta B < 0$.

Using the definitions of $B, \hat{B}$ we can write

$$\Delta \hat{B} = \Delta B + \sum_{(p,q) \in \bar{\mathcal{R}}} R_H(p,q) \Delta(\chi_p, \chi_q). \tag{5.18}$$

The function $\Delta(\chi_p, \chi_q)$ is defined by

$$\Delta(\chi_p, \chi_q) = \begin{cases} 0 & \chi_p = x_p, \chi_q = x_q, \\ x_q(x_p - \alpha) & \chi_p = \alpha, \chi_q = x_q, \\ x_p(x_q - \alpha) & \chi_p = x_p, \chi_q = \alpha, \\ 2\alpha(\frac{x_p + x_q}{2} - \alpha) & \chi_p = \chi_q = \alpha. \end{cases} \tag{5.19}$$

In order to reduce the value of the original energy function, we need $\Delta B \leq 0$. It suffices to show that the second term in equation (5.18) is positive.

Let us define the set of pixel pairs

$$\mathcal{R}' = \big\{ (p,q) \in \bar{\mathcal{R}} \mid x_p < \alpha, x_q < \alpha \big\},$$

and the set of pixels

$$\mathcal{C} = \{ p \mid \exists q \text{ s.t. } (p,q) \in \mathcal{R}' \}. \tag{5.20}$$

$\mathcal{C}$ is important because if we do not modify pixels in $\mathcal{C}$, then reducing our modified energy reduces the original energy.

Theorem 5.3 *Let x be an initial labeling and consider the α-expansion χ corresponding to the binary labeling b. Suppose that b does not modify the label of any pixel in $\mathcal{C}$. Then if b decreases our modified energy (i.e., $\Delta\hat{B} < 0$), it also decreases the original energy (i.e., $\mathcal{E}(\chi) < \mathcal{E}(\S)$.*

PROOF: If $p \notin \mathcal{C}$, then for some neighbor q at least one of x_p, x_q is greater than α. If both $x_p > \alpha$ and $x_q > \alpha$, then $\Delta(\chi_p, \chi_q) \geq 0$, since all of the cases in equation (5.19) are non-negative. If α lies between x_p, x_q then $(p, q) \in \mathcal{R}$.

We will need a better approximation than $\hat{B}$, since minimizing $\hat{B}$ is sound, but not practical. In practice, $\mathcal{C}$ will be too large for fast convergence, since pixels in $\mathcal{C}$ do not change. We will further modify the energy to allow all pixels to potentially change, hence increasing the convergence speed. Our final approximation is

$$B'(b) = \hat{B}(b) + \sum_{p \in \mathcal{C}} \lambda b_p, \tag{5.21}$$

where λ is a constant. This imposes a cost of λ for a pixel in $\mathcal{C}$ to increase in brightness to α.

Notice that the new cost only depends on a single pixel at a time, so B' is regular and we can use graph cuts to rapidly compute its global minimum. As before, we wish to show that reducing B' reduces B.

Similarly to equation (5.18) we can write

$$\begin{aligned} \Delta B' = \Delta B + &\sum_{(p,q) \in \bar{\mathcal{R}} \setminus \mathcal{R}'} R_H(p, q) \Delta(\chi_p, \chi_q) \\ &+ \sum_{(p,q) \in \mathcal{R}'} R_H(p, q) \Delta'(\chi_p, \chi_q). \end{aligned} \tag{5.22}$$

Here,

$$\Delta'(\chi_p, \chi_q) = \begin{cases} 0 & \chi_p = x_p, \chi_q = x_q, \\ x_q(x_p - \alpha) + \lambda' & \chi_p = \alpha, \chi_q = x_q, \\ x_p(x_q - \alpha) + \lambda' & \chi_p = x_p, \chi_q = \alpha, \\ 2\alpha(\frac{x_p + x_q}{2} - \alpha) + 2\lambda' & \chi_p = \chi_q = \alpha, \end{cases} \tag{5.23}$$

where $\lambda' = \lambda / R_H(p, q)$.

Set $\lambda_0 = \sum_{(p,q)\in\mathcal{R}'} R_H(p, q)\alpha^2$. If $\lambda > \lambda_0$, we can show that reducing our modified energy also reduces the original energy.

Theorem 5.4 *Let x be an initial labeling and consider the α-expansion χ corresponding to the binary labeling b. Then if b decreases our modified energy (i.e., $\Delta B' < 0$), it also decreases the original energy (i.e., $\mathcal{E}(\chi) < \mathcal{E}(\S)$.*

PROOF:

Note that the second term in equation (5.22) is positive due to Theorem 5.3. We will show that the third term can also be made positive by ensuring each case of $\Delta'(\chi_p, \chi_q)$ has positive energy. The case $\chi_p = \chi_q = \alpha$ is positive if $\lambda > R_H(p, p)\alpha^2,\ \forall p \in \mathcal{P}$. The second case becomes

$$\begin{gathered} \sum_{(p,q)\in\mathcal{R}'} R_H(p, q)x_q(\alpha - x_p) + \lambda \geq \\ \sum_{(p,q)\in\mathcal{R}'} R_H(p, q)(x_q(\alpha - x_p) + \alpha^2) \geq \\ \sum_{(p,q)\in\mathcal{R}'} R_H(p, q)(x_q\alpha + (\alpha^2 - x_p x_q)) > 0 \end{gathered} \tag{5.24}$$

since $x_p < \alpha, x_q < \alpha$. An identical argument holds for the third case. Thus, $\Delta'(\chi_p, \chi_q) \geq 0$, and we get $\triangle B'(b) < 0 \implies \triangle B(b) < 0$.

Our algorithm, then, replaces B by the approximation B' and uses graph cuts to find the global minimum of B'. We are guaranteed that this decreases the original energy $\mathcal{E}$ which we wish to minimize.

5.5.1 Further improvements

Theorem 5.4 guarantees that the original energy goes down whenever the modified energy B' goes down, for a large enough λ. We note that even B' is highly conservative in terms of satisfying the downhill criterion, for two reasons. First, the global supremum $\lambda = \lambda_0$ is much higher than necessary for many pixels only slightly below α. Second, $\Delta'(\chi_p, \chi_q)$ does not have to be positive for all (p, q); we only require the last term in equation (5.23) to be positive. So in practice, one may use a much smaller λ than suggested by Theorem 5.4. Of course, this might result in a small number of expansion moves producing uphill moves in the original energy, but we can always evaluate the change in energy, and reject moves that increase the cost. In most of our experiments, we chose $\lambda < 0.1\lambda_0$, without resulting in more than a few uphill moves. Choosing a small λ is desirable since the modified cost then becomes closer to the original cost.

Our method has the counterintuitive property that it is not symmetric; it is more difficult for pixels to become brighter than for pixels to become darker, due to the cost introduced in equation (5.21). This would seem to make it very difficult for a dark region of the image to undergo an α-expansion, but very easy for a bright region. It is easy to fix this asymmetry for many choice of H, by simply taking the negative of the image. If we normalize the intensities to lie in the range $[0, 1]$ and define the vector $\mathbf{1}$ to be all 1's, then the condition that H is not affected by inverting the image is $(\mathbf{1} - y) = H(\mathbf{1} - x)$, or $H\mathbf{1} = H$. Such an H is called

energy preserving, since it does not change a uniformly bright image. For most applications, H is energy preserving and so this transformation can be applied to increase the set of pixels that can be modified in a single α-expansion.

5.6 Experimental results - low level vision

Our approach is valid for any non-negative H, which covers the vast majority of linear inverse problems in vision.[3] Here we have concentrated on the important low-level vision application of image deblurring and motion deblurring. In all cases, the blurring was simulated by convolving the original uncorrupted image by a known blurring kernel. We evaluated our algorithm on real images. For comparison purposes we also implemented a regularized inverse solution, obtained by an iterative PCG algorithm. This solution corresponds to using the first derivative as the smoothness term G in equation (5.2), and is a good representative of traditional non discontinuity-preserving methods. It is always possible to choose a smoothing parameter in PCG that gives the same edge crispness as our method, but this leads to noise amplification (an example is shown in figure 5.1. Also note that PCG is subject to various numerical issues such as round-off error, which our method avoids (since we do not perform any floating point calculations). Parameters for our method and for PCG were experimentally chosen from a small number of trial runs.

In the following experiments we used the truncated linear model for potential functions between neighbours:

$$V(l, l') = \frac{\mu}{K} \min(|l - l'|, K).$$

[3]Our method actually covers a larger group of system matrices; we only require that R_H is non-negative.

The factor μ basically provides the weighting between data and prior terms, and was chosen to be $0.4y_{max}$, where y_{max} is the highest intensity in the corrupted image. The cutoff for truncation was chosen to be $K = \frac{y_{max}}{10}$. Thus, all intensity discontinuities greater than a tenth of the largest intensity value were penalized identically by our potential function. The neighbourhood system $\mathcal{N}$ was chosen to be the 8-connected neighbourhood of a pixel.

5.6.1 Deblurring Results

In all experiments shown below, we introduced in the blurred image independent Gaussian additive noise with standard deviation $\sigma_n = 0.02y_{max}$. We used the two blurring kernels:

$$h^1_{blur} = \begin{bmatrix} 1 & 1 & 1 \\ 1 & 1 & 1 \\ 1 & 1 & 1 \end{bmatrix} \qquad h^2_{blur} = \begin{bmatrix} 0 & 1 & 0 \\ 1 & 3 & 1 \\ 0 & 1 & 0 \end{bmatrix}$$

Figure 5.1(a)–(d) show results on a portion of the popular "Lighthouse" image corrupted by h^1_{blur}, which is more severe than the previous example. It is easier to see the effect of the different methods by zooming in on one of the boards in the fence, as shown in (e)–(h). In this example, the blurring in (f) has removed most of the evidence of the edge at the top of the board. PCG and our method perform similarly on the bottom edge of the board; however, on the interior of the board our method does a better job of smoothing, where PCG appears to suffer from noise amplification.

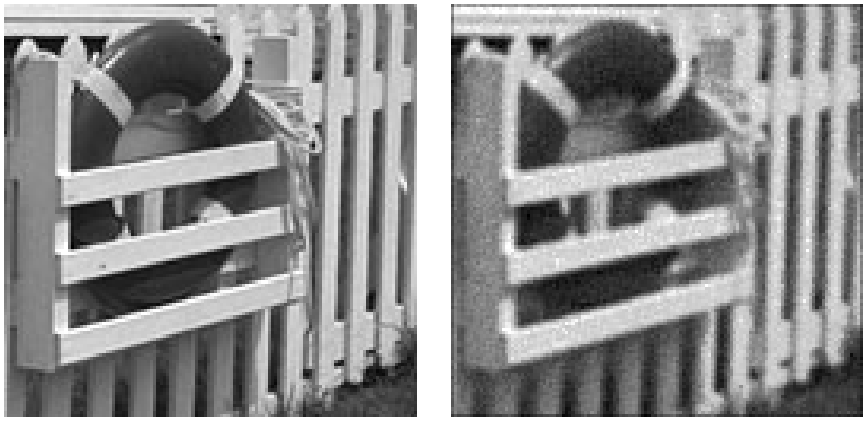

(a) Original image (b) Convolved image

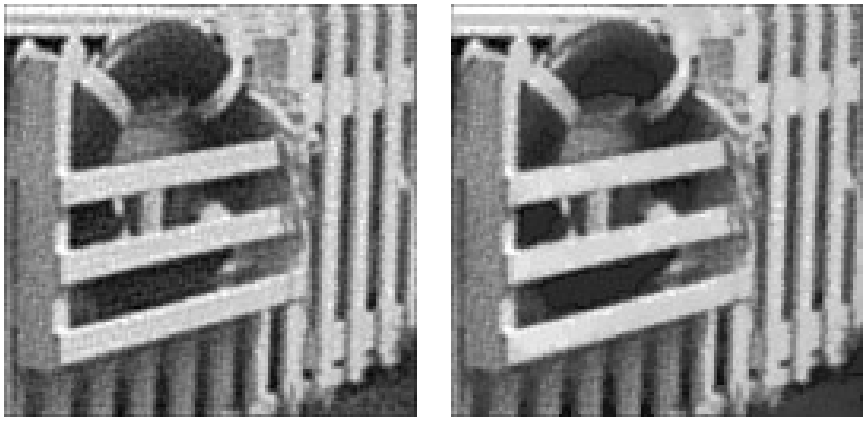

(c) PCG result (d) Our result

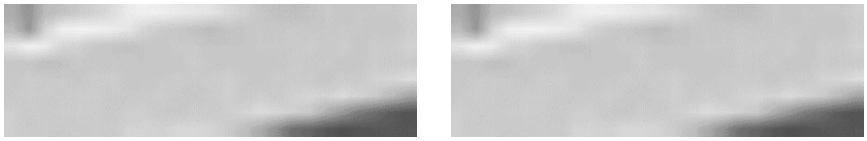

(e) Original image (zoomed) (f) Convolved image (zoomed)

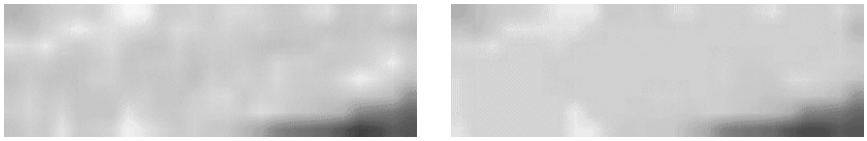

(g) PCG result (zoomed) (h) Our result (zoomed)

Figure 5.1: Deconvolution results on "Lighthouse" image. The original image (a) is convolved with h^1_{blur} to obtain (b). Deconvolving this gives (c) and (d). Zooming in on one of the boards in (a)–(d) produces the results shown in (e)–(h)

5.6.2 Motion Deblurring

The next experiment was to perform motion deblurring using our technique. For this purpose we simulated camera motion by convolving the original "Biker" image with the following kernel:

$$h_{blur}^{motion} = \begin{bmatrix} 1 & 1 & 1 & 1 & 1 & 1 & 1 \end{bmatrix}$$

This simulates camera motion in the horizontal direction for a camera that traverses 7 pixel locations within a single exposure. Figures 5.2(a) - (d) show results on the "Biker" image corrupted by motion blur h_{blur}^{motion}.

Both the PCG solution and our graph cut solution perform well in removing the motion blur. However, our solution displays both lower noise levels as well as better edge preservation. In order to demonstrate the latter property, we show in figures 5.2(e)–(h) a zoomed portion of the image in figure 5.2. The edge-preserving property of our solution is more evident now. The sleeve of the biker shows substantially enhanced sharpness than the PCG solution. Both deblurring methods provide significant improvement in edge definition compared to the blurred image.

A quantitative evaluation was undertaken by computing the PSNR (peak signal to noise ratio) of results on several examples. This is presented in table 5.1. While PSNR is well known not be an ideal measure of visual quality, it is the standard evaluation metric, and the performance of our method using this metric is encouraging.

5.7 Graph Cuts in MR Reconstruction

Having developed the graph cut method for linear inverses arising in vision and image processing, we now turn to MR reconstruction, particularly parallel imaging.

(a) Original image

(b) Motion blurred image

(c) PCG result

(d) Our result

(e) Original (zoomed)

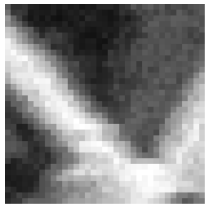

(f) Motion blurred (zoomed)

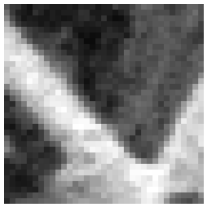

(g) PCG result (zoomed)

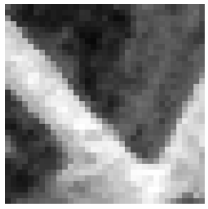

(h) Our result (zoomed)

Figure 5.2: Motion deblurring results on "Biker" image. Original image (a) is blurred with h_{blur}^{motion} to obtain (b). Deblurring results are shown in (c), (d). Zooming in on biker's sleeve produces results in (e)–(h)

Table 5.1: PSNR evaluation. Larger numbers indicate better performance (note that the measurements are in dB, so the scale is logarithmic.)

Image	Blurred	PCG	Our method
Lighthouse	24.1	25.4	26.9
Biker	22.1	21.8	24.7

It is easy to see that in spatial domain the multi-coil system model for parallel imaging shown in equation (2.5) in chapter 2 is a linear system of the form assumed in equation (5.1) earlier in this chapter. Furthermore, from figure 4.1 we know that the elements of E form a diagonal block structure for Cartesian sampling, with each non-zero element being the multiplicative sensitivity map value corresponding to a certain pixel on a certain receiver coil. For Cartesian sampling, the aliasing occurs only along the phase encode direction, according to equation (4.8). Since these values are intensities, they are non-negative. Furthermore, the desired MR image is likely to exhibit spatial correlation of the type well-captured by MRF-based models. We conclude that the MR reconstruction problem for Cartesian sampling is exactly the right candidate for the graph cut method described above. Let us now formalize the argument.

The problem we address is to efficiently minimize

$$\mathcal{E}(x) = ||y - Ex||_2^2 + G_{MRF}(x). \tag{5.25}$$

where E is diagonal-block as shown in chapter 4, and the data term y is the concatenation of aliased outputs from all receiver coils. From (4.8) it can be easily shown that this has the same form as equation (5.11). Let us first define for each pixel $p = (i, j)$ in the lth coil output $y^l, l = 1 \ldots L$, the set of aliasing pixels in x that

contribute to y_p^l, as follows: For an image x of size $M \times N$ undergoing acceleration by a factor R, the aliasing only occurs in the phase encode (i.e. vertical) direction. We will observe that cross terms in the energy function corresponding to Cartesian MRI involve these aliasing pixels. So let us define the aliasing neighbourhood set as all such aliasing pairs $\mathcal{N}_a = (p_r, p_{r'}); r, r' = 1 \ldots R$, where $p_r = (+(M/R)(r-1), j)$. Then we have

$$||y - Ex||_2^2 = \sum_p \sum_l (y_p^l - \sum_r s_{p_r}^l x_{p_r})^2. \tag{5.26}$$

After some rearrangement, this expands to

$$\begin{aligned} ||y - Ex||_2^2 = \sum_{p,l} {y_p^l}^2 - 2 \sum_{p,r} (\sum_l s_{p_r}^l y_p^l) x_{p_r} \\ + \sum_{p,r} (\sum_l {s_{p_r}^l}^2) {x_{p_r}}^2 + 2 \sum_{p,r,r';(p_r,p_{r'}) \in \mathcal{N}_a} (\sum_l s_{p_r}^l s_{p'_r}^l) x_{p_r} x_{p_{r'}}. \end{aligned} \tag{5.27}$$

This complicated-looking equation can be written as

$$a^2 - 2 \sum_{p,r} b(p_r) x_{p_r} + \sum_{p,r} c(p_r) {x_{p_r}}^2 + 2 \sum_{p,r,r';(p_r,p_{r'}) \in \mathcal{N}_a} d(p_r, p_{r'}) x_{p_r} x_{p_r}. \tag{5.28}$$

The first term is a constant and can be removed frm the energy; the next two terms depend only on a single pixel while the last term depends on two pixels at once, both from the aliasing set. Reverting to the notation used earlier, let $p_r \to p, p_{r'} \to q$, and the MR version of the second term in (5.7) becomes

$$2 \sum_{(p,q) \in \mathcal{N}_a} d(p,q) \chi_p \chi_q + \sum_{(p,q) \in \mathcal{N}} V(\chi_p, \chi_q). \tag{5.29}$$

This is exactly the same as the cross term in §5.4, except that the neighbourhood system of cross terms are different. It is straightforward to show that the resulting binary energy is non-regular as before, and cannot be solved using a direct application of α-expansion moves. Instead, the entire mathematical machinery

developed in preceding sections is applicable, and the same graph cut algorithm presented in §5.5 can now solve the MR reconstruction problem.

There are some differences in implementation which we would like to point out at this stage. First, the neighbourhood system pertaining to the cross data terms in 5.29 is quite different from the vision case. In the latter, the local neighbours, for instance the eight 1-connected neighbours of every pixel appear in the neighbourhood system of cross data terms, since the blurring operator is assumed to be over a local window. The situation is quite different in the MR case. From 5.28 it appears that the cross terms in data cost involve "aliasing neighbours" rather than physical neighbours. Moreover, we know that aliasing is usually only in one dimension of the image (i.e. the phase encode direction); thus the "aliasing neighbours" are also aligned in the phase encode direction. The number of such neighbours is equal to the undersampling factor R, which is much smaller than the number of physical neighbours. A major consequence of this is that we can guarantee downhill moves (see Theorem 5.4 by imposing considerably less stringent restrictions on possible expansion moves.

5.8 Experimental results on parallel MR

We evaluated our method on several MR reconstruction data sets, including high-resolution phantom studies as well as clinical studies. The data presented in this section were obtained by simulating the parallel imaging process via the Biot-Savart Law. In figure 5.3 we show results on parallel MR data simulated from an original, fully-sampled high-resolution phantom data. This example assumes 4 coils ($L = 4$), and undersampling by 3 ($R = 3$). This particular example displays a great deal of edge sharpness and high contrast, and we use it to demonstrate the edge-

preserving nature of our method, compared to standard SENSE reconstruction. Zoomed-in versions of a portion of the same images are shown in figure 5.4.

In figure 5.5 we show results on parallel MR data simulated from an original, fully-sampled MRA data set of the leg region. Again we use $L = 4$, $R = 3$. The figure also shows a sub-region which was zoomed-in for clarity. Another zoomed-in sub-region is shown in figure 5.6.

From all these examples it is obvious that our technique performs better than either standard SENSE or its regularized counterpart in terms of visual quality and noise properties. Further work is in progress to quantify these improvements and analyse the conditions under which improvements occur, or do not occur.

5.9 Extensions

The obvious extension of our work would be to generalize our results to arbitrary H. We would only need to handle the case where R_H can be negative; it seems plausible that this could be done by further refining our approximation to the original energy function. Linear inversion problems where R_H can be negative, however, do not appear to arise often in computer vision, and hence our current results cover the vast majority of applications.

It would also be interesting to compare our method with techniques that perform edge-preserving smoothing, such as bilateral filtering [TM98] or anisotropic diffusion [PM90]. Local operators such as bilateral filtering do not have an obvious interpretation in terms of energy minimization, so it is unlikely that there is any theoretical relationship between these methods and our approach. Anisotropic diffusion, on the other hand, can be viewed as a steepest descent method for an MRF-based energy function. As a result, it may be possible to compare anisotropic

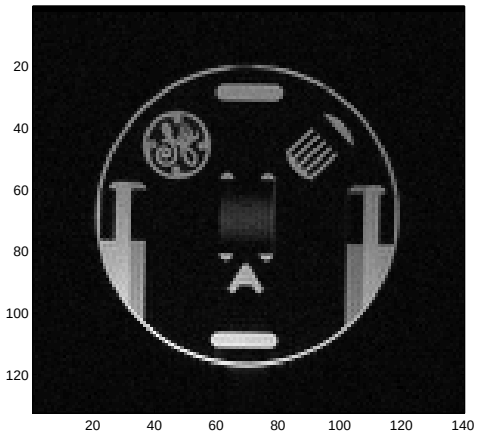

(a) Non-aliased reconstruction

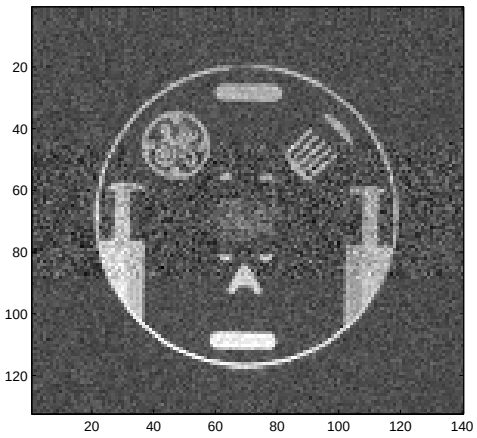

(b) SENSE reconstruction

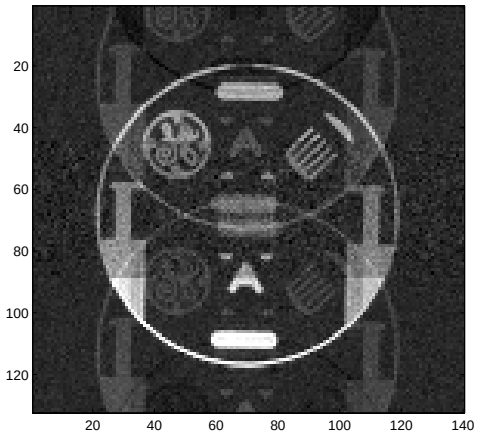

(c) Regularized SENSE

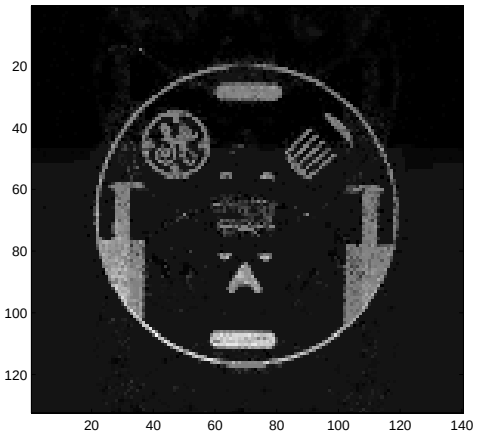

(d) GCMR reconstruction

Figure 5.3: Parallel reconstruction results on HiRes data: 4 coils and acceleration factor of 3. The original un-aliased reconstruction is shown in (a), SENSE reconstruction in (b), regularized SENSE in (c) and our GCMR method in (d).

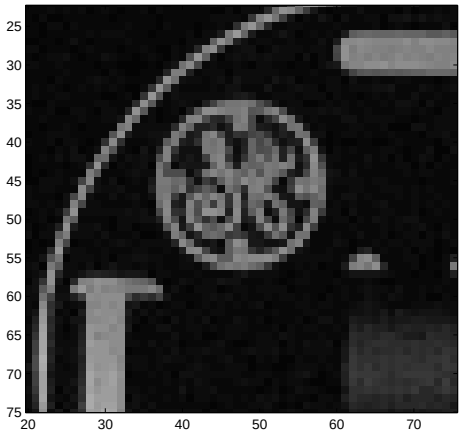

(a) Non-aliased reconstruction

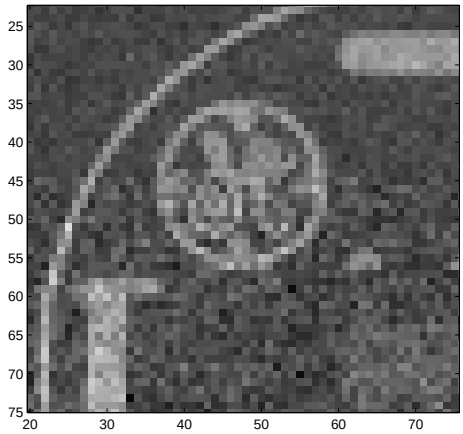

(b) SENSE reconstruction

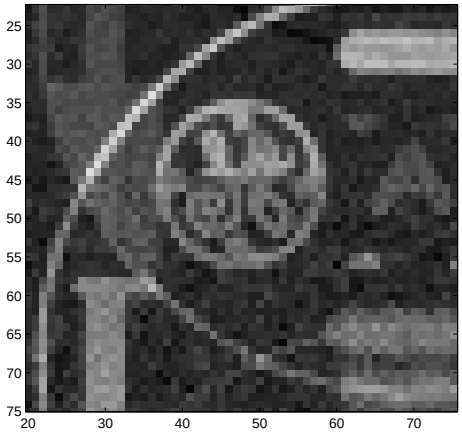

(c) Regularized SENSE

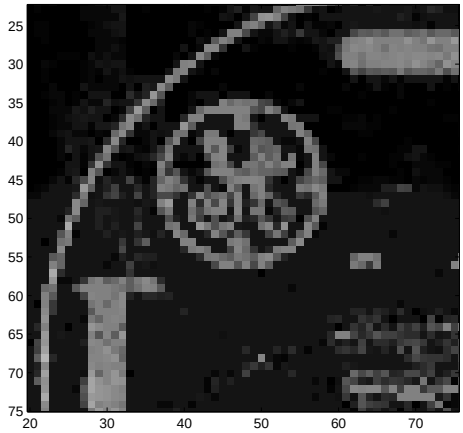

(d) GCMR reconstruction

Figure 5.4: Zoomed up portion of images in figure 5.3: (a) original un-aliased image, (b) SENSE reconstruction, (c) regularized SENSE, and (d) GCMR method.

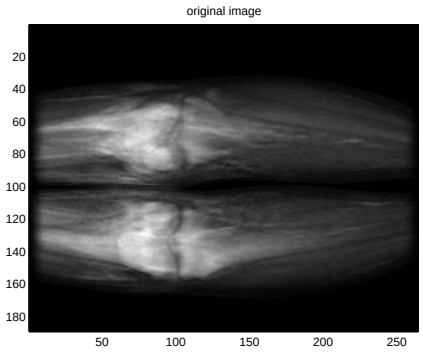

(a) Non-aliased reconstruction

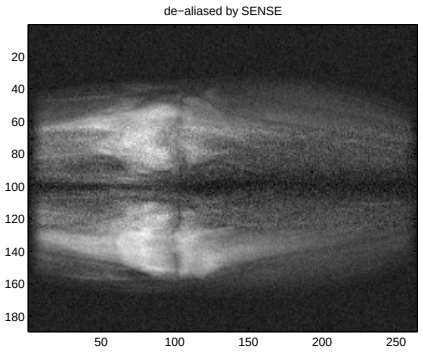

(b) SENSE reconstruction

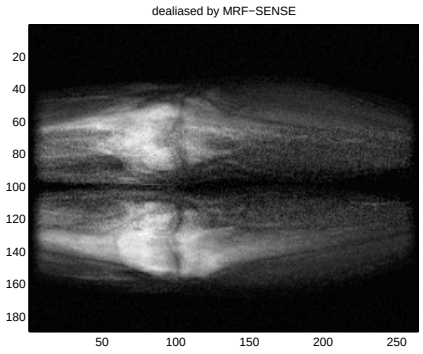

(c) GCMR reconstruction

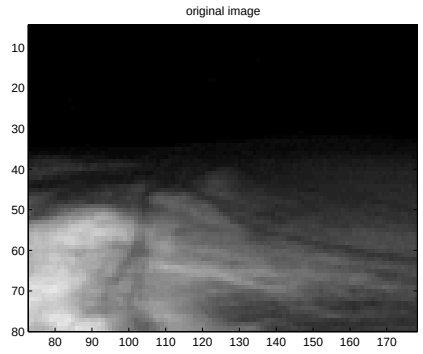

(d) Original image (zoomed)

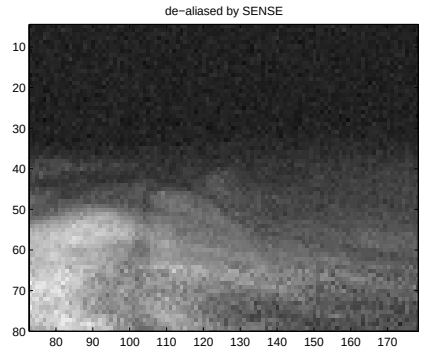

(e) SENSE reconstruction (zoomed)

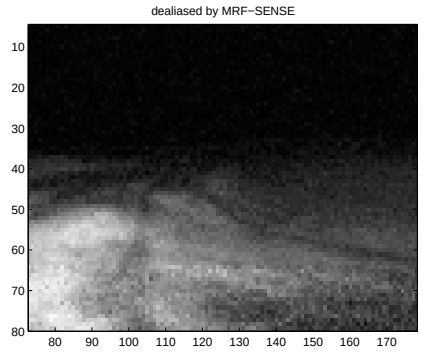

(f) GCMR reconstruction (zoomed)

Figure 5.5: MR parallel reconstruction results on leg data: 4 coils, 3x acceleration. The original un-aliased data shown in (a), SENSE reconstruction in (b), and GCMR method in (c). Zooming in on one portion of the image produces (d)–(f).

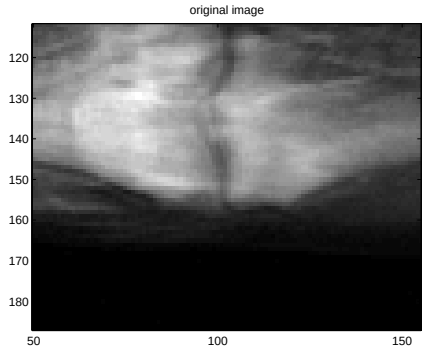

(a) Original image (zoomed)

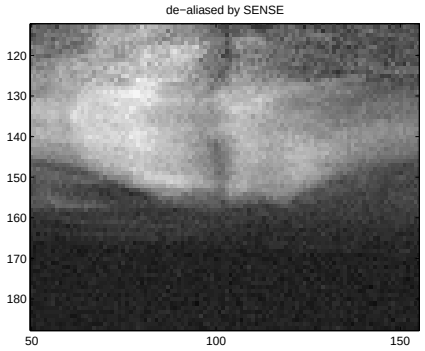

(b) SENSE reconstruction (zoomed)

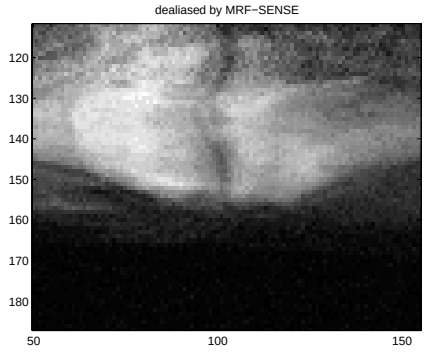

(c) GCMR reconstruction (zoomed)

Figure 5.6: Another zoomed portion of data presented in figure 5.5 (a), SENSE reconstruction, (b)SENSE and (c) GCMR.

diffusion with our method on identical energy functions, much as [TF03] compared LBP with graph cuts.

In the field of parallel MR reconstruction, a major extension would be to cover other sampling trajectories like spiral or radial. These trajectories will in general result in the entries of system matrix E being complex - a case that our current method is unable to handle. A generalization to arbitrary matrices will remove this restriction.

Chapter 6

Conclusions

This thesis described a number of algorithms related to the acquisition, reconstruction and post-processing of Magnetic Resonance data. These algorithms form parts of an elegant, unified linear systems framework within which fall many exciting and challenging problems in MR. The unified systems approach was inspired by developments in other computational fields like vision, signal and image processing. There have been few and sporadic attempts at exploiting the developments in these other fields for use in MRI, and this thesis should be considered a long-overdue step in that direction. We have used various ideas from estimation and detection theory, Graph Theory and multi-variate optimization and put them within the overall linear systems framework for MR. The algorithms we presented have the potential to result in disruptive innovations in several areas of MR. We argued that these techniques address in different but complementary ways the common goal of improving the fundamental time-quality trade-off in MR imaging. Let us list some novel ideas contained in the thesis.

We developed a new retrospective motion correction technique based on successive convex projections. The method corrects a motion corrupted frame in MRA sequence by iteratively making it more similar to a non-corrupted one. The algorithm is able to correct corrupted features both in k-space and image space without degrading radiologically important temporal events. The technique has the potential to retrieve corrupted angiography data that would otherwise be unusable due to motion artifacts. Results indicate significant improvement in MRA

quality, both from visual evidence as well as from a double-blind comparison.

A maximum-likelihood algorithm was developed to obtain an optimal solution to the parallel imaging reconstruction problem in the presence of both measurement and sensitivity noise. We argued that existing methods prove quite inadequate in tackling this problem, which is in fact a more natural model of the parallel imaging process than those used currently. We showed that for i.i.d. Gaussian noise the optimal solution is the minimizer of a weakly non-quadratic objective function which we solved efficiently via a non-linear least squares iterative technique with modest additional complexity compared to standard SENSE algorithms. A fast Newton algorithm with explicit Jacobian information was developed to solve the problem. Results for Cartesian k-space sampling indicate impressive improvement in performance compared to standard SENSE, amounting to almost 20 dB SNR gain in several high-noise cases. The algorithm yields substantial improvement even in cases where the i.i.d. Gaussian sensitivity noise model implicit in the method is not accurate.

Next we developed a new graph cut method to solve Bayesian estimation problems that arise in medical imaging, signal and image processing and machine vision. This approach benefits immensely from a Markov Random Field (MRF) based formulation of *a priori* information. The main restriction of our technique is that it works only on linear systems with non-negative matrix elements. We developed the general case, then specialised it to image deconvolution, motion deblurring and MR reconstruction from parallel data. The basic idea behind MRF-based Bayesian estimation is to impose a discontinuity-preserving smoothness term, which we accomplished by assuming the prior to have a Gibbsian distribution defined on an MRF. We developed a fast energy minimization method based on graph cuts to

solve this rather challenging numerical problem. We demonstrated our method by applying it for image deconvolution and motion deblurring on real images, as well as parallel MR reconstruction from raw Fourier data.

Taken separately or in combination with each other, the techniques presented in this thesis form a promising foundation upon which to build a unified linear systems approach to solving medical imaging problems.

6.1 Extensions

6.1.1 TL-SENSE for arbitrary sampling

The TL-SENSE algorithm developed in chapter 4 concentrated on the Cartesian sampling case, which happens to be the most widely used method currently. However, in the future, other trajectories like spira lor radial are likely to become very popular, since they intrinsically sample th emiddle of k-space, where most of the data lies, more densely than outer k-space. Using these nearly-sphericaly-symmetric trajectries is also very useful during motion correction. Hence a powerful extension of the TL-SENSE method would be to allowthe use of these trajectories. The reconstruction can no longer be reduced to independent sub-problems over columns like the Cartesian case, so the new algorithm is likely to be much more computationally challenging. But a modified Conjugate Gradients approach could perform reasonably well without incurring prohibitive compuation time.

6.1.2 TL-SENSE for general noise models

Recall that our algorithm assumes i.i.d. Gaussian noise in sensitivity maps. While we presented some data to support our contention that the method does well even

when this assumption is violated, there is a case for an algorithm that can handle arbitrary noise models. For instance, consider the situation where the sensitivity errors are mainly due to mis-orientation of coils between actual scan and pre-scan. Or the case where flexible receiver pads were used. Sensitivity noise in these cases can not be easily modelled under the i.i.d. assumption, but it can be safely assumed that such noise is of a low-frequency nature. We are currently exploring ways to extend the TL-SENSE algorithm to these noise models. Preliminary results suggest improvement upon the i.i.d. noise assumption, but much more work needs to be done before we obtain a final algorithm.

6.1.3 Graph Cut methods for arbitrary linear systems

An obvious extension of our MRF based Bayesian work would be to generalize our results to arbitrary linear systems, and not merely those with non-negative entries. Among other things, this will prove useful for arbitrary sampling trajectories in MR, as well as some deblurring problems (not frequently occurring however) in images. A general algorithm will make the method useful for other linear systems outside of vision or medical imaging.

BIBLIOGRAPHY

[AMH91] Theagenis J. Abatzoglou, Jerry M. Mendel, and Gail A. Harada. The Constrained Total Least Squares technique and its applications to harmonic superresolution. *IEEE Transactions on Signal Processing*, 39(5):1070–1087, May 1991.

[BB98] M Beretro and P Boccacci. *Introduction to Inverse Problems in Imaging*. Institute of Physics Publishing, 1998.

[BS93] Charles Bouman and Ken Sauer. A generalized Gaussian image model for edge preserving MAP estimation. *IEEE Transactions on Image Processing*, 2(3):296–310, July 1993.

[BVZ01] Yuri Boykov, Olga Veksler, and Ramin Zabih. Fast approximate energy minimization via graph cuts. *IEEE Transactions on Pattern Analysis and Machine Intelligence*, 23(11):1222–1239, November 2001.

[DEMM03] McRobbie DW, Moore EA, Graves MJ, and Prince MR. *MRI: From Picture to Proton*. Cambridge, UK, 2003.

[ea96] R. Zoroofi et al. Cancellation of MRI artifacts in image plane. *IEEE Transactions on Medical Imaging*, 5(6):178–182, June 1996.

[EK02] N. Park et al E. Kim. Cancellation of MRI motion artifact in image plane. *IEEE I&M Technical Conference Proceedings*, pages 329–334, May 2002.

[Fer94] P. J. Ferreira. Interpolation and the discrete Gerchberg-Papoulis algorithm. *IEEE Transactions on Signal Processing*, 42(10):22–29, October 1994.

[FL97] Mario A. Figueiredo and Jose M. Leitao. Unsupervised image restoration and edge location using compound Gauss-Markov random fields and the MDL principle. *IEEE Transactions on Image Processing*, 6(8):1089–1102, August 1997.

[GBD04] P. Gravel, G. Beaudoin, and J.A. DeGuise. A method for modeling noise in medical images. *IEEE Transactions on Medical Imaging*, 23(10):1221–1232, October 2004.

[GL96] G. Golub and C. Van Loan. *Matrix Computations*. Johns Hopkins University Press, 1996.

[GPR67] L G Gubin, B T Polyak, and E V Raik. The method of projections for finding the common point of convex sets. *USSR Computational Mathematics and Mathematical Physics*, 7:1–24, 1967.

[GWB86] E. Gmelin, H. D. Weiss, and F. Buchmann. Cardiac gating in intravenous dsa. *European J. Radiology*, 6(1):24–29, 1986.

[HL02] Sabine Van Huffel and Philippe Lemmerling. *Total Least Squares and Errors-in-Variables Modeling: Analysis, Algorithms and Applications*. Kluwer, 2002.

[Hog03] W. S. Hoge. A subspace identification extension to the phase correlation method. *IEEE Transactions on Medical Imaging*, 22(2):223–227, February 2003.

[Ish03] Hiroshi Ishikawa. Exact optimization for Markov Random Fields with convex priors. *IEEE Transactions on Pattern Analysis and Machine Intelligence*, 25(10):1333–1336, October 2003.

[Kay93] S. Kay. *Fundamentals of Statistical Signal Processing: Volume I - Estimation Theory*. Prentice-Hall, Upper Saddle River, NJ, 1993.

[Kim03] Junwan Kim. *Computer Vision Algorithms in Magnetic Resonance Imaging*. PhD thesis, Cornell University, August 2003.

[KPZ+02] Junhwan Kim, Martin R. Prince, Ramin Zabih, Jeff Bezanson, Richard Watts, Hale E. Erel, and Yi Wang. Automatic selection of mask and arterial phase images for temporally-resolved mr digital subtraction angiography. *Magnetic Resonance in Medicine*, 48(6):1004–1010, 2002.

[KZ03] Junhwan Kim and Ramin Zabih. Automatic segmentation of contrast-enhanced image sequences. In *International Conference on Computer Vision*, pages 502–509, 2003.

[KZ04] Vladimir Kolmogorov and Ramin Zabih. What energy functions can be minimized via graph cuts? *IEEE Transactions on Pattern Analysis and Machine Intelligence*, 26(2):147–159, February 2004.

[LBJ+02] Z. P. Liang, R. Bammer, J. Ji, N. Pelc, and G. Glover. Improved image reconstruction from sensitivity-encoded data by wavelet denoising and Tikhonov regularization. In *Proc. International Summer School on Biomedical Imaging*, pages 493–496, 2002.

[LdMH96] Philippe Lemmerling, Bart de Moor, and Sabine Van Huffel. On the equivalence of Constrained Total Least Squares and Structured Total Least Squares. *IEEE Transactions on Signal Processing*, 44:2908–2911, November 1996.

[Li95] S. Li. *Markov Random Field Modeling in Computer Vision*. Springer-Verlag, 1995.

[LL99] Zhi-Pei Liang and Paul C Lauterbur. *Principles of Magnetic Resonance Imaging: A Signal Processing Perspective*. IEEE Press, 1999.

[MGK95] Vladimir Z. Mesarovic, Nikolas P. Galatsanos, and Aggelos K. Katsaggelos. Regularized Constrained Total Least Squares image restoration. *IEEE Transactions on Image Processing*, 4(8):1096–1108, August 1995.

[MNV99] Erik H. Meijering, Wiro J. Niessen, and Max A. Viergever. Retrospective motion correction in digital subtraction angiography: A review. *IEEE Transactions on Medical Imaging*, 18(1):2–21, January 1999.

[MOY+01] C. A. McKenzie, M. A. Ohliger, E. N. Yeh, M. D. Price, and D. K. Sodickson. Coil-by-coil image reconstruction with SMASH. *Magnetic Resonance in Medicine*, 46:619–623, 2001.

[MP03] K. L. Miller and J. M. Pauly. Nonlinear phase correction for navigated diffusion imaging. *Magnetic Resonance in Medicine*, 50:343–353, 2003.

[MTJ98] Prince MR, Grist TM, and Debatin JF. *3D Contrast MR Angiography*. Springer-Verlag, New York, 1998.

[OFS88] P Oskoui-Fard and H Stark. Tomographic image reconstruction using convex projections. *IEEE Transactions on Medical Imaging*, 7:45–58, March 1988.

[Opi67] Z. Opial. Weak convergence of the sequence of successive approximations for nonexpansive mappings. *Bulletin of the American Mathematical Society*, 73:591–597, 1967.

[Pea88] Judeah Pearl. *Probabilistic reasoning in intelligent systems: networks of plausible inference*. Morgan Kaufmann, 1988.

[PM90] P. Perona and J. Malik. Scale space and edge detection using anisotropic diffusion. *IEEE Transactions on Pattern Analysis and Machine Intelligence*, 12(7):629–639, July 1990.

[PT97] Yani Picard and Christopher J. Thompson. Motion correction of pet images using multiple acquisition frames. *IEEE Transactions on Medical Imaging*, 16(2):137–144, April 1997.

[PTK85] Tomaso Poggio, Vincent Torre, and Christof Koch. Computational vision and regularization theory. *Nature*, 317:314–319, 1985.

[PTVF92] William Press, Saul Teukolsky, William Vetterling, and Brian Flannery. *Numerical Recipes in C*. Cambridge, 2nd edition, 1992.

[PWBB01] K. P. Pruessmann, M. Weiger, Peter Boernert, and Peter Boesiger. Advances in sensitivity encoding with arbitrary k-space trajectories. *Magnetic Resonance in Medicine*, 46:638–651, 2001.

[PWSB01] K. P. Pruessmann, M. Weiger, M. B. Scheidegger, and Peter Boesiger. SENSE: sensitivity encoding for fast MRI. *Magnetic Resonance in Medicine*, 42(5):952–962, 2001.

[RA98] K. Ratakonda and N. Ahuja. POCS-based adaptive image magnification. *Proceedings, International Conference on Image Processing*, pages 1231–35, October 1998.

[SM97] P. Stoica and R. L. Moses. *Introduction to Spectral Analysis*. Prentice-Hall, 1997.

[SS02] Daniel Scharstein and Richard Szeliski. A taxonomy and evaluation of dense two-frame stereo correspondence algorithms. *International Journal of Computer Vision*, 47:7–42, April 2002.

[TF03] M.F. Tappen and W.T. Freeman. Comparison of graph cuts with belief propagation for stereo, using identical MRF parameters. In *International Conference on Computer Vision*, pages 900–907, 2003.

[TM98] C. Tomasi and R. Manduchi. Bilateral filtering for gray and color images. In *International Conference on Computer Vision*, pages 839–846, 1998.

[TRF04] M.F. Tappen, B.C. Russell, and W.T. Freeman. Efficient graphical models for processing images. In *IEEE Conference on Computer Vision and Pattern Recognition*, pages II: 673–680, 2004.

[vdBWK+03] Johan S. van den Brinka, Yuji Watanabeb, Christiane K. Kuhlc, Taylor Chungd, Raja Muthupillaia, Marc Van Cauterena, Kei Yamadae, Steven Dymarkowskif, Jan Bogaertf, Jeff H. Makig, Celso Matosh, Jan W. Casselmani, and Romhild M. Hoogeveena. Implications of SENSE MR in routine clinical practice. *European Journal of Radiology*, 46(1):3–27, April 2003.

[WBP04] Florian Wiesinger, Peter Boesiger, and Klaas Pruessmann. Electrodynamics and ultimate SNR in parallel MR imaging. *Magnetic Resonance in Medicine*, 52(2):376–390, August 2004.

[Wel67] P. D. Welch. The use of fast fourier tranforms for the estimation of power spectra: A method based on time averaging over short modified periodograms. 15:70–73, 1967.

[WND+03] B. J. Wintersperger, K. Nikolaou, O. Dietrich, J. Rieber, M. Nittka, M. F. Reiser, and S. O. Schoenberg. Single breath-hold real-time cine MR imaging: improved temporal resolution using generalized autocalibrating partially parallel acquisition (GRAPPA) algorithm. *European Journal of Radiology*, 13(8):1931–1936, May 2003.

[XH01] Yingbiao Xu and E M Haacke. Partial fourier imaging in multi-dimensions: A means to save a full factor of two in time. 14:628–635, 2001.